CHANNEL MODELING AND CHARACTERIZATION FOR INDOOR AND VEHICULAR MILLIMETER WAVE (MMW) COMMUNICATIONS

A Dissertation

by

Fahimeh Aghaei

Submitted to the
Graduate School of Sciences and Engineering
In Partial Fulfillment of the Requirements for
the Degree of

Doctor of Philosophy

in the
Department of Electrical and Electronics Engineering

Özyeğin University
January 2024

CHANNEL MODELING AND CHARACTERIZATION FOR INDOOR AND VEHICULAR MILLIMETER WAVE (MMW) COMMUNICATIONS

Approved by:

Professor Murat Uysal, Advisor
Department of Electrical and Electronics Engineering
Özyeğin University

Assistant Professor Çağatay Edemen
Department of Electrical and Electronics Engineering
Özyeğin University

Assistant Professor Kadir Durak
Department of Electrical and Electronics Engineering
Özyeğin University

Associate Professor Eylem Erdogan
Department of Electrical and Electronics Engineering
Istanbul Medeniyet University

Date Approved: 28 December 2024

Assistant Professor Tahsin Yilmaz
Department of Electrical and Electronics Engineering
Yeni Yuzyil University

To

My parents for their love, endless support, patience, and encouragement.

My siblings for their unwavering support.

ABSTRACT

The demand for ultra-high-speed wireless connectivity is ever-increasing, which poses unique challenges for the next-generation wireless communication system design. This has prompted the exploration of higher frequency bands including millimeter wave millimeter Wave (MMW) and visible light bands in addition to the conventional sub-6 GHz band. In this thesis, we provide a detailed comparison of these frequency bands' propagation channels in identical indoor settings. We adopt ray tracing techniques for site-specific channel modeling, which enables the consideration of the three-dimensional models of the indoor environment and objects inside. Using ray tracing, we model site-specific channels in three-dimensional indoor environments, considering various frequencies (2.4 GHz to 100 GHz) and transmitter types (Radio Frequency (RF) antennas and indoor lighting for Visible Light Communication (VLC)). Our analysis includes Channel Impulse Response Channel Impulse Response (CIR) data, channel path losses, and Cumulative Distribution Function Cumulative Distribution Function (CDF) expressions for received power levels across all considered frequencies. Our results highlight that VLC channels demonstrate lower path loss than MMW but more than the 2.4 GHz band, while also revealing the impact of antenna types on MMW path loss, especially over shorter transmission distances.

Vehicle to Vehicle (V2V) communication is an underlying key technology to realize future intelligent transportation systems. Both MMW communication and VLC are strong candidates to address V2V connectivity. Most of the earlier literature focuses on individual technology. In an effort to better highlight the differences and relative advantages of these two competing technologies, we provide a comprehensive one-to-one comparison between vehicular VLC and MMW channels in this thesis. For this purpose, we utilize ray tracing

simulations which enable the consideration of three-dimensional modeling of the propagation environment and allow the study of various system parameters and road conditions in both Line of Sight (LOS) and Non Line of Sight (NLOS) conditions. In the same settings, we showcase the signal strengths for both systems and study their channel features for communication between vehicles in the same or different lanes, assessing the effects of varying densities of neighboring vehicles and instances of partial or complete blockage.

ÖZETÇE

Üstün hızda kablosuz bağlantı talebi sürekli artıyor, bu da gelecek nesil kablosuz iletiş-im sistem tasarımı için benzersiz zorluklar doğuruyor. Bunun üzerine, geleneksel alt-6 GHz bandına ek olarak milimetre dalga (MMW) ve görünür ışık bantları gibi yüksek frekanslı bantların keşfine yönelik çalışmalar hız kazandı. Bu araştırma, aynı iç mekan ayarlarında bu frekans bantlarının yayılma kanallarını detaylı bir şekilde karşılaştırıyor. Siteye özgü kanal modelleme için ışın izleme tekniklerini kullanıyoruz, bu da iç mekanın üç boyutlu modellerini ve içindeki nesneleri dikkate alma imkanı sağlıyor. 2.4 GHz ile 100 GHz arasındaki çeşitli frekanslar ve Verici Frekansı (RF) antenleri ile Görünür Işık İletişimi (VLC) için iç mekan aydınlatma gibi farklı verici tiplerini göz önünde bulundurarak, ışın izleme ile siteye özgü kanalları modelliyoruz. Analizimiz, Telsiz İmpuls Cevabı (CIR) verilerini, kanal yol kayıplarını ve alınan güç seviyelerinin Kumulatif Dağılım Fonksiyonu (CDF) ifadelerini içeriyor. Sonuçlarımız, VLC kanallarının MMW'den daha düşük yol kaybına sahip olduğunu ancak 2.4 GHz bandından daha fazla olduğunu gösterirken, aynı zamanda özellikle kısa iletim mesafelerindeki MMW yol kaybına anten tiplerinin etkisini ortaya koyuyor.

V2V iletişimi, gelecekteki akıllı ulaşım sistemlerini gerçekleştirmek için temel bir anahtar teknolojidir. Hem MMW iletişimi hem de VLC, V2V bağlantısını ele almaya güçlü adaylardır. Daha önceki literatürün çoğu bireysel teknolojiye odaklanmaktadır. Bu iki rakip teknolojinin farklılıklarını ve göreceli avantajlarını daha iyi vurgulamak amacıyla, bu tezde araç VLC ve MMW kanalları arasında kapsamlı bire bir karşılaştırma sunuyoruz. Bu amaçla, yayılma ortamının üç boyutlu modellemesinin dikkate alınmasına olanak tanıyan ve çeşitli sistem parametrelerinin ve yol koşullarının hem görüş hattı hem de görüş hattı dışı koşullarda incelenmesine olanak tanıyan ışın izleme simülasyonlarından yararlanıyoruz. Aynı ayarlar altında, her iki sistem için alınan sinyal güçlerini sunuyoruz ve aynı şeritte ve farklı şeritlerde bulunan iki araç arasındaki iletişim için yanal kaydırma ile kanal özelliklerini araştırıyoruz. Ayrıca komşu araçların düşük, orta ve yüksek yoğunluğunun yanı sıra kısmi ve tam tıkanmaların etkisini de analiz ediyoruz.

ACKNOWLEDGEMENTS

I am grateful to my supervisor, Prof. Murat Uysal, for his ongoing mentorship and the never-ending supply of fascinating tasks. His humble approach to research and science is an inspiration. This approach is evident in his simple but obvious writing style, which I aspire to emulate throughout my career. He genuinely deserved the prestigious Mustafa Prize (Science and Technology Award of Islamic World) in 2023.

I am truly grateful to the members of my dissertation committee, Asst. Prof. Kadir Durak, and Dr. Tahsin Yilmaz for their time serving on my committee and carefully reviewing my dissertation.

I am also grateful for technical and non-technical discussions with my colleague Dr. Hossien B Eldeeb in the CT&T research group at Özyeğin university. It is worth noting that all results related to VLC are part of our common papers and used in this work by his authorization for comparison purposes.

Last, but not least, I would like to thank my mother and father, for their love and encouragement. Words cannot express the feeling I have for my parents for their constant unconditional support, both emotionally and financially. I also want to express my deepest gratitude to my brother, Ali, for his unstoppable love and support.

ACRONYMS

3D	Three Dimension
AL	Atmospheric Loss
AoV	Angle of Arrival
CIR	Channel Impulse Response
CAD	Computer Aided Design
CDF	Cumulative Distribution Function
DoA	Direction of Arrival
DSRC	Dedicated Short-Range Communication
FoV	Field of View
GO	Geometric Optics
ITS	Intelligent Transportation System
LED	Light Emitting Diode
LOS	Line of Sight
MMW	millimeter Wave
MIMO	Multiple-Input Multiple-Output
MPCs	Multipath Components
MPM	Millimeter wave Propagation Model
NLOS	Non Line of Sight
PDP	Power Delay Profile
RMS	Root Mean Square
RF	Radio Frequency
RX	Receiver
SBR	Shooting and Bouncing Ray

SINR	Signal-to- Interference-Noise Ratio
THz	Terahertz
ToA	Time of Arrival
TX	Transmitter
UTD	Uniform Theory of Diffraction
UE	User Equipment
V2V	Vehicle to Vehicle
VLC	Visible Light Communication
VSWR	Voltage Standing Wave Ratio

TABLE OF CONTENTS

LIST OF TABLES

LIST OF FIGURES

CHAPTER I

INTRODUCTION

1.1 Motivation

MMW communication has raised increasing attention from academia and industry due to its exceptional benefits. The MMW frequencies, approximately ranging from 30GHz to 300GHz, have gained significant interest due to their substantial bandwidth. Compared with other wireless methods like WiFi and 4G, MMW communication utilizes significantly higher carrier frequencies, offering substantial advantages such as extensive bandwidth, focused transmission, superior quality, and robust detection capabilities. For example, these advantages effectively tackle challenges posed by modern wireless applications, particularly in managing the skyrocketing traffic demand for wireless communication, especially with video streaming. However, MMW communications inherently face drawbacks like signal attenuation caused by oxygen absorption, susceptibility to obstruction, and limited coverage due to their shorter wavelengths. Fig. 1 shows that MMW communication experiences relatively small attenuation in some special bands such as 35 GHz, 94 GHz, 140 GHz, and 220 GHz. Therefore, long-distance communication being suitable for peer-to-peer communication can be realized in these MMW bands. However, MMW signals attenuate severely as high as 15 dB/km known as “Attenuation Peak” in 60 GHz, 120 GHz, and 180 GHz. Meanwhile, MMW signals face challenges with poor diffraction when obstructed due to their shorter wavelengths. These limitations significantly restrict the transmission range of MMW signals, often leading to disconnections in MMW links. However, advancements in complementary metal-oxide-semiconductor (CMOS) radio frequency (RF) integrated circuits have accelerated the utilization of beamforming techniques employing large-scale MMW antenna arrays to expand the reach of MMW networks. Additionally, by leveraging

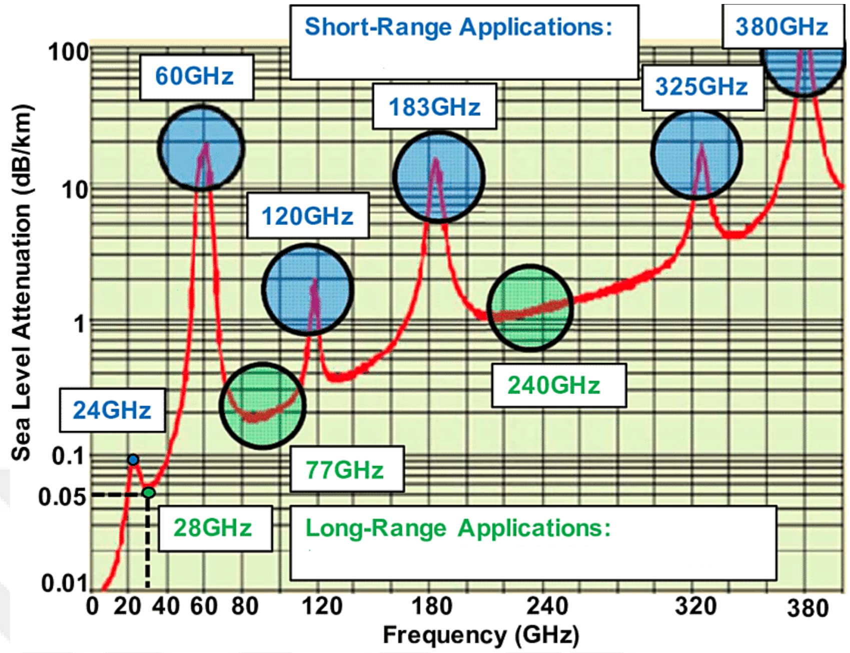

Figure 1: Atmospheric and molecular absorption at MMW frequencies.

highly directional beams, interference within MMW networks can be notably minimized, transitioning these networks into being primarily noise-limited rather than interference-limited in various scenarios. Consequently, the primary challenge lies in mitigating these limitations while maximizing their advantages.

In the following several advantages associated with MMW communications are outlined in contrast to 4G wireless technologies.

- **Extremely wide bandwidths**: Compared to 4G wireless networks, MMW communications utilize significantly higher frequencies (30-300GHz) as carrier frequencies, thereby boasting a much broader spectrum resource (270GHz), which renders it highly attractive in scenarios with dense spectrum availability.

- **Small element sizes**: Due to their short wavelengths, MMW devices facilitate the integration of extensive antenna arrays within small physical dimensions.

- **Narrow beams**: Using the same antenna dimensions, it's feasible to incorporate more antenna elements in MMW frequencies compared to microwaves. Consequently, this ability allows for narrower beam formation, providing opportunities for the advancement of applications like detection radars.

1.2 MMW Channel Modeling

Since the wavelength of the MMW band is considerably shorter than the sub-6 GHz, MMW communication has distinctive fundamental characteristics [1, 2]. Therefore, there is a crucial requirement to have accurate and reliable knowledge of MMW propagation characteristics. The propagation parameters including path loss, delay spread, frequency-dependence material penetration, the effect of propagation mechanism (reflection, diffraction, scattering), the effect of weather conditions, and attenuation losses are taken into account to characterize the radio propagation. These parameters can be obtained through channel measurements, theoretical formulas, or ray tracing tools.

Several works have already investigated RF channel modeling for indoor scenarios [3–8]. For example, the works in [3–6] examined the RF propagation channels at low-frequency bands of 2.4 GHz [3], 10 GHz [4], 11 GHz [5], and 23.5 GHz [6]. Although [3] and [4] assumed the availability of the direct LOS link, [5] and [6] considered the case of obstructed LOS called NLOS and its effect. [9] assumed only the first-order reflection from the walls in an indoor environment. It should be also noted that the previous works considered only limited-low MMW frequencies, which restricts their applicability to higher MMW frequency cases. Considering the higher MMW frequencies is a crucial aspect of meeting the escalating demands for consistently high-quality performance. The impact of the higher MMW frequencies up to 60 GHz on indoor channels was then examined in [7], [9] for a conference room scenario. The wide-band channel measurements were also conducted in [8] to investigate the effect of propagation distance on indoor scenarios. The results showed that both standard deviation and path loss outcomes are frequency-dependent, particularly exhibiting higher values at 60 GHz compared to other frequencies.

In MMW communication systems, the antenna type is a significant factor that can notably influence wireless channels and overall system performance [10]. Research has indicated that employing directional antennas at both the transmitter and receiver in indoor scenarios considerably diminishes Root Mean Square (RMS) delay spread compared to using omnidirectional antennas. Ray tracing stands out as a more adaptable and realistic channel modeling approach for exploring MMW channels. This methodology enables the incorporation of a 3D model of the testing environment, facilitating the examination of both LOS and NLOS paths, similar to the consideration of various antenna types. For instance, in [11], the Wireless Insite ray-tracing simulator was employed to capture CIR at 433 MHz in an empty room. Despite the simplicity of the scenario, this approach indicated the realism achievable through such channel modeling techniques.

To achieve precise environmental sensing and enhance vehicle automation, there's a growing need for exchanging a substantial volume of sensing data among vehicles. As the number of vehicular sensors rapidly expands [12], the challenge intensifies due to the heightened complexity of sensing systems. Handling the enormous data flow, often reaching terabytes, becomes increasingly daunting for vehicles in terms of real-time transmission and processing. Existing V2V communication systems, like Dedicated Short-Range Communication (DSRC) [13], typically struggle to facilitate such extensive transmission and processing demands. To enable the transmission of substantial data volumes known as big data, MMW communication technology presents a solution, offering gigabit-per-second transmission rates. MMW vehicular communication was explored at different frequencies such as 28 GHz, 30 GHz, 38 GHz, 60 GHz, and 73 GHz [14–19]. In [14], the proposed 3GPP channel model for V2X systems was investigated and the impact of several automotive-specific parameters on the overall performance was demonstrated in urban and highway conditions at 60 GHz. A two-path power delay profile model was proposed for V2V LOS channels at 38 GHz and 60 GHz based on the measurements [15]. In [17], the Angle of Arrival (AoV) measurements were measured in a parking lot using in-vehicle antennas at 60 GHz. In [18], the V2V blockage characteristics were explored at 28 GHz to determine the blockage loss caused by the vehicles depending on the receiver's positions. The work in [19] studied the inter-vehicle blockage by conducting measurements at 6.75, 30, 60, and 73 GHz with an ultra-wideband multi-channel sounder. Despite the advantages of 5G MMW access, transmissions at such high frequencies (6 GHz) commonly encounter significant propagation loss and obstructions (caused by large vehicles and so on). To mitigate this challenge, MMW transmitters concentrate transmission power in a specific direction, effectively extending the practical transmission range. However, this directional transmission in MMW, referred to as an MMW beam, introduces fresh hurdles in communications, with one of the foremost concerns being mobility management especially critical in vehicular communication scenarios involving moving User Equipment (UE), such as vehicles. Ensuring connectivity requires precise beam alignment and robustness in maintaining connections against rapid channel changes [20], [21]. Additionally, novel solutions are necessary to switch between beams, particularly in cases involving highly mobile vehicles [22]. During connectivity, the UE encounters two forms of mobility in MMW, known as cell level and beam level mobility, as outlined in 3GPP.

A comparison of MMW channel modeling discussed so far is classified in Table 1 regarding the environment, operating frequency, and other scenario assumptions.

Table 1: Comparison of Indoor-Outdoor MMW channel modeling

Ref.	**Environment**	**Frequency**	**Other Assumptions**
[3]-[4]	Indoor	2.4GHz-10GHz	-LOS propagation channel
[5]-[6]	Indoor	11GHz-23.5GHz	-Both LOS and NLOS propagation channel
[9]	Indoor	6GHz	-LOS and NLOS (First order reflection)
[10]	Indoor	30GHz-300GHZ	-Different size of room -Different operating frequencies -Different type of antennas
[11]	Indoor	433MHZ	-Using Raytracing tool -Empty room Scenario
[12]	Outdoor Vehicular Com.	60GHz	-Using Raytracing tool -3D beam patterns of beam training -MMW V2X communication
[15]	Outdoor Vehicular Com.	38GHz, 60GHz	-Two branch tapped delay -Wideband model
[17]	Outdoor Vehicular Com.	60GHz	-AoV measurements
[18]	Outdoor Vehicular Com.	28GHz	-V2V blockage
[19]	Outdoor Vehicular Com.	6.75, 30, 60, 73 GHz	-Inter vehicles blockage
[20]	Outdoor Vehicular Com.	28GHz	-Beam alignment
[22]	Outdoor Vehicular Com.	30GHz-300GHz	-Switching beams

1.3 Channel Modeling Approaches

Generally, channel modeling can be classified into three categories: stochastic channel models (SCMs), geometry-based channel models, and deterministic channel models. However, it's evident that none of these modeling approaches can singularly achieve the required accuracy and reliability for MMW V2V channels. Therefore, it makes more sense to evaluate which method aligns better with specific assumptions or demands of the MMW V2V system. Typically, stochastic and geometry-based models find more extensive application in system design and comparisons due to their ability to capture essential channel properties with relatively lower computational complexities. Geometry-based modeling provides valuable insights for system performance assessment by establishing direct relationships between channel parameters and system performance, often in closed form. On the other hand, deterministic modeling, yielding site-specific models, tends to be more favorable for system deployment. However, deploying deterministic models for MMW V2V systems demands an extensive database encompassing environmental characteristics. The high propagation loss in MMW V2V channels typically leads to sparse MPCs. Additionally, the propagation characteristics of MMW, like optical waves with small wavelengths, prompt a deterministic approach to modeling these channels. However, there remains an incomplete deterministic modeling framework for MMW V2V channels. In [23], a geometric optics-based deterministic model with four rays is proposed for 77-GHz V2V channels. Another study, [24], employs 2D deterministic modeling on a curved road with few vehicles, exploring propagation loss and Power Delay Profile (PDP) through simulations at 60 GHz. Meanwhile, [25] adopts a quasi-deterministic approach for 60-GHz outdoor peer-to-peer channel modeling, closely related to V2V applications. This model primarily accounts for the strongest propagation paths via ray tracing and incorporates additional random rays from scatterings and reflections using a stochastic approach. Notably, this model addresses challenges like human body shadowing and reflections due to moving vehicles, making it a non-stationary channel model. However, it lacks validation through actual V2V measurements.

Typically, the deterministic modeling of MMW V2V channels should address two key concerns: Firstly, understanding the electromagnetic properties of common materials in MMW V2V scenarios, such as road surfaces, vehicle bodies, traffic signs, and windshields. Secondly, examining the influence of scattering components at MMW frequencies, which holds significance in low-frequency bands and requires further exploration within the MMW spectrum.

1.4 Ray tracing

Site-specific algorithms have been introduced in various works, including those by McKown and Hamilton [26], Bertoni et al. [27], and others [28–33]. In these algorithms, we specifically estimate the local average of received power by summing the powers of all multipath components that arrive at the designated location. For each propagation path, we calculate the additional loss beyond the free space propagation loss. This additional loss is determined by multiplying the squared magnitude of reflection and transmission coefficients with the antenna radiation patterns. We compute the reflection and transmission coefficients for each object using a multilayer dielectric model while preserving their dependencies on angle and polarization. Moreover, we can accommodate an arbitrary number of surfaces, including walls, floors, or ceilings.

A ray is essentially the trajectory followed by an idealized particle that moves along a straight path but can also experience momentary interactions like reflections and refractions. Ray tracing is a straightforward technique used to track the advancement of wave fronts, with these ideal particles representing points on the traveling wave front. When applied to problems related to radio wave propagation, ray tracing serves as an approximation; Maxwell's coupled differential equations account for scattering effects that cannot be fully represented by simple particles. The accuracy of the ray tracing approximation

Table 2: Comparison of different methods in modeling of wireless channels.

Parameters/Methods	Measurements	Mathematical	Ray tracing
Computational Complexes		✓	✓
Costly	✓		
Time intensive	✓	✓	
Accuracy			✓
Material Penetration loss	✓		✓
Mathematical complexity for system deployment	✓	✓	
Specific geometric environment	✓		✓
Number of reflections, diffractions,..			✓
Various objects in the environment	✓		✓
Different pattern of antennas	✓		✓
Antenna configurations (Rotating, location, hight,..)	✓		✓
Angles of arrival and departure	✓		✓
Different operating frequencies	✓		✓

primarily hinges on the relationship between the wavelength of the waves, the size of scatterers, and the spatial volume of interest. In some cases, comparisons between ray tracing calculations and spatially averaged measured data are presented in [34]. Ray tracing yields the most accurate results when the observation point is significantly distant from the nearest scatterers in terms of wavelengths, all scatterers are considerably larger than a wavelength, and they exhibit smooth surfaces, meaning their surface features are much smaller than a wavelength. Distinguishing three distinct approaches (i.e., ray tracing tools, mathematical models, and measurements) in investigating the wireless channels, Table 2 compares some parameters including computational complexes, cost and time intensive, accuracy, and so on.

Wireless InSite®is an electromagnetic simulation software by Remcom designed to forecast how buildings and the landscape influence the behavior of electromagnetic waves.

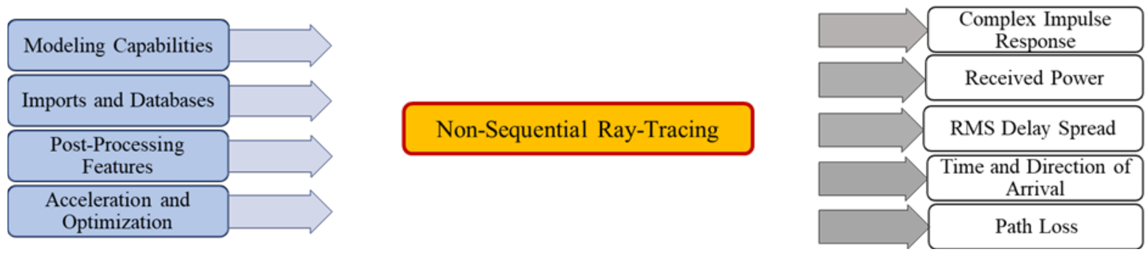

Figure 2: Steps in predicting propagation and channel characteristics.

It anticipates variations in signal strength caused by the placement of transmitters and receivers in urban environments. This tool replicates the structural attributes of uneven terrain and urban building structures, conducts electromagnetic computations, and subsequently assesses the characteristics of signal propagation. Fig. 2 presents the steps of channel modeling methodology from key inputs in Wireless Insite up to some calculations based on MATLAB®. In the first step, the major features including modeling capabilities, importing data, post-processing features, accelerating, and optimizing in Wireless Insite are provided. Under these properties, the software can predict radio propagation for indoor, indoor-outdoor, and terrain models with several modeling options such as high-fidelity ray tracing, Multiple-Input Multiple-Output (MIMO) simulations for 4G, 5G, Wi-Fi, and empirical propagation models. Also, a channel data analyzer for viewing, plotting, and exporting MIMO outputs by proper handling of antennas, polarization, phase, angle of departure, and arrival is considered to cover all desired analyses.

In the second step, the non-sequential ray-tracing program is interfaced with Wireless Insite GUI software to provide complex impulse response, RMS delay spread, Time of Arrival (ToA), and Direction of Arrival (DoA), path loss prediction, etc. It is worth noting that non-sequential ray tracing is applied to the system where the rays effectively find their way from source to receivers on the modeled wireless channel environment. Further details related to each step of channel modeling and characterization are elaborated in the following for planning indoor radio communication systems in Wireless Insite®as an example.

In an indoor environment, the transmitted signals by a fixed transmitter encounter multiple objects in the environment creating the reflected, scattered, and diffracted duplicates of the source signal. Reflecting objects consist of floors, ceilings, walls, doors, etc. Designers based on these characteristics from ray-tracing models can design and improve tools to match the channel propagation. Accordingly, RF propagation provides efficient and accurate predictions of electromagnetic propagation and communication channel characteristics for our area as outdoor or indoor environments. At every receiver site, the system combines and assesses the inputs from incoming ray paths to calculate anticipated parameters, including electric and magnetic field intensity, received power, measures of interference, path attenuation, delay distribution, arrival direction, impulse response, electric field over time, electric field across frequency, and the power delay profile.

In the following, let's clarify these parameters and details related to Wireless Insite®to acquire insight into the channel modeling and propagation mechanism of RF communication including MMW.

1.5 Channel Parameters

1.5.1 Received Power and Path Loss

Path loss is a metric that isolates the influence of transmitter power and the highest achievable gains of both the transmitter and receiver, resulting in a numerical representation of signal attenuation within the transmission budget. This attenuation accounts for factors like multipath propagation, transmission distance, interactions along each signal path, deviations from maximum gain in individual paths, polarization mismatches, as well as effects like constructive and destructive interference and atmospheric absorption. It's important to note that path loss does not encompass system losses, such as Voltage Standing Wave Ratio (VSWR) and Transmission Line losses, which impact received power [35]. The prevailing and widely accepted definition of path loss is:

$$PL_{\text{Max}}(\text{dB}) = P_t(\text{dBm}) - P_r(\text{dBm}) + G_{T,\text{Max}}(\text{dBi}) + G_{R,\text{Max}}(\text{dBi}) - L_S(\text{dB}) \tag{1.1}$$

where $G_{T,\text{Max}}$ and $G_{R,\text{Max}}$ are the maximum gains of the TX and RX antennas, respectively. L_S is the sum of all other losses in the system (in dB), including the bandwidth overlap factor. When dealing with directional antennas, the path loss varies according to the antenna's orientation. When incorporating path loss into a link budget, it's important to consider that it's not solely determined by the frequency and the environment, as is the case with Omnidirectional antennas. Assuming P_t as the transmit power, the total received power is then given by [[35], Eq. (21.1)]:

$$P_r = \sum_{i=1}^{N_p} P_i, \tag{1.2}$$

where the carried power by the i^{th} path (P_i), and N_P is the number of paths. P_i is given by [[35], Eq. (21.2)]:

$$P_i = \frac{\lambda^2 \beta}{8\pi\eta_0} |V_i|^2, \tag{1.3}$$

where λ is the wavelength and η_0 is the impedance of free space (377 Ω). The quantity β is the overlap of the frequency spectrum of the transmitted waveform and the spectrum of the frequency sensitivity of the receiver written in [[35], Eq. (21. 4) and (21.5)]. In (1.25) V_i is the voltage at the feed point of the receiving antenna [[35], Eq. (21.31)]:

$$V_i = E_{\theta,i} g_{R,\theta}(\theta_{A,i}, \phi_{A,i}) + E_{\phi,i} g_{R,\phi}(\theta_{A,i}, \phi_{A,i}), \tag{1.4}$$

while θ_i and ϕ_i are the parameters related to the direction of the arrival ray. The direction of arrival is given by [[35], Eq. (21.3)]

$$g_{R,\theta}(\theta_{A,i}, \phi_{A,i}) = \sqrt{|G_{R,\theta}(\theta, \phi)|} e^{j\psi_{\theta_A, i}}, \tag{1.5}$$

$$g_{R,\phi}(\theta_{A,i}, \phi_{A,i}) = \sqrt{|G_{R,\phi}(\theta, \phi)|} e^{j\psi_{\phi_A, i}}, \tag{1.6}$$

where $G_{R,\theta}(\theta, \phi)$, $G_{R,\phi}(\theta, \phi)$ are the theta and phi components of receiving antenna gain. $\psi_{\theta_A, i}$ and $\psi_{\phi_A, i}$ are the relative phase of the θ and ϕ components of the electric field at the i^{th} arrival path. Here, $E_{\theta,i}$ and $E_{\phi,i}$ are the so-called theta and phi components of the electric field of the i^{th} path at the receiver point (i.e., $E_i(r_i, \theta_i, \phi_i)$) [[35], Eq. (16.3)]:

$$E_i(r_i, \theta_i, \phi_i) = (A_\theta(\theta_i, \phi_i)\hat{e}_\theta + A_\phi(\theta_i, \phi_i)\hat{e}_\phi) \frac{e^{-j\frac{\omega}{c} r_i}}{r_i} \tag{1.7}$$

where

$$A_\theta(\theta_i, \phi_i) = \sqrt{\frac{P_t \eta_0}{2\pi}} g_{T,\theta}(\theta_{D,i}, \phi_{D,i}), \tag{1.8}$$

$$A_\phi(\theta_i, \phi_i) = \sqrt{\frac{P_t \eta_0}{2\pi}} g_{T,\phi}(\theta_{D,i}, \phi_{D,i}), \tag{1.9}$$

$$g_{T,\theta}(\theta_{D,i}, \phi_{D,i}) = \sqrt{\left|G_{T,\theta}(\theta, \phi)\right|} e^{j\psi_{\theta_{D,i}}}, \tag{1.10}$$

$$g_{T,\phi}(\theta_{D,i}, \phi_{D,i}) = \sqrt{\left|G_{T,\phi}(\theta, \phi)\right|} e^{j\psi_{\phi_{D,i}}}, \tag{1.11}$$

The directions of i^{th} departure path (i.e., $g_\theta(\theta_{D,i}, \phi_{D,i})$ and $g_\phi(\theta_{D,i}, \phi_{D,i})$) are given by [[35], Eq. (21.3)]. $G_{T,\theta}(\theta, \phi)$, $G_{T,\phi}(\theta, \phi)$ are the θ and ϕ components of the gain of the transmitting antenna.$\psi_{\theta_{D},\, i}$and $\psi_{\phi_{D},\, i}$ are the relative phase of the θ and ϕ components of the electric field at the i^{th} departure path. P_t is the power radiated by the transmitter and r_i is the total distance of the i^{th} path from the transmitter to the field point [[35], Eq. (16. 4)–(16. 8)]. The total received power by substituting (1.14) and (1.17) in (1.12) is [[35], Eq. (21.6)]:

$$P_r = \left(\frac{\lambda^2 \beta}{8\pi\eta_0}\right) \left|\sum_{i=1}^{N_P} E_{\theta,i} g_\theta(\theta_i, \phi_i) + E_{\phi,i} g_\phi(\theta_i, \phi_i)\right|^2, \tag{1.12}$$

(1.12) can be rewritten by taking the antenna patterns as

$$P_r = \left(\frac{P_T \lambda^2 \beta}{(4\pi)^2}\right) \left|\sum_{i=1}^{N_P} \frac{1}{r_i} \left(g_{T,\theta}(\theta_{D,i}, \phi_{D,i}) g_{R,\theta}(\theta_{A,i}, \phi_{A,i}) + g_{T,\phi}(\theta_{D,i}, \phi_{D,i}) g_{R,\phi}(\theta_{A,i}, \phi_{A,i})\right)\right|^2, \tag{1.13}$$

As an example, the received power due to the free space with the effect of the antenna patterns is [[35], Eq. (21.10)]:

$$P_r = \left(\frac{P_T \lambda^2 \beta}{(4\pi)^2 R^2}\right) \left|g_{T,\theta}(\theta_D, \phi_D) g_{R,\theta}(\theta_A, \phi_A) + g_{T,\phi}(\theta_D, \phi_D) g_{R,\phi}(\theta_A, \phi_A)\right|^2, \tag{1.14}$$

where θ_D and ϕ_D are the direction in which the ray leaves the transmitter, θ_A and ϕ_A are the direction from which the ray arrives at the receiver. R is the distance between the transmitter and the receiver. It is worth noting that the antenna gains of the receiver and transmitter points are included in $g_{R,(\theta,\phi)}$ and $g_{T,(\theta,\phi)}$.

Let P_t denote the transmit electrical power. The received power is given as

$$P_r = P_t \hat{H}_{\mathrm{MMW}}, \tag{1.15}$$

where $\hat{H}_{\mathrm{MMW}}$ is the overall $effective$ channel coefficient. Wireless Insite calculates it as

$$\hat{H}_{\mathrm{MMW}} = \left(\frac{\lambda^2 \beta}{8\pi\eta_0}\right) \left| \sum_{i=1}^{N_P} E_{\theta,i} g_\theta(\theta_i, \phi_i) + E_{\phi,i} g_\phi(\theta_i, \phi_i) \right|^2, \tag{1.16}$$

where λ is the wavelength and η_0 is the impedance of free space (377 Ω). The quantity β is the overlap of the frequency spectrum of the transmitted waveform and the spectrum of the frequency sensitivity of the receiver [35].

Note that the combined effects of transmitter/receiver antenna patterns and propagation environment are inherently captured by ray tracing in Wireless Insite. Therefore, as an alternative expression to (1.15), we can write

$$P_r = P_t \underbrace{G_R G_T H_{\mathrm{MMW}}}_{\hat{H}_{\mathrm{MMW}}}, \tag{1.17}$$

where G_T is the transmit antenna gain and G_R is the receive antenna gain. H_{MMW} is the channel coefficient and only includes the effect of the propagation environment. For calculating H_{MMW}, the arrival and departure angles of each ray and the antenna gains in both the transmitter and receiver sides are available in Wireless Insite [35]. The channel path loss (in linear scale), including the effect of antenna gains, is calculated by

$$PL_{\mathrm{MMW}} = \left(\frac{\lambda^2 \beta}{8\pi\eta_0}\right) \left| \sum_{i=1}^{N_P} E_{\theta,i} g_\theta(\theta_i, \phi_i) + E_{\phi,i} g_\phi(\theta_i, \phi_i) \right|^2, \tag{1.18}$$

Utilizing the non-sequential ray tracing feature with specified parameters like the number of rays and reflections, we compute the received power and the distances traveled by each ray from the source to the receiver. Subsequently, it is worth noting that Wireless Insite automatically generates various outputs (see Fig. 3) including the CIR, PDP, and P_r.

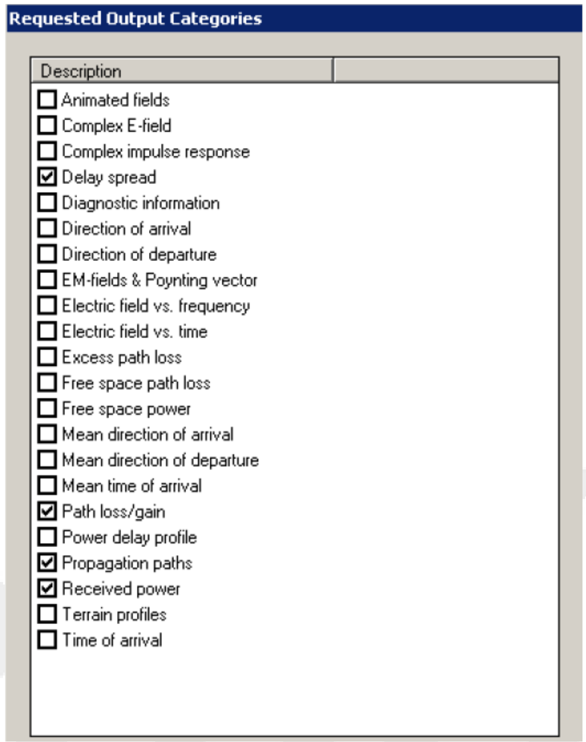

Figure 3: The requested outputs in categories.

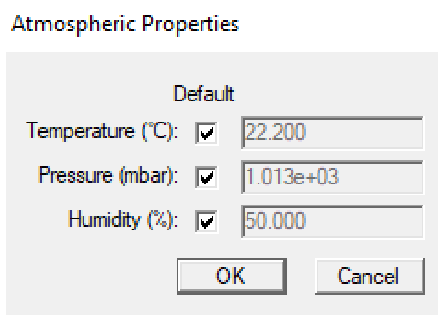

Figure 4: The X3D atmospheric properties window.

1.5.2 Atmospheric Attenuation

The X3D propagation model incorporates atmospheric absorption, broadening the scope of its wave propagation simulations to encompass millimeter-wave frequencies. It incorporates atmospheric attenuation and offers various unique capabilities, including Monte Carlo parameter variability, generating adjacent paths for highly efficient predictions in scenarios with dense receiver sets, and facilitating MIMO system analysis. The X3D model is equipped to handle atmospheric absorption due to oxygen and water. Input parameters, including temperature, relative humidity, and pressure, are incorporated into the X3D model's calculations for atmospheric absorption. A comprehensive explanation of the algorithm can be found in the following [35]. X3D ray model simulations incorporate absorption that varies with frequency, attributed to the presence of oxygen and water in the atmosphere. Users have the flexibility to define temperature, relative humidity, and pressure parameters within the X3D "Atmospheric-Properties" window (See Fig. 4), accessible through the "Atmosphere" button in the X3D study area properties window. The path loss and received power calculations are influenced by the distance traveled by a ray, frequency, and the specified atmospheric properties. By setting each field to zero, one can deactivate the absorption loss. The software employs an atmospheric absorption model adapted from a publicly available model introduced in [36]. This model's specific attenuation behavior, in relation to frequency, complies with the guidelines outlined in ITU recommendation ITU-R P.676-9 [37]. In Fig. 5a, we can observe the outcomes of the atmospheric absorption model integrated into Wireless InSite®, while Fig. 5b illustrates the loss as described in the ITU recommendation.

1.5.3 Material Penetration Loss

In Wireless InSite®, all features are fundamentally constructed using the "Materials" window. This manual collectively refers to the properties of a material as "Material Types". These material properties encompass both the electromagnetic characteristics of the surface and its visual display attributes. The reflection and transmission coefficients are directly derived from the material properties, while the diffraction coefficients are indirectly determined based on their relationship with the reflection and transmission coefficients. In some cases, the thickness of a material influences the reflection and transmission coefficients, whereas for others, it primarily affects the visual rendering of the surface. Regardless of material type, attributes like color and shininess only impact the visual representation of

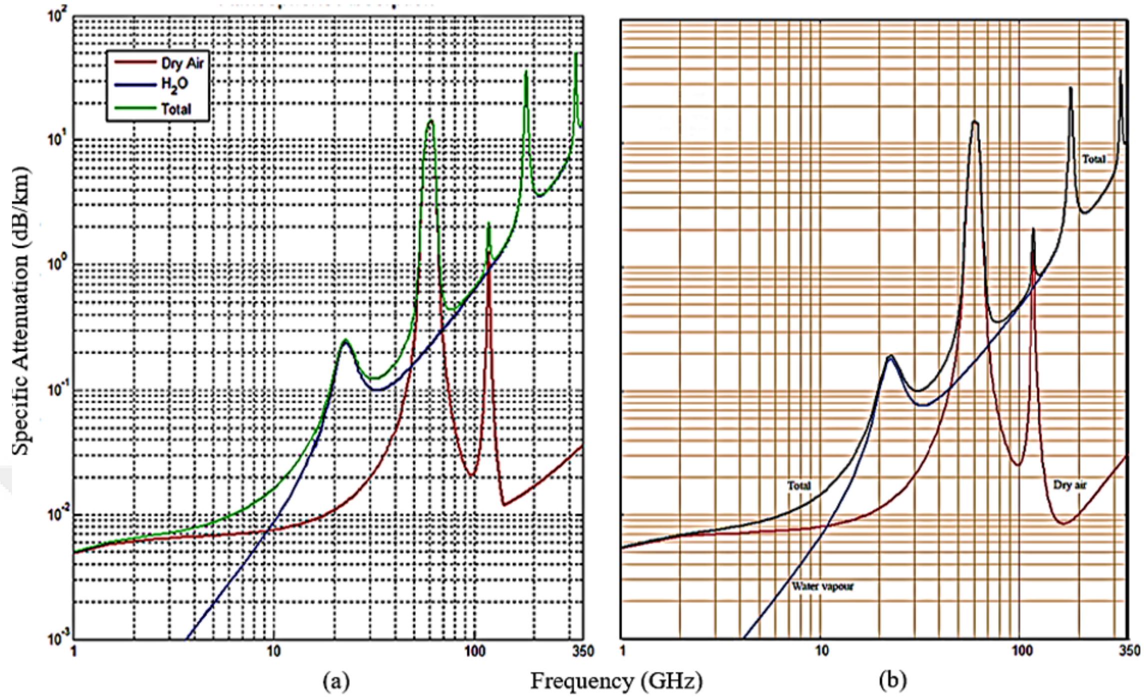

Figure 5: Specific attenuation as predicted by Wireless Insite' X3D.

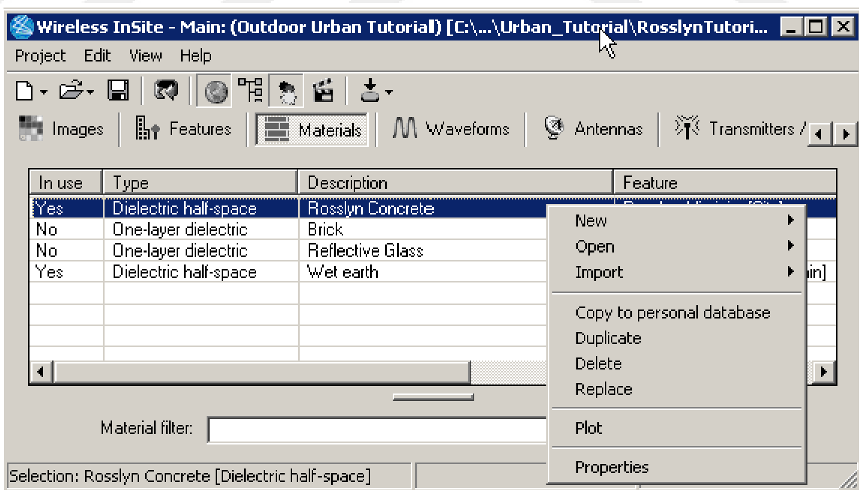

Figure 6: The list of materials under the Materials tab.

the surface. Wireless InSite®offers tools that make it easy for users to assign a material to individual surfaces or groups of surfaces. Additionally, these materials can be stored in the material database for use in other projects. The materials employed in a Wireless InSite ®project can be found in the material tab within the main window, illustrated in Fig. 6 [35].

The material properties for each feature are stored in the same file that contains the feature's geometric data. The properties window for each material type encompasses all the parameters that characterize the material. While certain values like thickness and roughness are found in each window, the majority of values are specific to a particular material type. The following is a compilation of typical fields that we encounter within the material properties window.

- **Roughness:** This parameter represents the standard deviation of the surface height in relation to the mean height, measured in meters.

- **Thickness:** It signifies the thickness of the material, also measured in meters. In some cases, the thickness is utilized to calculate reflection and transmission coefficients, while for other material types, it primarily affects the visual representation. For instance, even though a Dielectric Half-Space requires a thickness value, it doesn't influence the reflection and transmission coefficients, so entering a reasonable value (even zero) ensures the material is displayed correctly. Material types with multiple layers have a thickness value for each layer, with the total thickness influencing the display.

- **Permittivity (ε_r):** This field represents the material's permittivity, relative to the permittivity of free space (ε_0=8.85 $\times$ 10^{-12}). Some material types allow users to input one or more permittivity values, often focusing on the real part. However, for Foliage, a complex permittivity in the form of ($\varepsilon_r = \varepsilon' - j\varepsilon''$) is required.

- **Conductivity (σ_r):** Material conductivity is entered in units of Siemens per meter (S/m). Similar to permittivity, some material types allow the input of one or more conductivity values.

- **Reflection Coefficient (parallel), etc.:** When using a constant coefficient material, we can enter values for the reflection and transmission coefficients for the electric field, taking into account its polarization, either parallel or perpendicular to the plane of incidence.

- **Reflection/Transmission Coefficient Filename:** This field specifies the names of files that contain the reflection and transmission coefficients for a User-Defined Material.

- **DS Enabled:** When checked, this option activates Diffuse Scattering properties for the material, which can be further modified by clicking the Diffuse Scattering button.

The material database contains several frequently used building, ground, and foliage materials, along with a selection of generic material types. When any of these materials is assigned to one or more faces within a feature, the material properties are saved within the feature file, becoming an integral part of that specific feature. There is no ongoing connection to the database entry. Once material from the database is used for a feature, any adjustments made to the material's properties will only affect that particular feature, leaving the original properties of the material in the database unaltered.

Materials tend to influence signal propagation in varying ways depending on the frequency of the radio waves they encounter. Wireless InSite®offers a range of material definitions in its database, aligned with ITU recommendations, designed for four typical Wi-Fi and 5G millimeter-wave frequencies. The characteristics of building materials are determined using the equations outlined in [38], while those for soil are derived from the data presented in [39]. Tables 3 and 4 display the relative permittivity and conductivity in S/m of these materials in Wireless InSite®. As shown in Fig. 7a and 7b, it becomes evident that, in the case of numerous materials, the ITU recommendations indicate a relatively consistent relative permittivity across different frequencies, while the conductivity exhibits notable variations within this frequency range.

Table 3: Properties of included Wi-Fi frequency-sensitive material

	2.4 GHz		5 GHz	
Material	**Relative Permittivity (ε)**	**Conductivity (σ)(S/m)**	**Relative Permittivity (ε)**	**Conductivity (σ)(S/m)**
Concrete	5.31	0.0662	5.31	0.1199
Drywall	2.94	0.0215	2.94	0.0362
Wood	1.99	0.0122	1.99	0.0263
Glass	6.27	0.0122	6.27	0.0293
Ceiling board	1.5	0.0013	1.5	0.0032
Floor board	3.66	0.0143	3.66	0.0387
Very dry ground	3	0.0013	3	0.0086
Medium dry ground	13.7426	0.1458	12.77	0.4823
Wet ground	21.1366	0.4681	15.75	1.2154

Table 4: Properties of included 5G frequency-sensitive material

	28 GHz		60 GHz	
Material	**Relative Permittivity (ε)**	**Conductivity (σ)(S/m)**	**Relative Permittivity (ε)**	**Conductivity (σ)(S/m)**
Concrete	5.31	0.4838	5.31	0.8966
Drywall	2.94	0.1225	2.94	0.2102
Wood	1.99	0.1671	1.99	0.3783
Glass	6.27	0.2286	6.27	0.5674
Ceiling board	1.5	0.0241	1.5	0.0585
Floor board	3.66	0.3974	3.66	1.1133
Very dry ground	3	0.3	3	0.75
Medium dry ground	5.7	6.5	4.3	14
Wet ground	5.7	9.5	4.3	15

1.5.4 Radio Channel Propagation Mechanisms

Wireless InSite®offers a variety of ray-based propagation models, including X3D, FULL 3D, URBAN CANYON, and VERTICAL PLANE [35]. These models employ a combination of ray-tracing algorithms along with Geometric Optics (GO) and the Uniform Theory of Diffraction (UTD) [40], [41], [42]. Ray-tracing techniques are utilized to determine the propagation paths connecting transmitter and receiver locations. Subsequently, physical principles such as GO and UTD are employed to assess the complex electric fields linked to each of these ray paths.

The Shooting and Bouncing Ray (SBR) method is initially used to compute ray paths

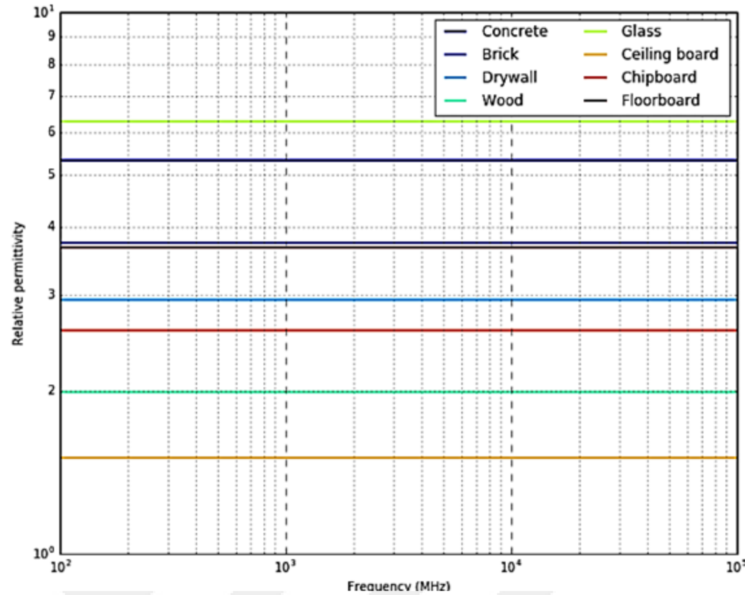

(a)

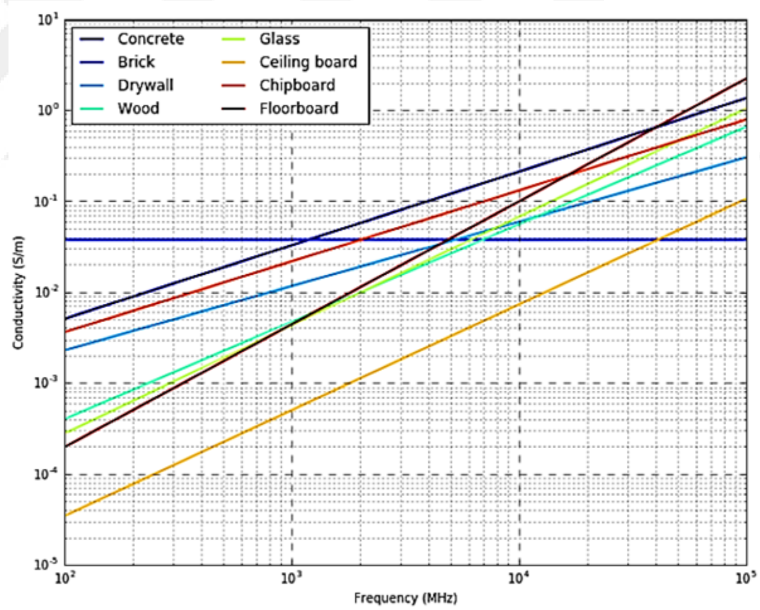

(b)

Figure 7: (a) Relative permittivity vs frequency, (b) Conductivity vs frequency.

through the three-dimensional building geometry without considering the specific locations of field points. This procedure, as outlined in [43] and [44], involves tracing rays originating from source points. These rays undergo specular reflection upon hitting the building walls and are continuously traced until reaching the maximum number of reflections or intersecting the boundary of the study area.

Fig. 8 illustrates the rays emitted from the source point, terminating either at the first reflection point on a building wall or at the intersection with the boundaries in different study areas from Indoor to Outdoor scenarios. It's worth noting that the ray density depicted in the figures is significantly lower than that used in actual calculations. When determining the number of rays to generate, there are two key factors to consider. The primary factor is to establish a sufficiently dense spacing of the SBR rays to guarantee that a minimum of two rays along each distinct ray path intersect the encompassing collection surface near each field point. The estimate of the angular spacing in radians is:

$$\Delta\phi \approx \frac{R_{collect}}{D_{\max}} \tag{1.19}$$

where D_{max} is the maximum distance across the area being considered, and $R_{collect}$ is the radius of the collection sphere [35]. The secondary factor involves assessing the ray spacing concerning the geometry. It is essential to choose a spacing small enough to ensure that at least two rays intersect most of the visible faces from the receiver's perspective. While this condition is usually met by considering the ray spacing relative to the collection surface, in certain cases, it may be the decisive factor in selecting an appropriate ray spacing. Based on practical experience, it has been observed that a ray spacing of 0.2° meters and a collection surface with a radius of 2.5 meters are effective in most scenarios. The SBR method can calculate ray paths with a maximum of 30 total reflections and transmissions, including diffractions. However, it's important to note that when both reflections and transmissions are included, the computation time can become significantly longer. The computation time is approximately proportional to the following factors:

$$\frac{(N_R + N_T + 1)!}{N_R!N_T!} \tag{1.20}$$

where N_R and N_T are the number of reflections, and transmissions, respectively. In the absence of diffraction calculations, the computation time will be roughly in proportion to the number of facets in the geometry, considering double-sided facets as two separate facets. If a single diffraction calculation is requested, the computation time scales approximately

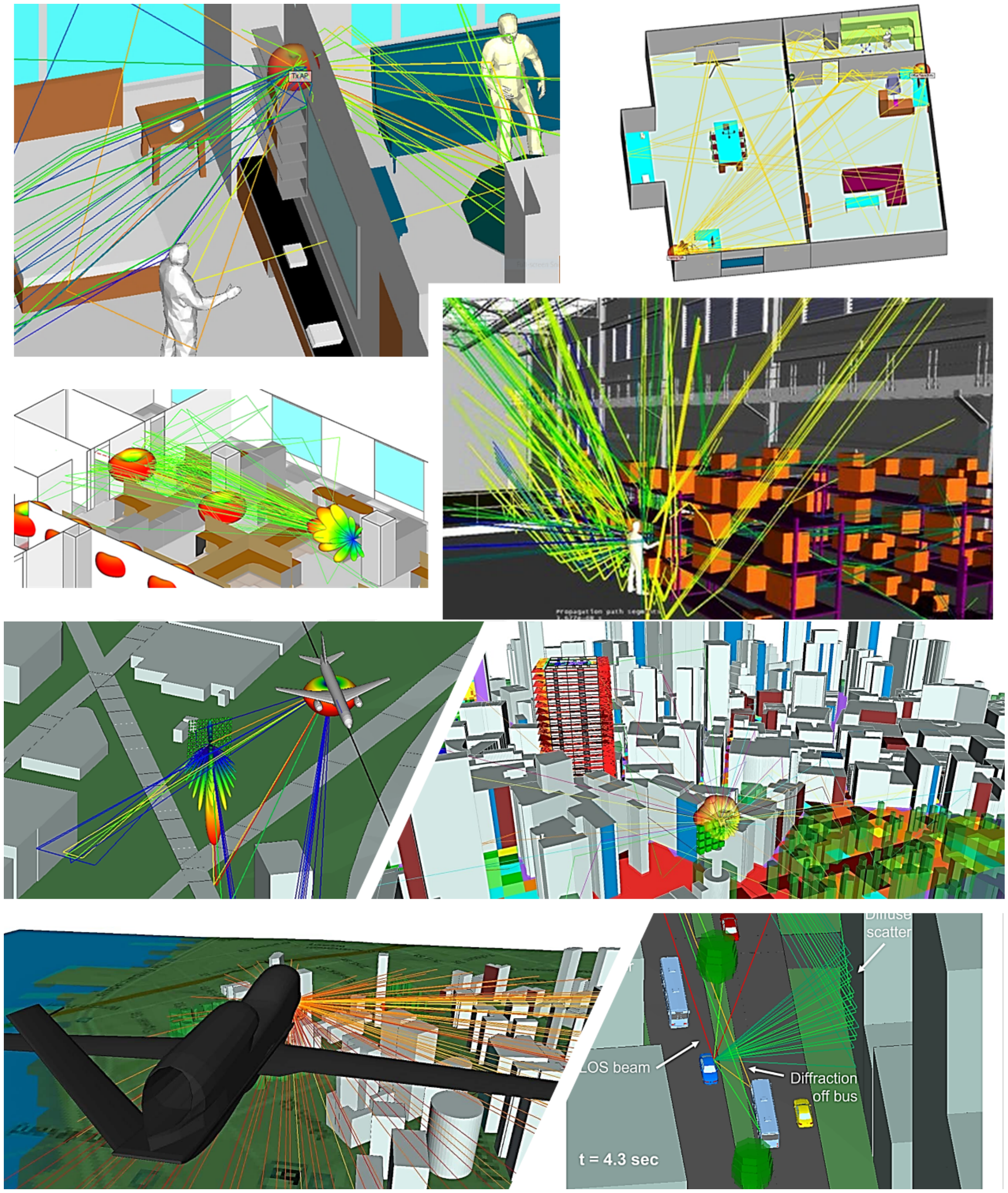

Figure 8: Ray emission by Ray tracing tool in different study areas from Indoor to Outdoor scenarios.

with the square of the number of facets. The inclusion of additional surface diffractions doesn't significantly impact the runtime due to the constraint related to coplanar edges [35].

Wireless InSite's diffuse scattering model enables the simulation of scattered paths resulting from natural imperfections in real-world structures and materials. It provides reasonably accurate results without requiring highly detailed project geometry. It's important to note that diffuse Scattering outputs are exclusively produced for study areas employing the X3D model. Wireless InSite's diffuse scattering model is founded on the framework established by Degli-Esposti in 2007 [45], with additional adjustments introduced for cross-polarization based on his subsequent work in 2011 [46]. The core idea behind this model is that electromagnetic waves scatter from building surfaces in a stochastic manner, radiating in all directions beyond simple specular reflection. This phenomenon is known as diffuse scattering. It involves a reduction in the standard Fresnel coefficient for specular reflection, compensating for the influence of power scattered in a diffuse manner. Wireless InSite supports three models for calculating diffusely scattered fields including the Lamberian, Directive, and Backscatter models. By selecting three models and associated parameters including Lambertian, Directive, and Directive with Backscatter the user can define how scattering takes place for each material and how strong the scattering is (See Diffuse scattering properties window in Fig. 9). The scattering factor represents the fraction of the incident ray that is scattered diffusely by the valid values ranging from 0 to 1 for no diffuse and completely diffuse scattering, respectively. The cross-polarization fraction K introduces the diffused power fraction relative to the polarization of the incident ray which is cross-polarized.

The Lambertian model has a scattering pattern that normally centers around the wall regardless of the incidence direction as the blue incident rays in Fig. 10. The fraction of the diffusely scattered field for this model is defined by the scattering coefficient input. The second model is named the directed model scatter which spreads out around the direction of occurred reflection shown with green rays in Fig. 10. In addition to the two parameters i.e., scattering and cross-polarization factors, a third parameter called Alpha defines how narrow forward scattering will be and it has a value between 1 to 10. The directive model with backscatter is the third model taken by Wireless Insite®as shown in red rays. In this model, a forward directive beam still that follows the reflection way is observed but there is also an added scatter beam in the backward direction. This one would happen

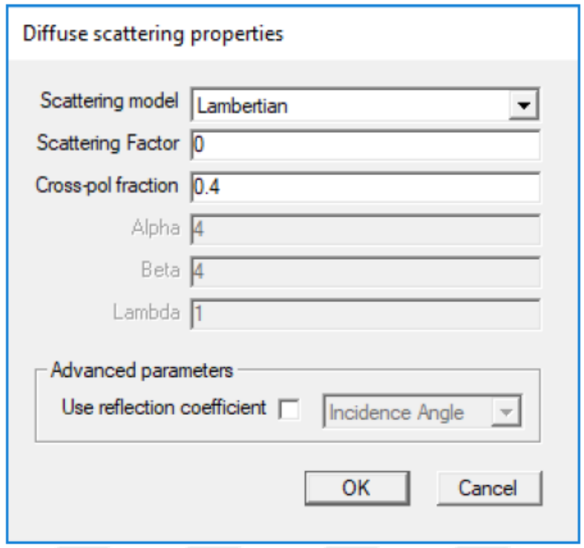

Figure 9: Diffuse scattering properties Window.

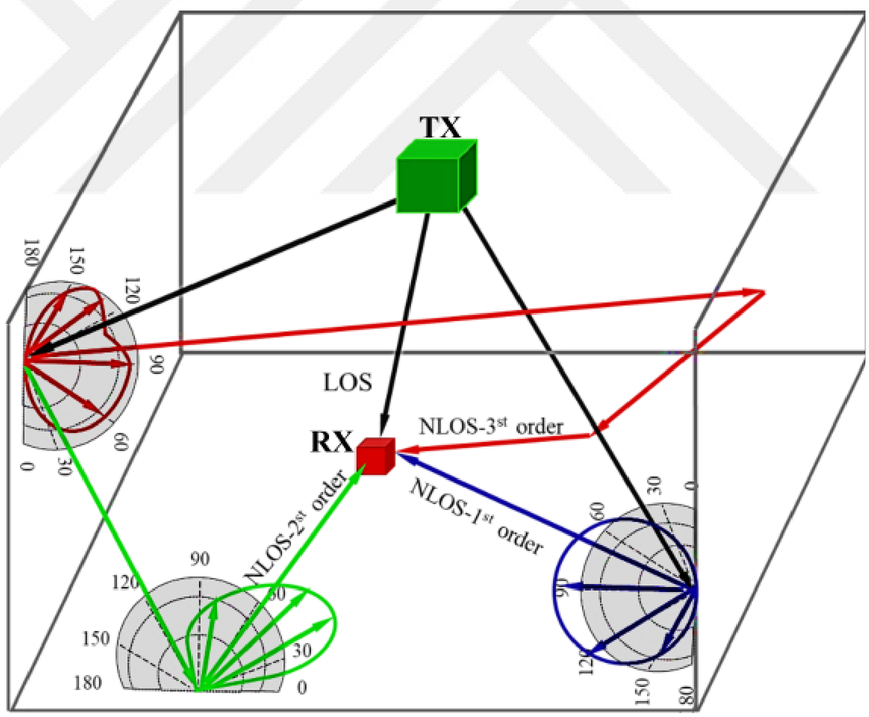

Figure 10: Diffuse scattering and path interaction for indoor environment.

if the diffused scattering included lots of right angles some of them effectively are corner reflectors. Therefore, scattered energy that goes back toward the transmitter leads to defining two additional parameters as Beta between 1 and 10 for determining how strong that backscatter is going to be. The second additional fraction is Lambda to describe how much of the forwarded energy is scattering as opposed to the back direction. The default values in Wireless Insite®for α, β, and Λ are 4, 4, and 0.75, respectively.

The complex impulse response related to the i^{th} arrival path [[35], Eq. (21.32)] and total complex impulse response as an output result of Wireless Insite®is considered to be:

$$s_i = P_i e^{j\psi_i}, \tag{1.21}$$

$$S = \sum_{i=1}^{N_p} s_i \delta(t - t_i) \tag{1.22}$$

where the carried power by the i^{th} path (P_i), and the associated phase (ψ_i) were defined in (1.3) and (1.23) [[35], Eq. (21.32)] as:

$$\psi_i = \tan^{-1}\left(\frac{\mathrm{Im}(V_i)}{\mathrm{Re}(V_i)}\right), \tag{1.23}$$

t_i is the time of arrival for the i^{th} path as:

$$t_i = \frac{L_i}{c}, \tag{1.24}$$

where L_i is the total geometrical path length, c is the speed of light in free space.

The delay spread serves as a valuable metric for assessing multiple effects associated with multipath propagation. It represents the RMS of time delays, weighted by signal power, and is computed under the assumption of a narrowband signal at the carrier frequency. This calculation is performed according to the formula provided in [47]:

$$\sigma = \sqrt{\frac{\sum_{i=1}^{N_P} (t_i - \bar{t})^2 P_i}{P_r}}, \tag{1.25}$$

where $\bar{t}$ is the mean time of arrival given by:

$$\bar{t} = \frac{\sum_{i=1}^{N_P} P_i t_i}{P_r}. \tag{1.26}$$

1.6 Dissertation Outline

Our primary objective is to create realistic channel models for MMW in various environments, including indoor, outdoor, and vehicular mediums. Our approach leverages Wireless Insite®, a site-specific software primarily designed for RF system design. We exploit the ray tracing capabilities of this software, which enable accurate modeling of how RF rays interact within a defined enclosed space when emitted from a transmitter antenna as a source.

In the first phase of our research, we concentrate on indoor channel modeling. Our proposed approach has the capability to generate CIRs, received power, and path loss results for different types of TX/RX antennas, operating frequencies, locations of antennas, and positions of trajectories, distinguishing it from previous methods that relied on just a feature. Moreover, it can seamlessly account for diffuse, specular, and mixed reflections. Additionally, our approach accurately incorporates objects and considers the wavelength-dependent reflective properties of surface materials in channel modeling. To validate the accuracy of our approach, we first demonstrate its ability to produce the same CIR and received power as existing literature when assuming purely diffuse reflections and ideal Lambertian scattering. As part of our case studies, we examine a range of indoor scenarios classified into 100 small cells. In these considered environments, we derive CIR and present a channel characterization analysis, extracting parameters such as received power, path loss, and root mean square delay spread. Furthermore, we perform direct comparisons between VLC and RF communication results for the same environments, highlighting the distinctions between these two communication bands.

In the second phase of our research, we focus on channel modeling for V2V MMW Communication systems, specifically in Intelligent Transportation System (ITS) scenarios. We meticulously account for the impact of lateral shifts, density of vehicles, and LOS blockage. We also consider practical operating conditions, including reflections from road surfaces, and factor in varying weather conditions throughout our channel modeling investigation.

The author has published several of the main ideas in this dissertation as part of her research. These include:

1. A practical indoor RF channel modeling approach that considers real-world factors such as wavelength-dependent reflection coefficients, different types of antennas, different locations of antenna, different trajectories, different operating frequencies, the effect of scattering, and a higher number of reflections is presented in [48].

2. A closed form received power expression for indoor RF channel in different frequencies is given in [48].

3. A realistic V2V MMW channel modeling taking into account the real-world factors such as wavelength-dependent reflection coefficients of road, different lateral shifts, different densities of vehicles, and the effect of blockage due to different densities of cars is presented in [49].

1.7 Organization

The rest of the dissertation is organized as follows. In Chapter II, we first review the existing indoor channel modeling approaches and highlight their shortcomings. Then, we propose an RF/MMW channel modeling approach based on non-sequential ray tracing features of Wireless Insite ®and present a comprehensive channel characterization study for various frequencies. In Chapter III, we present vehicular RF channel models for various configurations such as vehicle-to-vehicle, the effect of lateral shift, the effect of density of vehicles, and the effect of LOS blockage. In Chapter IV, the future works related to RIS-aided MMW/THz channel modeling are presented. Finally, Chapter V concludes and summarizes this dissertation.

CHAPTER II

CHANNEL MODELING AND CHARACTERIZATION FOR INDOOR MMW COMMUNICATIONS

2.1 Introduction

More than 70 % of wireless voice and data traffic takes place in an indoor environment [50, 51]. Low-cost and high-data-rate solutions are required to enable ubiquitous indoor wireless connectivity as well as avoid congestion in the radio frequency spectrum. The omnipresence of Light Emitting Diode (LED)s in indoor environments provides a unique opportunity for VLC to exploit the existing illumination infrastructure for wireless access [52–54]. VLC has therefore emerged as a complementary solution to RF-based wireless systems [55–58]. While the millimeter-wave and visible light are different in nature, they exhibit some similarities due to operating at higher frequencies compared to sub-6 GHz systems [59, 60]. It is therefore critical to explore the fundamental characteristics of these two technologies.

Most of the earlier works focus on individual technology and do not present a one-to-one comparison of indoor MMW and VLC channels. To the best of our knowledge, the only prior works that attempt to make such a comparison are [61, 62]. The work in [61] compared the channel modeling of both the VLC and MMW systems in an empty room based on a simple path loss model. The path loss and time dispersion were calculated for both MMW and VLC assuming different antenna gains for 28, 60, and 73 GHz and VLC bands. The work in [62] used a ray tracing tool to compare the channel characteristics of VLC/RF indoor systems assuming 7 hexagonal micro-cells.

In this chapter, we compare the propagation channels of RF and VLC spectra for the same indoor environment and scenarios. Several RF frequencies are considered, including

2.4 GHz, 6 GHz, 28 GHz, 60 GHz, 100 GHz. We benefit from the advanced features of the ray-tracing methodology for modeling both the VLC and RF propagation channels. We take into account the realistic models of the indoor environment, the objects inside, and the typical antenna radiation patterns. Taking into account the impact of the LOS, reflected, refracted, and scattered rays, we investigate the channel characteristics for different user positions, receiver locations, and user trajectories (i.e., diagonal, vertical, and horizontal paths). We analyze the results of CIRs and the channel path loss for different positions of users, frequencies, locations of receivers, and antenna types. The obtained results demonstrate that the propagation channel characteristics are highly dependent on the antenna type as well as the geometry of the user and the receiver's location.

The rest of this chapter is organized as follows: In Section 2.2, we describe channel modeling methodology. In Section 2.3, we describe the indoor scenarios under consideration. Section 2.4 provides simulation results and discussions.

2.2 Channel Modeling Methodology

We use Remcom's Wireless Insite [35] software tool for MMW indoor channel modeling. To have a precise characterization of the signal interaction with the environment, this simulator builds upon advanced non-sequential ray tracing features to enable integration of the realistic source radiation patterns and wavelength-dependent reflectance of the surface coating. It can be noted that the channel models obtained by the considered ray tracing methods have been validated by real measurement/empirical data [63–66]. For instance, related to MMW the authors in [63], demonstrated through experimental validation at 100-300 GHz that the ray tracing method is an effective and highly accurate channel modeling approach for MMW and Terahertz (THz) channels.

2.2.1 RF Channel Modeling

Ray tracing is a classical deterministic method for analyzing site-specific radio wave propagation. It builds upon the geometrical optic and uniform theory of diffraction to model the interactions between the rays and objects, including the reflection from various surfaces, transmission via indoor objects, scattering, and diffraction from edges.

In the following, we describe the main steps in our simulation study. First, we create a Three Dimension (3D) model of the indoor environment in the Wireless Insite®where the Computer Aided Design (CAD) models of a human and a cell phone are imported, see Figure 11. Then, the Transmitter (TX) and Receiver (RX) specifications including antenna type, radiation pattern, orientation, etc are defined. Maximum gain, polarization, aperture/feed width and height, and feed-aperture length are additional inputs related to antenna type characterization. In the simulations, rays originating from the transmitter encounter objects (i.e., indoor surfaces, the human body, etc.), and the losses in the strength of the propagating signal depend on the electrical features of the surface materials. The frequency dependence of surface materials in terms of permittivity, conductivity, and thickness [67] to characterize these interactions are further taken into account. For example, the reflections of the walls, floor, and ceiling are characterized as a mix of specular and diffuse in our study while the reflections of the cellphone with metal material are modeled as specular [68]. The reflection type in materials can be determined by the "scatter fraction" parameter in the X3D propagation model of Wireless Insite (See Fig. 10). This parameter varies between 0 and 1 such that zero indicates the purely specular reflections and unity notes the purely diffuse case.

The SBR method is used in Wireless Insite [69] to obtain the CIR. The rays are launched with angular spacing and traced back to the RXs. The CIR consists of LOS rays as well as n^{th}- order NLOS rays related to the floor, ceiling, walls, and objects. Wireless Insite can generate specific outputs such as received power, path loss, and CIR automatically by selecting those items in the output window. It is worth noting that generating CIR, PL, and P_r in Wireless Insite®follows the equations in Sections 1.5.

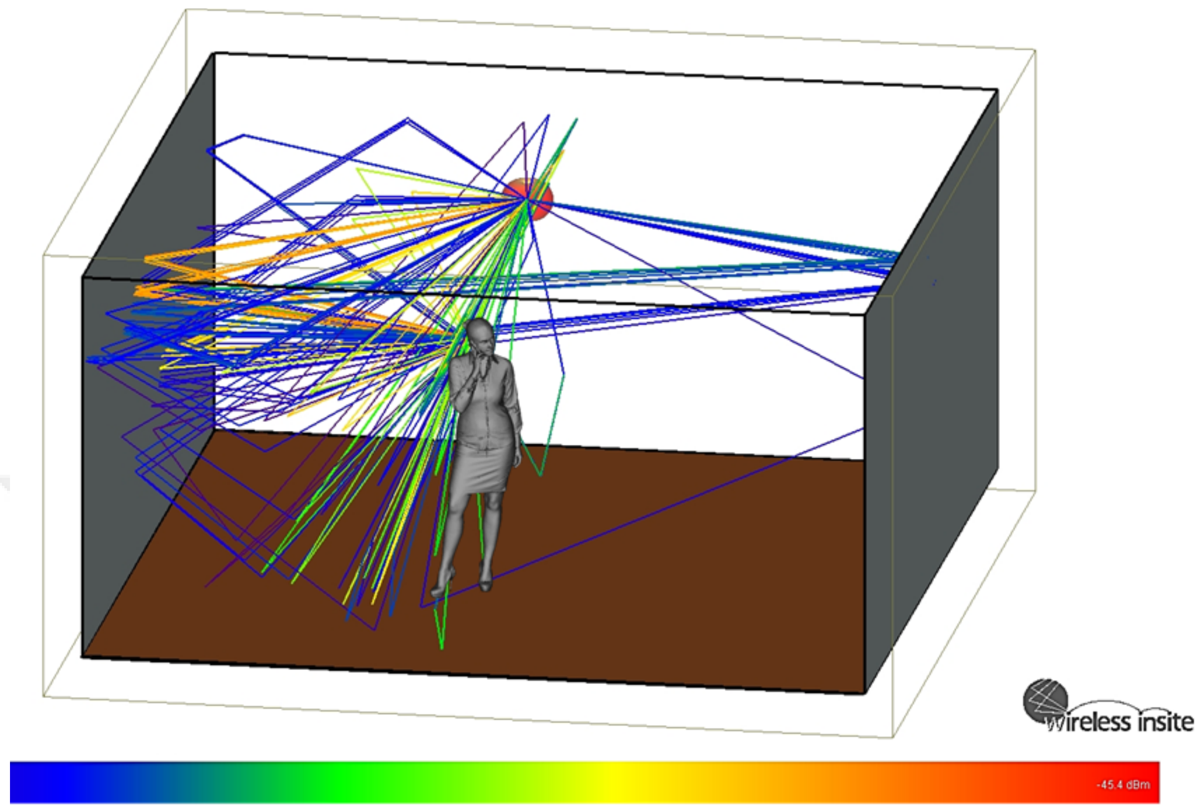

Figure 11: Modeling layout for MMW system

2.3 Indoor Scenarios

Our simulation environment is an empty room with a size of 6 m $\times$6 m$\times$3 m shown in Figure 12. We consider 100 cells with an equidistant spacing of 0.6 m in x and y directions to investigate the effects of user locations as well as the effect of antenna locations. A user holding a phone in his hand next to his ear with 45° rotation upward to the ceiling with a height of 1.8 m is modeled. The cell phone has a size of 5.5 cm $\times$ 10.5 cm $\times$ 0.5 cm [68]. The radiation patterns of the RF antennas are illustrated in Figure 13, which include (a) omnidirectional antenna, (b) directional horn antenna, and (c) patched antenna. Horn antenna and rectangular patch antenna have a simple structure, directional performance, high gain, wide bandwidth, and peak power handling capability. The last two advantages come from the fact that horn antennas do not have resonant elements. To have a fair comparison with VLC, we consider pyramid horn and rectangular patch antennas with a peak gain of 1

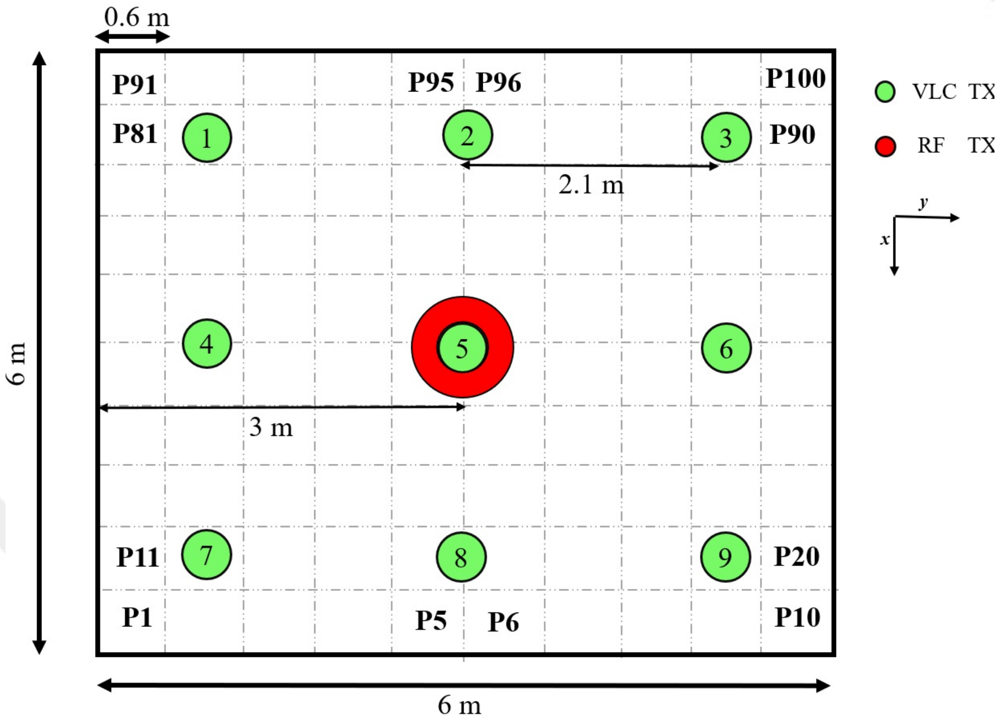

Figure 12: MMW and VLC indoor system under consideration.

dBi and the same area of VLC receivers (i.e., 1 cm^2). These antennas are used in a beam alignment procedure in which RX orients its antenna to the direction for receiving the most powerful signal. The calculation for finding the feed/aperture sizes of the horn antenna parameters is based on [70, 71] presented in the Appendix. In our simulation, the coating materials for walls, the ceiling, the floor, the cell phone, and the human are considered as concrete drywall, wood, black glossy metal, and absorbing skin. The frequency dependence of material features can be characterized in terms of permittivity and conductivity. Table 5 presents the relative permittivity and conductivity of different materials. Table 6 provides the whole simulation parameters of the simulator including the antenna pattern. We consider the unit gain for all results including path loss and received power.

The 3D views of Fig. 14, show the path of each scenario under consideration to investigate the MMW and VLC propagation channels. However, Fig. 15 illustrates the up-side 2D view of different trajectories at the same sight. For the VLC system, 9 LEDs located on the ceiling act as wireless transmitters (drawn by the green circles on the ceiling in Figure

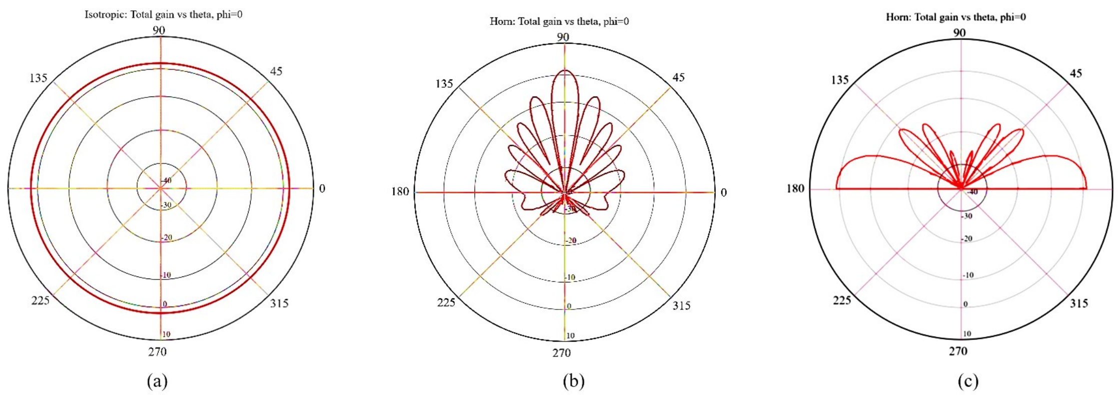

Figure 13: Radiation patterns: (a) isotropic omnidirectional antenna, (b) directional antenna, (c) rectangular patch antenna.

Table 5: Material characteristics at different frequencies.

Material		Concrete	Wood	Metal	Skin
Relative permittivity (ε_r)		5.31	1.99	0.98	10.5
Conductivity (σ_r)	**2.4 GHz**	0.0662	0.012	3.88	1.56
	6 GHz	0.123	0.027	3.02	3.95
	28 GHz	0.48	0.167	1.98	5.32
	60 GHz	0.89	0.378	1.28	7.32
	100 GHz	1.05	0.46	0.58	9.01

12 and denoted by VLC TX in legend) while a single antenna represents the RF transmitter (drawn by the red circles on the ceiling in Figure 12 and denoted by RF TX in legend). The cell phone is equipped with five receiver units denoted by RX1-RX5 as shown in Figure 16. The RXs are distributed around the cell phone in a way to cover all possible directions where the rays can come from either directly or via reflection. To develop various snapshots of indoor communication in a room, six different scenarios are considered for the user by moving through trajectories (denoted by T_1, T_2,..., T_6, See Fig. 14 and 15) as detailed below:

- **Scenario 1 (Figure 14a):** In this scenario, we consider all cells in T_1 which the user moves horizontally from the left to the right side of the room marked by the red rectangular in Figure 15a. The cell phone is in the right hand of the user and it is

Table 6: Simulation parameters for room and transceivers.

Parameters	Wireless Insite (RF)	OpticStudio (VLC)
Room Size	6 m× 6m× 6m	
Room surface material	Wall: Concrete Floor: Pine Wood	
Scattering / Cross polarization Factors	Lambertian R2(0.5-0.5) (Mixed diffuse and specular) (Alpha=4, Beta=4, Lambda=0.75)	
Objects specifications	Cell Phone: Metal (Black gloss paint) Human: Face Skin and Absorbing	
No. of TX	1	9
Antenna type	Omnidirectional / Directional/ Rectangular Patch	Indoor Luminaries (Lambertian)
Total Transmit Power	12 W	
Operating frequency	2.4 GHz, 6 GHz, 28 GHz, 60 GHz, 100 GHz	VLC (400–700 THz)
No. of Reflections	6	
Channel Model	Ray Tracing	
No. of RXs	5	
Area of RX **Field of View (FoV) Angle**	1 cm^2 90°	

directed to the inner room side.

- **Scenario 2 (Figure 14b):** This scenario considers the cells near the north wall of our room as T_2 shown by the red rectangular in Figure 14b. The user holds the cell phone in his right hand and changes his location from the right to the left side of the room. The cell phone is directed to the wall.

- **Scenario 3 (Figure 14c):** In this scenario, the human walks vertically from down to up near the west wall of the room to get the results of all cells in T_3, shown by the blue rectangular in Figure 14c. The cell phone is located in the right hand of the user-looking wall and completely covered by the head of the human and the wall.

- **Scenario 4 (Figure 14d):** In this scenario, all cells of T_4 are captured from down to up near the east wall of the room to investigate the results of all antennas in the cell phone (See blue rectangular in Figure 14d). The cell phone is directed to the inner side of the room.

- **Scenario 5 (Figure 14e):** The light blue cells located on the diagonal of Figure 15e illustrate T_5. The user moves from one corner to the opposite one diagonally by holding the cell phone in his right hand.

- **Scenario 6 (Figure 14f):** The light green colours in Figure 14f denotes cells of T_6. Through this trajectory, the human holds his cell phone near his ear and changes his position from the right-south corner up to the left-north side.

2.4 Simulation Results and Discussions

In this section, we present simulation results for MMW channel of indoor scenarios in comparison with VLC channel described in the previous sections.

As the extensive use of wireless technology has led to the study of radio wave propagation in different environments like complex building indoor structures, wireless systems have to take into account several propagation effects. Channel modeling does not depend only on LOS, because the waves encounter various obstacles from walls, floor, furniture, human body, etc., with different materials, as shown in Fig. 11. Wireless Insite considers the diffuse scattering models by revealing how paths interact with different surfaces and structures. Also, this can demonstrate how power strength is affected by the type of materials, especially in the millimeter-wave spectrum as a forced expansion of 5G technology.

The IEEE 802.11ay standard builds upon the previous 802.11ad system operating in the 60 GHz band, introducing new use cases and scenarios that demand a fresh approach to describing the millimeter-wave channel. The proposed channel modeling approach for the IEEE 802.11ay standard is based on a method known as quasi-deterministic (Q-D)

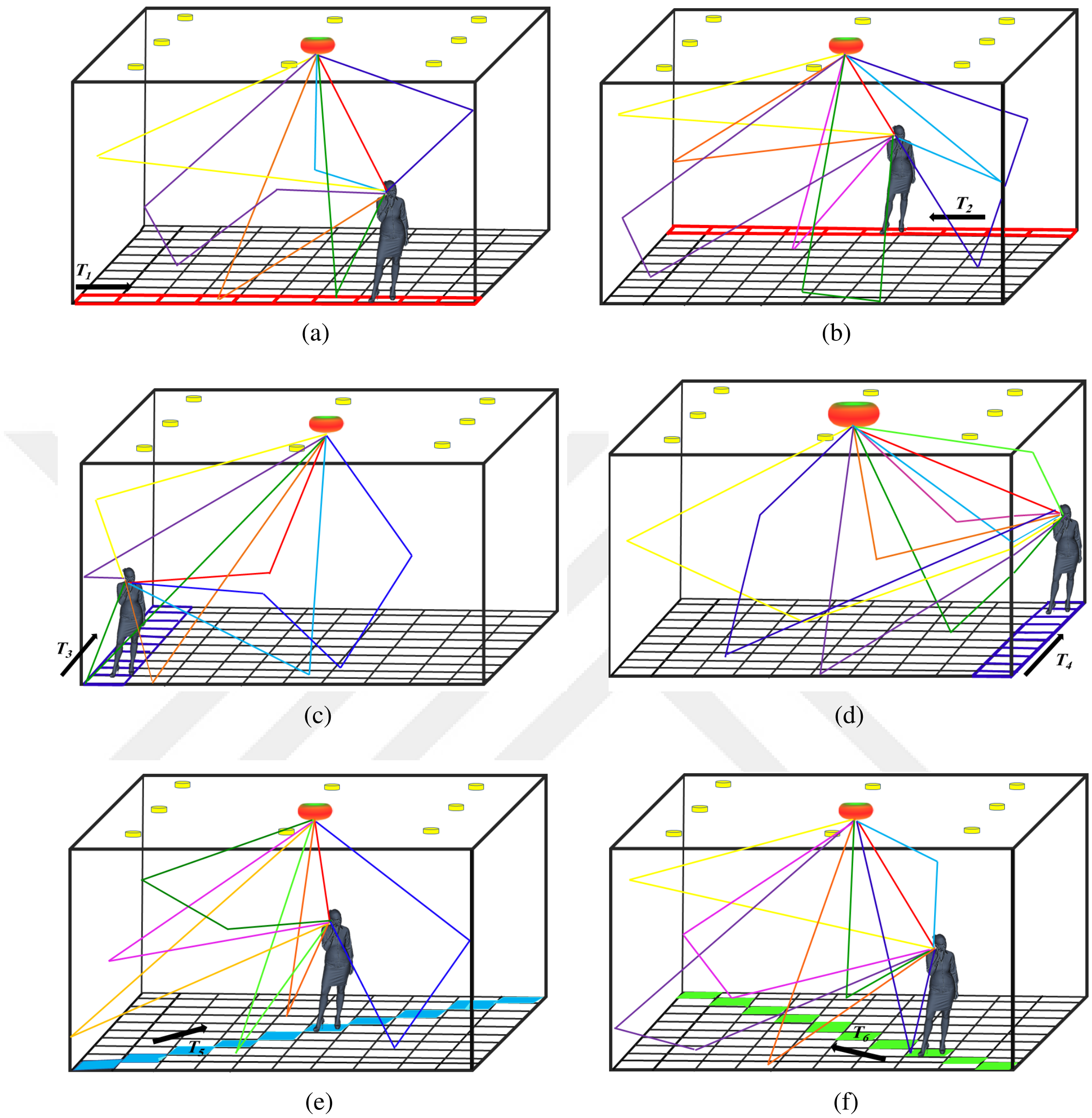

Figure 14: Indoor MMW/VLC Scenarios, (a) Cells of T_1 related to Scenario 1, (b) Cells of T_2 related to Scenario 2, (c) Cells of T_3 related to Scenario 3, (d) Cells of T_4 related to Scenarios 4, (e) Cells of T_5 related to Scenario 5, (f) Cells of T_6 related to Scenario 6.

methodology. This approach combines deterministic and stochastic elements in describing the environment, facilitating the incorporation of scenario-specific geometric characteristics, reflection attenuation, ray blockage, mobility effects, and accurate MIMO channel models. In line with this methodology, the 3D channel impulse response is represented as a combination of several quasi-deterministic strong rays (referred to as D-rays). These D-rays originate from prominent scenario-specific large reflecting surfaces. Additionally,

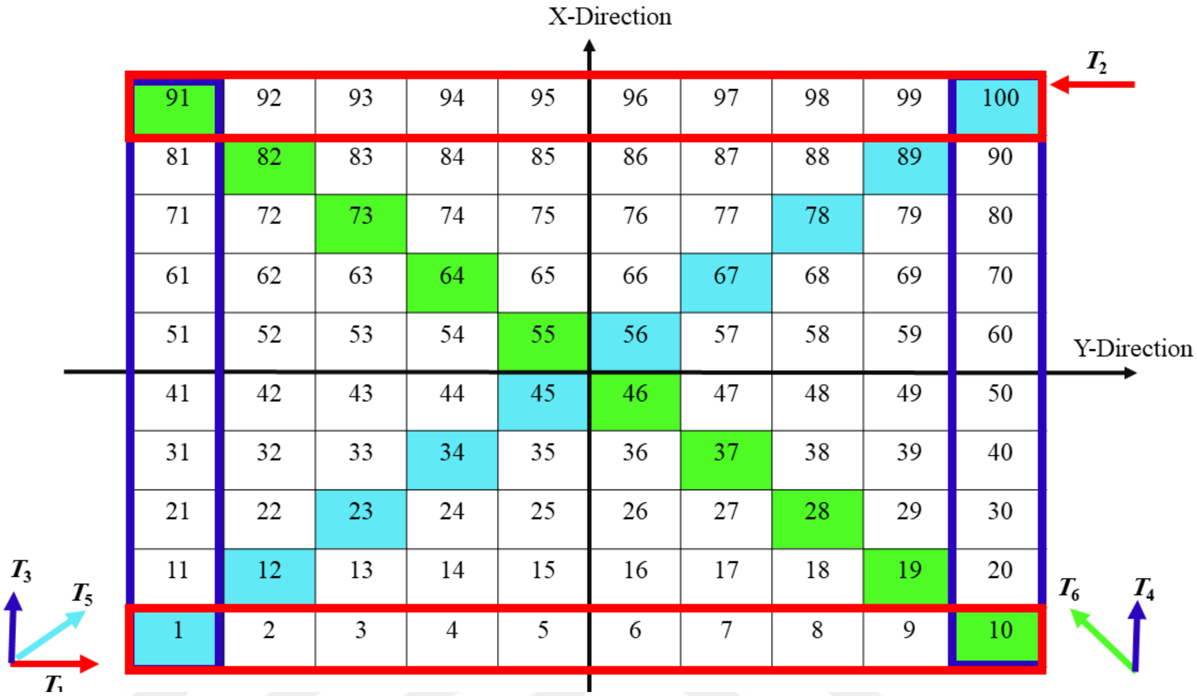

Figure 15: Up-side view of different trajectories considered in Indoor Scenario.

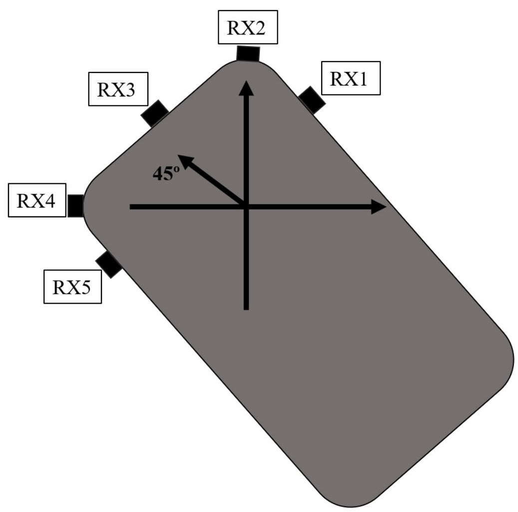

Figure 16: Orientation of RXs on the cell phone.

the model includes numerous relatively weaker random rays (R-rays), which account for the real-world environment with its random, smaller reflecting objects.

Fig. 17 illustrates the major steps of the CIR generation process including D-rays and R-rays based on the Q-D channel modeling developed within the MMW project in [72]. This

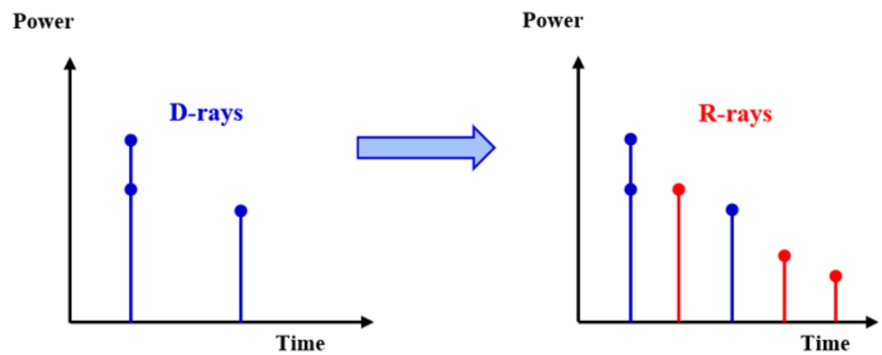

Figure 17: Basic steps in generating CIR.

model takes the advantages of both a geometry-based approach for the limited number of Multipath Components (MPCs) and a stochastic approach. Therefore, the realistic MMW channel models are made up of deterministic and random MPCs related to unpredictable factors and objects. In each scenario, the definition of D-rays, and R-rays are derived from the theoretical analysis as ray-tracing reconstruction and available experimental measurements. They represent the strong LOS rays, and some relatively weak random rays originating from the static surface's reflections. On the basis of this model, it is possible to conclude that CIR for indoor scenarios would include LOS rays (as D-rays) and MPCs including nth-order NLOS rays (as R-rays) reflected and diffracted from the floor, ceiling, walls, and objects as Fig. 18.

In Fig. 19, the path loss results are provided for RX1, RX2, and RX5 at 60 GHz and VLC. It is observed that the diagonal trajectories (i.e., T_5 and T_6) related to Scenarios 5 and 6 have the minimum path loss for RX1 and RX2 at the middle position of each trajectory in MMW. This trend is the same as VLC for RX2 T_3, T_5, and T_6 have lower path loss in comparison with the other trajectories. The path loss results of T_1, T_2, T_5, and T_6 significantly decrease over their initial positions on the path for given MMW RXs. Having passed the middle point of those trajectories, the path loss results of T_6 witness a dramatic increase. There are upward trends in the path loss results of T_1, T_2, and T_5 but not as much as T_6. The main factor behind this is the blockage of the cell phone with the human head,

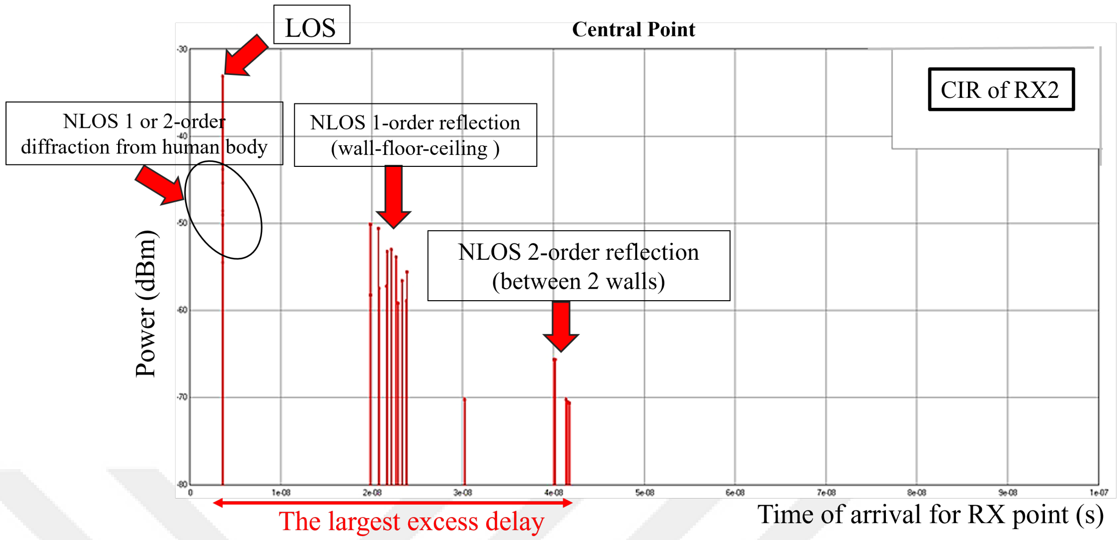

Figure 18: Analysing the CIR of RX2 for central point in Indoor scenario generated by Wireless Insite.

which appears after passing the middle position of T_6. For T_3 and T_4, there are only slight changes.

In VLC, all trajectories experience the sinusoidal signal behaviors by RX1 and RX2 which means that there are increasing and decreasing while the user is getting away or near the LEDs on the ceiling (See Fig. 14). For RX5, the minimum path loss results are related to T_1, T_6, and T_5, respectively. Because of the location of RX5 in the cell phone (See Fig. 16), most of the received rays are 1 or 2-order reflections from the floor. The path loss of RX5 fluctuates for the initial positions of T_1 and T_5 till the middle position levelled off. Then there is a steady growth in path loss results for the last positions of T_1. By contrast, the path loss results of T_3 and T_4 are flat and there is a significant difference between those amounts due to blockage of the receivers by the head of the human and sidewall over the T_3. The maximum results of the path loss are related to T_2 where RX5 is completely covered by the human body and sidewall throughout this path. It is worth noting that again the maximum difference between the first and last positions is related to T_6. In VLC more of trajectories experience fluctuation trends.

In Fig. 20, the impact of different frequencies on path loss results is presented for

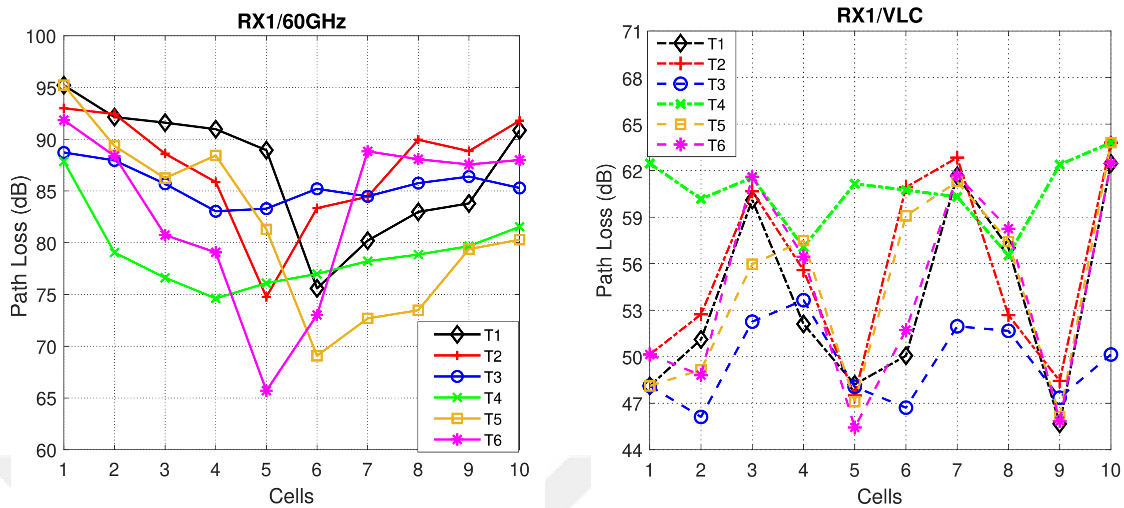

(a)

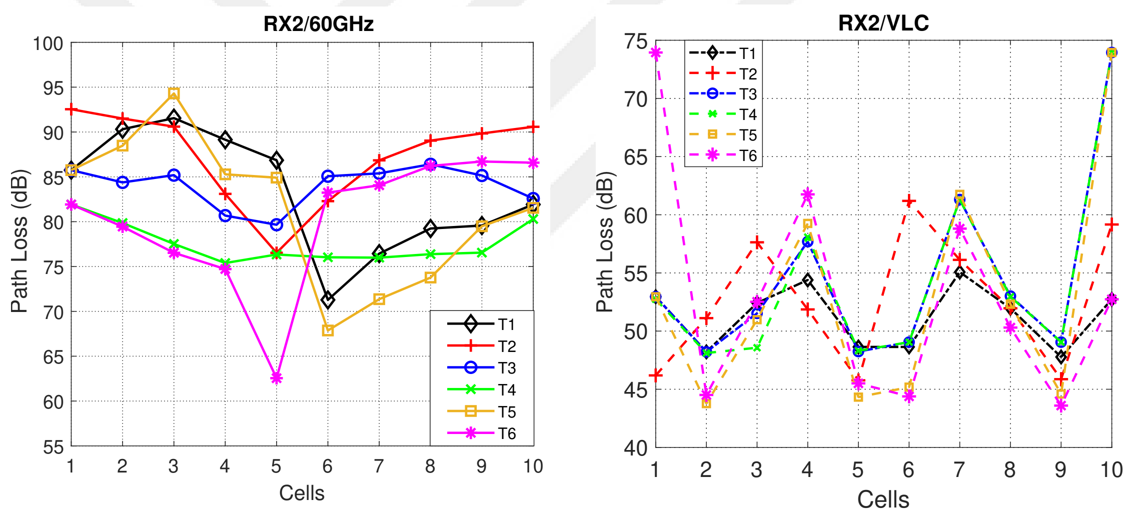

(b)

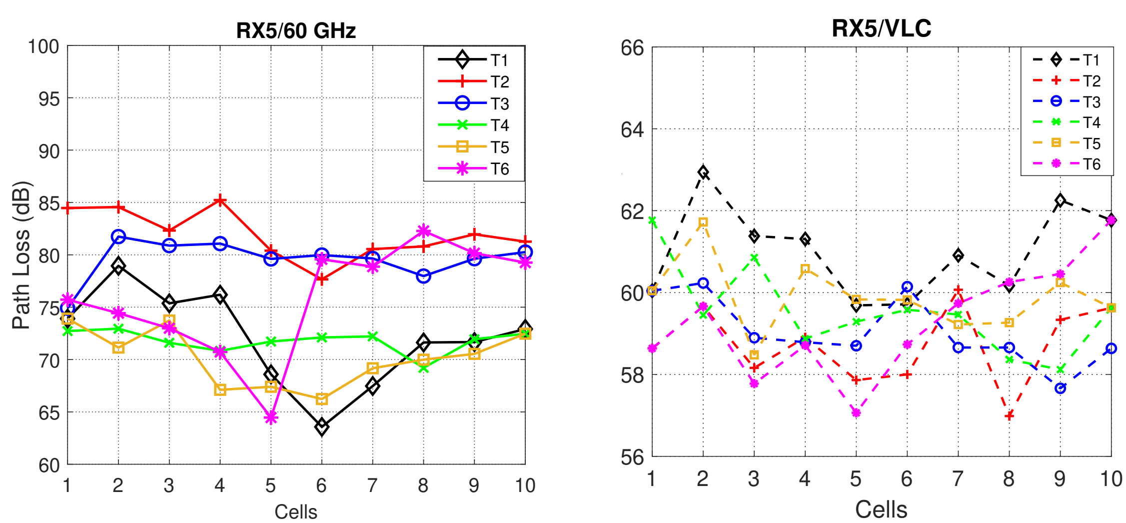

(c)

Figure 19: Effect of different trajectories on the path loss results for both MMW and VLC (Scenarios 1-6), considering (a) RX1, (b) RX2, and (c) RX5.

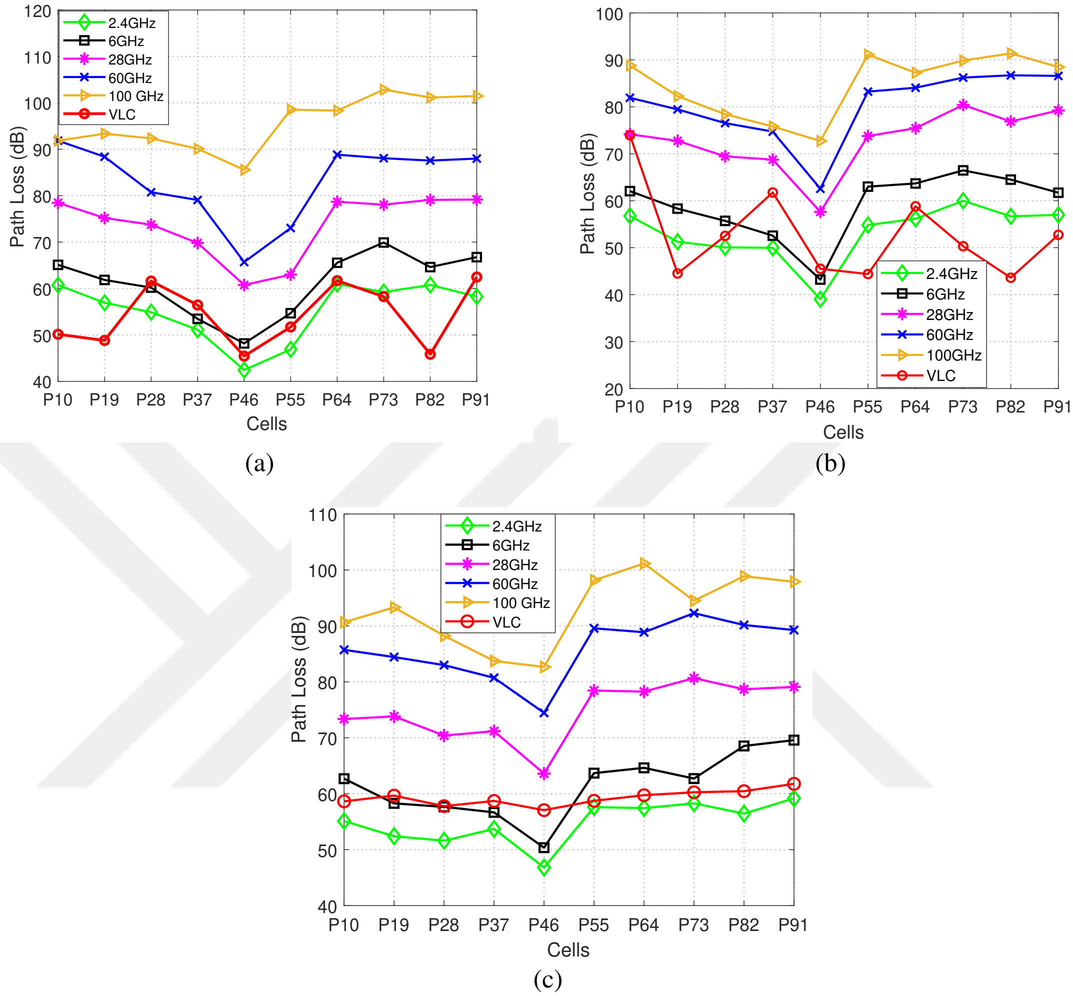

Figure 20: Effect of different frequencies on the path loss results considering T_6 (a) RX1, (b) RX2, and (c) RX5.

Scenario 6 (i.e., trajectory T_6), using omnidirectional antennas for RX1, RX2, and RX5. The results show that increasing frequency leads to an increase in path loss for all RXs. Interestingly, the results of VLC intersect with those of RF for all RXs. For instance, for RX2 (Fig. 20b), at certain positions such as P10, P37, and P64, the path loss of the 6 GHz band is lower than that of the VLC band, while at other positions such as P19, P55, and P92, the opposite is true. Notably, the 2.4 GHz, 6 GHz, and VLC bands yield the lowest path loss results compared to higher RF bands such as 28 GHz, 60 GHz, and 100 GHz.

Fig. 21 illustrates the effect of different antenna types on the path loss of Scenario 6 by considering 60 GHz. It is apparent from this figure that the path loss results for the

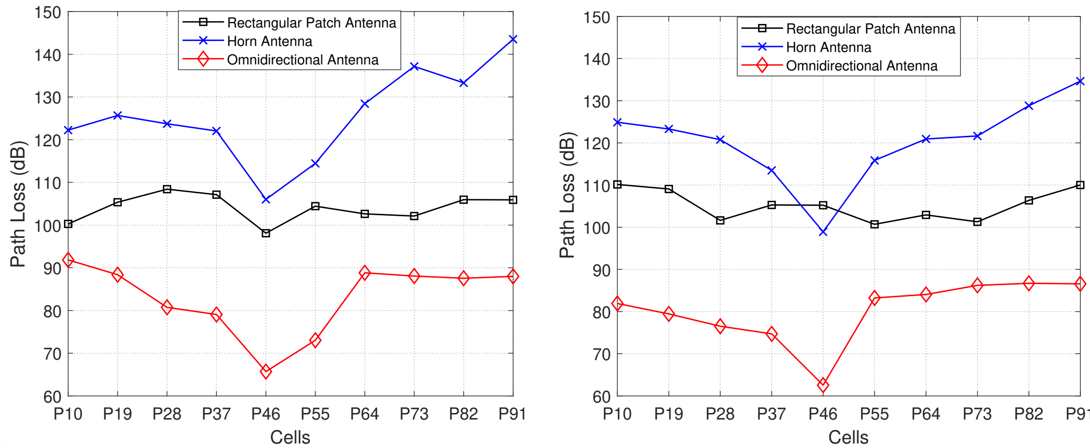

(a) (b)

Figure 21: Effect of antenna type on the path loss results considering 60 GHz and trajectory T_6 for (a) RX1 and (b) RX2.

omnidirectional antenna for RX1 are lower than the results for the rectangular patch and horn antennas. The factor behind this is the patterns of those antennas shown in Figure 13 (a-c). The patch antenna cannot get rays from all directions as much as an omnidirectional antenna. On the other side, its coverage is not as narrow as the horn antenna. It can be noted that the path loss of P46 with a horn antenna is less than one equipped with the patch antenna. The reason is that the main lope of the patch antenna is not as strong as the one in the horn antenna noting that both antennas have unit gain (See Fig. 13b and 13c). The side lopes of the patch antenna are stronger than the main lope. Therefore, the path loss result of RX1 in P46 has the minimum amount, however, RX2 cannot have a minimum result regarding its location in the cell phone and the pattern of the antenna (See Figures 13 and 16).

Fig. 22 presents the CIR of RX2 at P91 for different RX antennas including horn and omnidirectional antennas. At first sight, the LOS components in exploiting omnidirectional antenna increases by nearly 40 dBm. The main factor behind this is the location of the RX2 antenna on the cellphone and the position P91 leading to coverage of the cellphone by the head of the human and the corner walls of the room (See Fig. 14 - 16). Also, the direction of the main lobe in RX2 towards the ceiling as its pattern in Fig. 13 indicates. However,

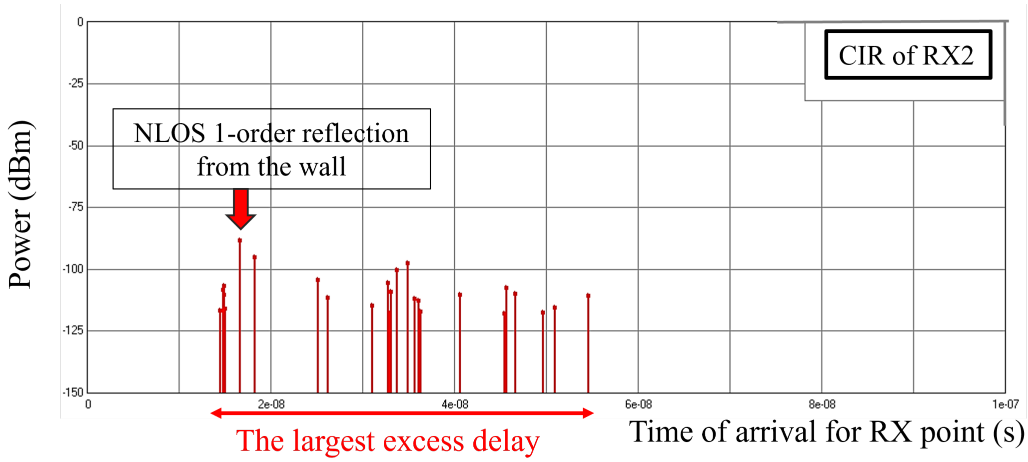

(a)

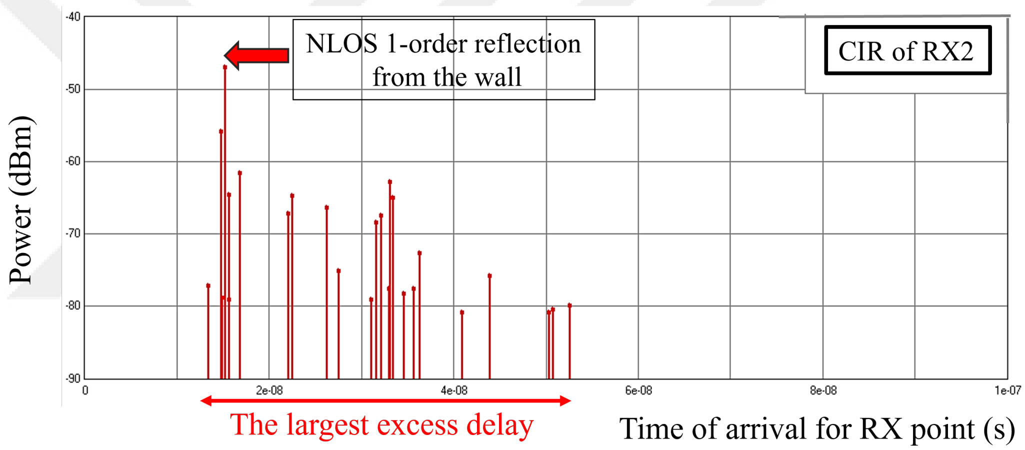

(b)

Figure 22: Analysing CIR of P91 related to RX2 at P91 using (a) Horn antenna, and (b) Omnidirectional

the omnidirectional antenna enabled in RX2 can receive all rays in different directions with the same antenna gain.

In Fig. 23, the path loss results are presented for all RXs assuming omnidirectional antennas for Scenario 3. Results illustrate that RX1, RX2, and RX3 have less path loss in all positions belonging to P41. The reason is that the human head covers the cell phone in his hand throughout this path, but the location of RX2 can help to get the power with less path loss by receiving the reflected signals from the ceiling. For VLC RX1-RX3 experiences less path loss than RX4 and RX5. Due to utilizing 9 LEDs on the ceiling, there is no

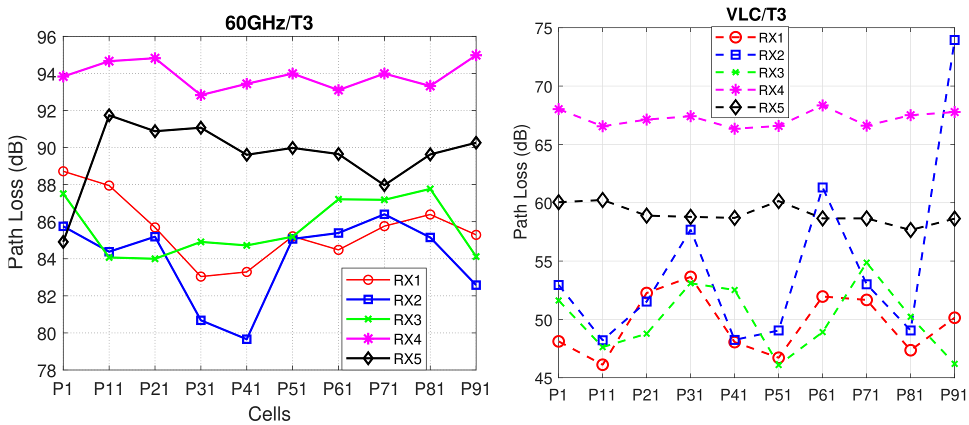

(a) (b)

Figure 23: Effect of receiver locations on the path loss results of MMW and VLC considering trajectory T_3.

minimum point, and the behavior of the path loss follows a sinusoidal pattern.

In the following, we investigate the received power levels for all scenarios and frequency bands under consideration. We consider the CDF of received powers as seen by the individual receivers (i.e., RXs). This presents the probability that received power will take less than or equal a specific value, which is given by

$$F_X(x) = \Pr[X \leq x]. \tag{2.1}$$

As shown in Fig. 24, the worst case occurs for RX5 because it is located at the bottom of the cell phone and faces down (see Fig. 16). Therefore, most of the received rays at RX5 are mainly due to the first reflection from the floor or higher order reflections from the walls and ground (i.e., no LOS reception). In contrast, RX2 has the highest received power (best case) due to its ability to get LOS rays in most positions. Because it is located on the top of the cell phone and faces toward the ceiling, where TXs are located. Results also illustrate that RX1 and RX3 have lower path loss in comparison to RX4 and RX5. Because the human head covers a part of the cell phone throughout the path, which contains RX4 and/or RX5 depending on the location. RX1 and RX3, however, experience lower path loss since they are only partially covered. In the VLC case, RX1 and RX3 can even get a LOS signal from different luminaries based on user location.

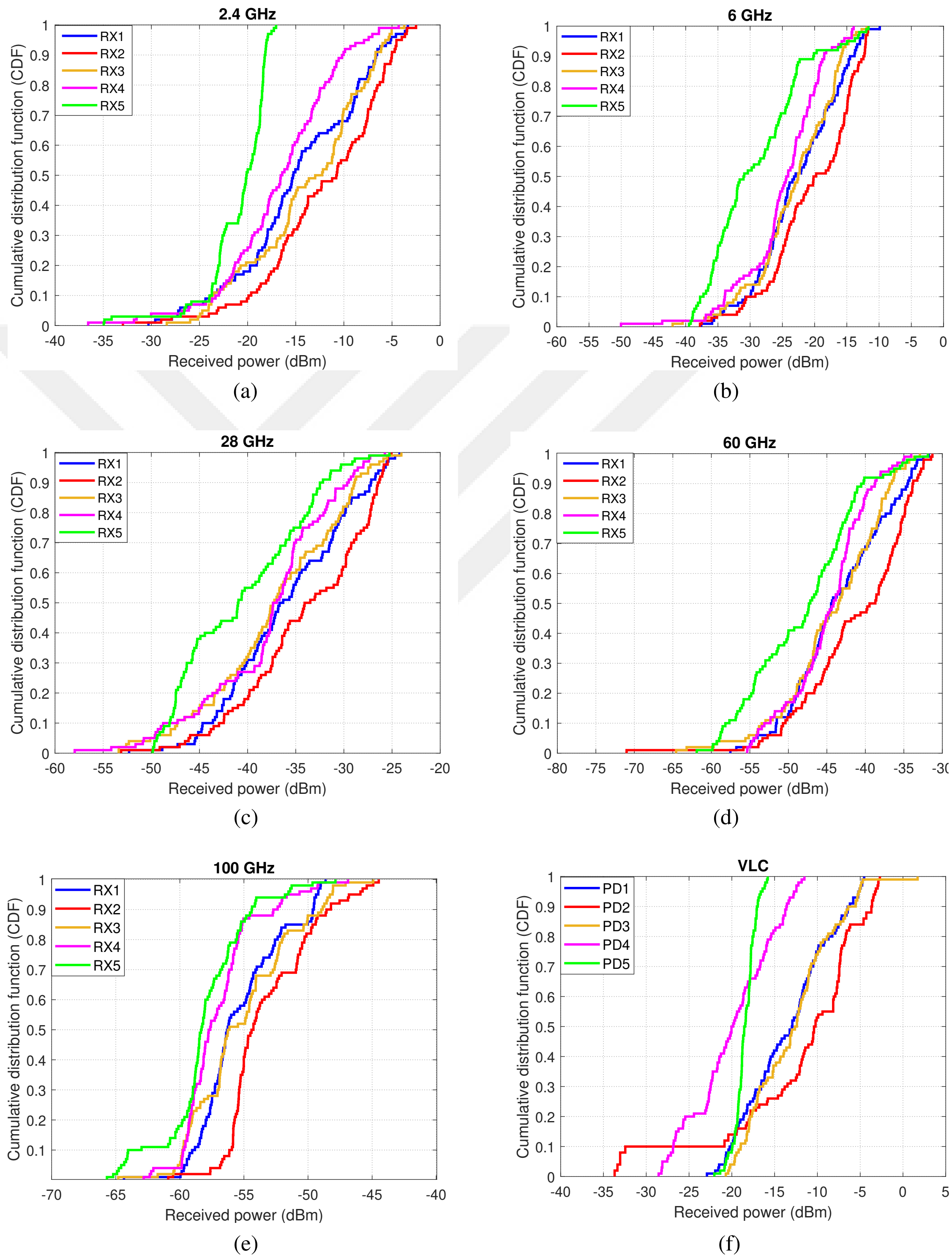

Figure 24: CDF of received power as seen by the individual RXs and Photo Detectors (PDs) for different RF (a-e) and VLC (f) frequencies.

Table 7: Gaussian coefficients in the CDF functions of received powers for 2.4 GHz.

	$F_{1X}(x) = a_1 \exp\left(-((x-b_1)/c_1)^2\right)$		
2.4 GHz	a_1	b_1	c_1
RX1	0.96	2.56	14.66
RX2	1.22	4.35	16.35
RX3	1.16	1.73	16.13
RX4	0.98	4.83	11.54
RX5	1.58	3.32	12.75

Table 8: Gaussian coefficients in the CDF functions of received powers for 6 GHz.

	$F_{1X}(x) = a_1 \exp\left(-((x-b_1)/c_1)^2\right)$		
6.0 GHz	a_1	b_1	c_1
RX1	0.96	10.55	14.44
RX2	1.07	10.60	21.37
RX3	1.02	10.41	14.24
RX4	0.98	11.75	11.47
RX5	0.99	14.18	16.10

Furthermore, we propose closed-form expressions for the CDFs of indoor channels for all scenarios and receivers under consideration. We use non-linear curve fitting in the MATLAB toolbox to determine the CDF behavior of the channel path losses. At lower frequencies (i.e., 2.4 GHz, 6 GHz, and 28 GHz), the CDF of the received power is fitted with a 1-term Gaussian function. For higher frequency bands (i.e., 60 GHz, 100 GHz, and VLC), the CDF of the received power is fitted with a 2-term Gaussian function. These are given, respectively, by

$$F_{1X}(x) = a_1 \exp((-(x-b_1)/c_1)^2), \tag{2.2}$$

$$F_{2X}(x) = a_1 \exp((-(x-b_1)/c_1)^2) + a_2 \exp((-(x-b_2)/c_2)^2), \tag{2.3}$$

where, x denotes the received power (in dBm), a_1, a_2, b_1, b_2, c_1, and c_2 are coefficients of Gaussian functions with 95% confidence bounds, and adjusted R-squares of 99% provided in Table 7 - Table 12.

Fig. 25 shows the CIR of a critical position (i.e., P91 as the corner point in our Indoor scenario, See Fig. 14) where the cell phone is covered by the human head and the

Table 9: Gaussian coefficients in the CDF functions of received powers for 28 GHz.

	$F_{1X}(x) = a_1 \exp\left(-((x-b_1)/c_1)^2\right)$		
28 GHz	a_1	b_1	c_1
RX1	0.9569	24.09	14.57
RX2	1.441	22.64	19.71
RX3	0.983	23.8	15.75
RX4	0.980	26.71	12.61
RX5	0.97	27.45	15.96

Table 10: Gaussian coefficients in the CDF functions of received powers for 60 GHz.

	$F_{2X}(x) = a_1 \exp(-((x-b_1)/c_1)^2) + a_2 \exp(-((x-b_2)/c_2)^2)$					
60 GHz	a_1	b_1	c_1	a_2	b_2	c_2
RX1	0.97	29.9	3.82	0.45	31.95	10.51
RX2	0.97	37.67	3.48	1.01	30.77	12.97
RX3	0.83	39.71	3.98	1.00	34.61	11.78
RX4	1.65	31.64	4.02	1.53	29.82	16.09
RX5	0.96	32.89	2.31	0.98	33.81	16.66

Table 11: Gaussian coefficients in the CDF functions of received powers for 100 GHz.

	$F_{2X}(x) = a_1 \exp(-((x-b_1)/c_1)^2) + a_2 \exp(-((x-b_2)/c_2)^2)$					
100GHz	a_1	b_1	c_1	a_2	b_2	c_2
RX1	0.939	49.12	5.703	0.313	55.29	2.821
RX2	1.016	46.83	6.358	0.296	53.64	1.822
RX3	0.996	45.63	7.43	0.373	54.30	2.708
RX4	1.011	48.07	6.193	0.559	55.34	3.621
RX5	1.028	49.36	7.93	0.308	56.16	1.669

Table 12: Gaussian coefficients in the CDF functions of received powers for VLC.

	$F_{2X}(x) = a_1 \exp(-((x-b_1)/c_1)^2) + a_2 \exp(-((x-b_2)/c_2)^2)$					
VLC	a_1	b_1	c_1	a_2	b_2	c_2
RX1	0.096	13.63	3.38	0.89	14.37	8.71
RX2	0.12	16.61	2.96	0.668	18.93	7.22
RX3	0.300	15.41	3.24	0.877	16.94	9.16
RX4	0.255	10.58	2.98	0.807	13.61	9.10
RX5	0.099	16.23	2.43	0.80	18.38	9.84

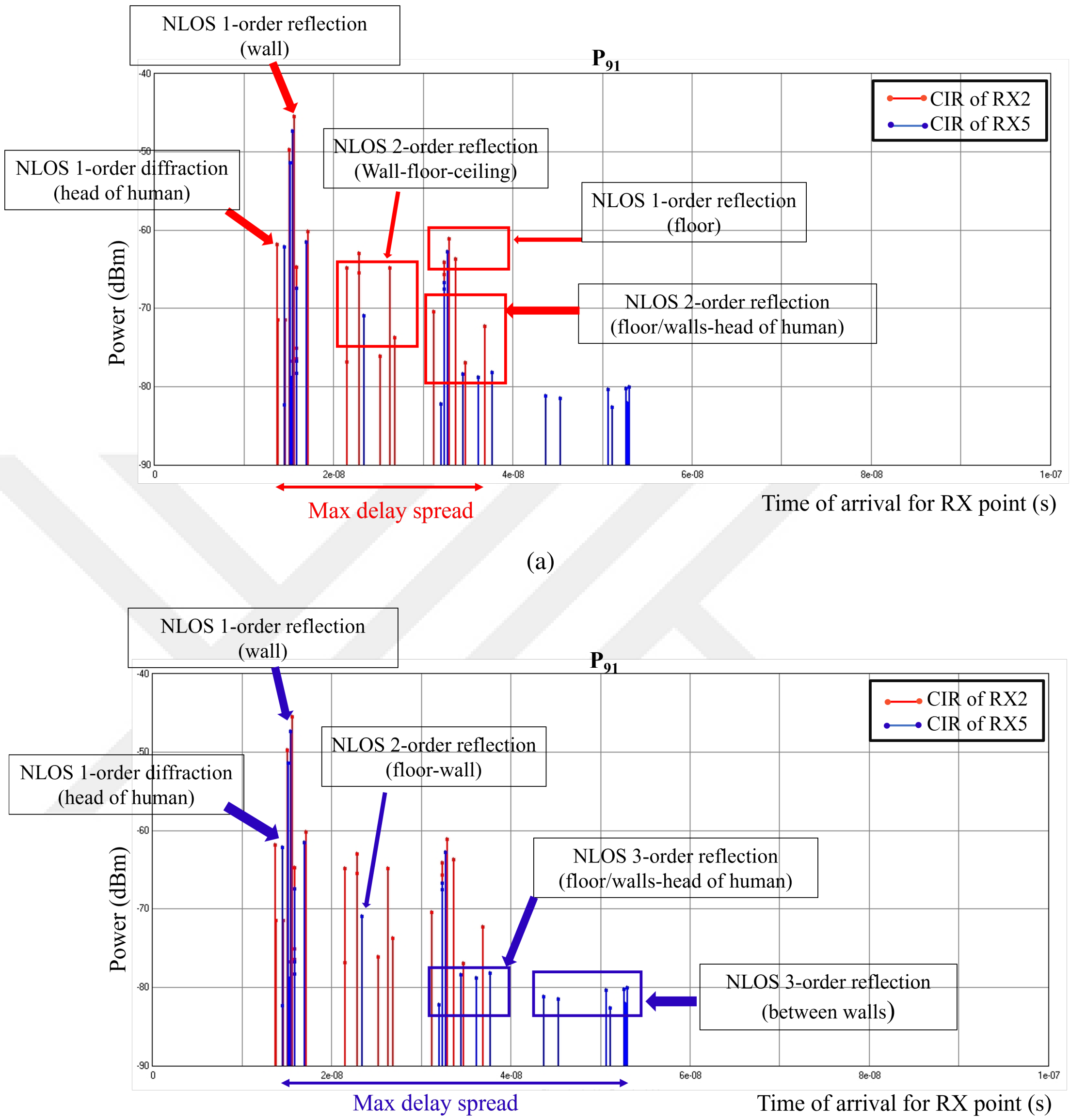

(a)

(b)

Figure 25: Analysing CIRs of P91 related to (a) RX2, and (b) RX5

wall. This position is a good sample for using raytracer tools in studying the indoor channel model due to the lack of an accurate analytical model at all locations of a room. It is apparent comparing Figs. 18 and 25 that the related CIR to RX2 at the central point includes the LOS as the first arrived component with the highest value displayed. Unlike that, the first arrived components of CIRs of RX2 and RX5 for P91 are related to 1-order diffraction rays (as NLOS) from the head of the human. The factor behind the NLOS rays

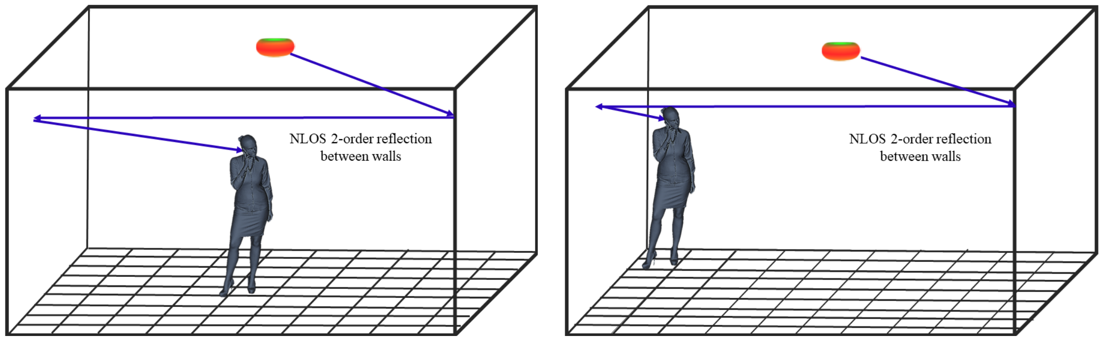

(a) (b)

Figure 26: Multiple rays related to the last components in CIRs of RX2 (a) Central point, and (b) P91.

in P91 is hidden receivers covered by the head of the human and walls in the corner. It is observed that the components with the highest power in P91 emerged by 1-order NLOS reflection from the wall near the human. Comparing the CIR of RX2 and RX5 P91, the impulse response of RX5 includes the 3-order NLOS components arrived from reflections and diffraction between surrounding walls and the ground-wall-head of the human. All reflection and diffraction rays with different orders are noted in Figs. 25a and 25b. There is also a remarkable point that can be distinguished by these figures regarding the delayed spread of CIRs. Although the human at the central point is closer to the transmitter (See Fig. 26a) than P91 (See Fig. 26b), 2-order NLOS reflection rays between surrounding walls passed more distance compared with P91 till arrived at RX2 shown in Fig. 26b. Therefore the delay spread of the CIR at the central point (Fig. 18) received by RX2 is more than case P91 (Fig. 25a). Moreover, the delay spread of CIR of RX5 is larger than RX2 at the same position (i.e. P91) due to having higher-order reflection rays (See Fig. 25a and 25b).

CHAPTER III

CHANNEL MODELING AND CHARACTERIZATION FOR VEHICULAR COMMUNICATION

3.1 Introduction

ITSs provide road traffic information and local awareness to ensure safety for drivers through functionalities such as cruise control, parking assistance, and collision avoidance. V2V communication is an underlying key technology to realize ITSs [73]. For example, Toyota has become the first universal automaker to deliver connected vehicles by equipping them with IEEE 802.11p-based DSRC [74, 75]. To improve data rates and latency of DSRC, the Cellular Vehicular Network (C-V2X) standard was introduced as part of 5G [76] with various ongoing pilot deployments worldwide [77, 78].

It is envisioned that 6G will leverage spectra going beyond the millimeter wave including optical bands, in particular, visible light [79, 80]. MMW communication and VLC are both strong candidates for V2V communication. Table 13 shows some advantages of both MMW and VLC over the DSRC solutions like ITS-G5/DSRC and IEEE 802.11p/DSRC [81–83].

While the MMW and visible light are different in nature, they exhibit some similarities since they both operate at higher frequencies compared to sub-6 GHz systems. Since earlier works discussed above focus on an individual technology, they do not present a one-to-one comparison of vehicular MMW and VLC channels[1]. To the best of our knowledge, the only prior work that attempts to make such a comparison is [85] where path loss comparisons are made based on an experimental study. However, this work is limited to a simple

[1] In the context of indoor communications, a comparative comparison of MMW and VLC channels was presented in [84].

Table 13: Radio and Visible Light solutions for vehicular communication.

Type	VLC	MMW	IEEE 802.11p/DSRC ITS-G5/DSRC
Communication Mode	Point to Point (LOS or Diffuse)	Point to Multipoint or Broadcasting	Point to Multipoint or Broadcasting
Frequency Band	400-790 THz	28, 38, 60GHz 70-80 GHz (E-band)	5.85-5.92 GHz
Latency	5ms	10ms	50ms
Channel Bandwidth	No limited	199 MHz-2.16 GHz	10 MHz
Data Rate	Up to 400 Mb/s	Up to 7 Gb/s	Up tp 27 Mb/s
License	Unlicenced	Licensed	Licensed
Weather Condition	Sensitive	Sensitive	Robust
Cost	Low	Low	High
Mobility Support	100 m/h	100 km/h	130 km/h

V2V scenario where two cars communicate with each other in an indoor garage. In this chapter, we aim to provide a one-to-one comparison between vehicular VLC and MMW channels with an emphasis on the effect of vehicular topology. For this purpose, we utilize ray tracing simulations. This enables the consideration of three-dimensional modeling of the propagation environment and allows the study of various system parameters and road conditions in both LOS and NLOS configurations. For this purpose, we use Remcom's Wireless Insite [35] ray tracing software tool for MMW and compare our results with VLC channel modeling. Under the same settings, we present the received signal strengths for both systems and investigate the channel characteristics for communication between two vehicles in the same lane as well as in different lanes with a lateral shift. We also analyze the impact of low, medium, and high density of neighbor vehicles as well as partial and complete LOS blockage.

The rest of this chapter is organized as follows: In Section 3.2, we describe the vehicular scenarios under consideration. In Section 3.3, we present the channel modeling methodology for MMW and VLC systems. In Section 3.4, we present simulation results and discussions on the comparison of the two systems under consideration.

3.2 Vehicular Scenarios

We consider a V2V communication system on a three-lane road. The three-lane roads are commonly used in urban areas and chosen in our study to give us the flexibility to investigate the effect of different lateral shift values as well as different vehicle density cases. Two-lane roads are typical choice in rural areas and can be considered as a sub-set of three-lane road under consideration. We consider four V2V scenarios illustrated in Fig. 27 - Fig. 30 and detailed below:

- **Scenario 1**: In this scenario, we consider two vehicles following each other in the same lane with perfect alignment as shown in Fig. 27.

- **Scenario 2**: In this scenario, we consider two sub-scenarios to investigate the impact of lateral shift d_h between two vehicles: **2.a**. Two vehicles follow each other in the same lane but there is a lateral shift between them as shown in Fig. 28a. **2.b.** Two vehicles follow each other in different lanes with a lateral shift d_h as shown in Fig. 28b where the source vehicle communicates with a vehicle traveling in the 3^{rd} lane.

- **Scenario 3**: In this scenario, we investigate the effect of neighbor vehicles. An effective way to estimate traffic density is the calculation of the occupied road surface by vehicles. Specifically, the Percentage Vehicle Occupancy (PVO) of the road segment can be defined as [86]

$$PVO = \frac{\text{No. of } VOB}{\text{No. of } BOI} \times 100, \tag{3.1}$$

  where VOB is the Vehicle - Occupied Block and BOI is the Block of Interest (which can be selected as the same width of each lane). Table 14 provides the classification of traffic density based on PVO. In our work, we consider three different sub-scenarios where the PVO values are calculated respectively as 20%, 60%, and 80% which correspond to low, medium, and high density: **3.a. (Low density)** Two vehicles follow each other in the middle lane and there is one neighbor vehicle in each of the side lanes as shown in Fig. 29a. **3.b. (Medium density)** Two vehicles

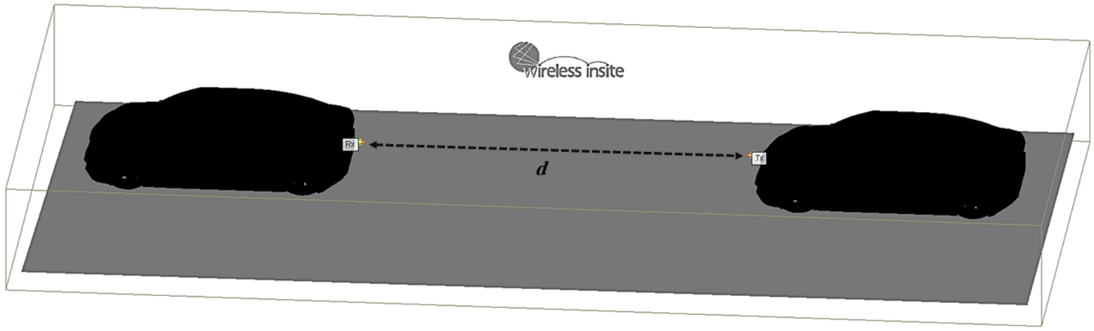

Figure 27: Two vehicles following each other in the same lane with perfect alignment (Scenario 1).

Table 14: Classification of traffic density based on *PVO*

Traffic Density	% Range
Low	$PVO < 40\%$
Medium	$40\% \leq PVO \leq 65\%$
High	$PVO > 65\%$

follow each other in the middle lane and there are 2-3 neighbor vehicles in each of the side lanes as shown in Fig. 29b. **3.c. (High density)** This scenario is similar to the previous one but there are additional neighbor vehicles in the middle lane which partially blocks the LOS signal as shown in Fig. 29c.

- **Scenario 4**: In this scenario, we investigate the effect of partial and full LOS blockage. Specifically, we consider two different sub-scenarios: **4.a**. Two vehicles follow each other in the middle lane (see Fig. 30a) where the middle car blocks LOS transmission. **4.b**. Two vehicles follow each other in the middle lane (Fig. 30b) where the middle car results in partial LOS blockage.

3.3 Channel Modeling Methodology

As illustrated in Fig. 31, the source vehicle is equipped with a single horn antenna, denoted by TX, for MMW transmission. For the VLC case, the two headlights of the vehicle are the transmitters which are denoted by TX1 and TX2. On the other side, the destination vehicle is equipped with a single receiver denoted by RX, located in the middle of the car's

(a)

(b)

Figure 28: Effect of lateral shift (Scenario 2): (a) Lateral shift in the same lane, (b) Lateral shift in different lanes.

back, for MMW reception. For the VLC case, we deploy two receivers, denoted by RX1 and RX2, and they are located under the car taillights. Out of these two RXs, the one with the highest received power is selected. We use Remcom's Wireless Insite® [35] software tool for MMW and compare our results with VLC channel modeling. This tool builds upon advanced non-sequential ray tracing features and makes possible integration of the realistic source radiation patterns and wavelength-dependent reflectance of surface coating for each material for a precise characterization of the signal interaction with the environment.

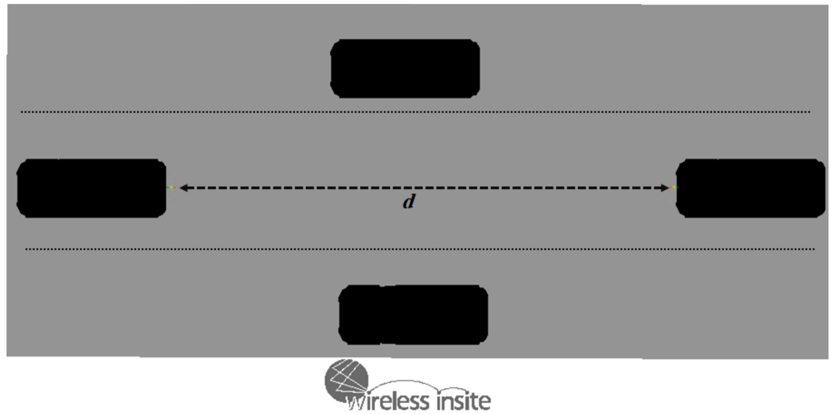

(a)

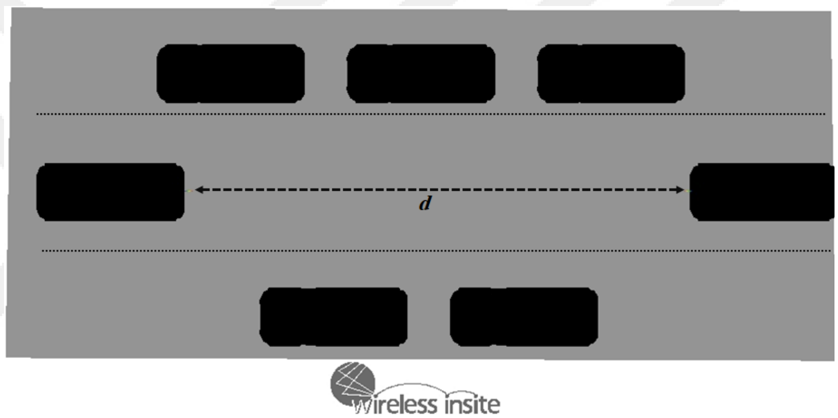

(b)

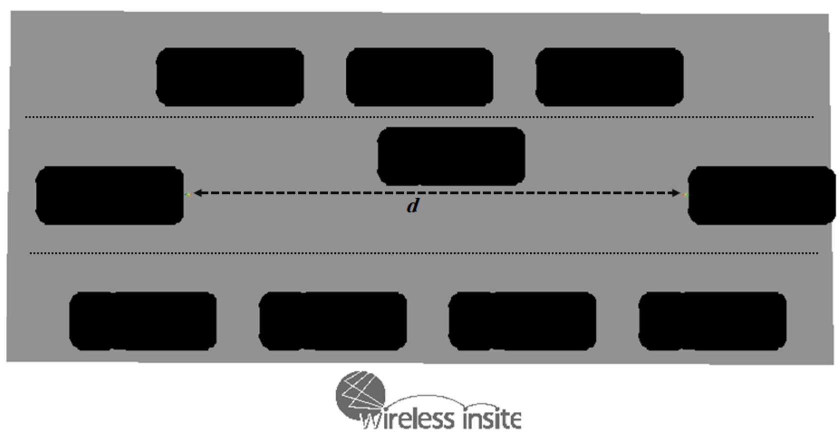

(c)

Figure 29: Effect of vehicle density (Sky view of Scenario 3): (a) Low density, (b) Medium density, (c) High density.

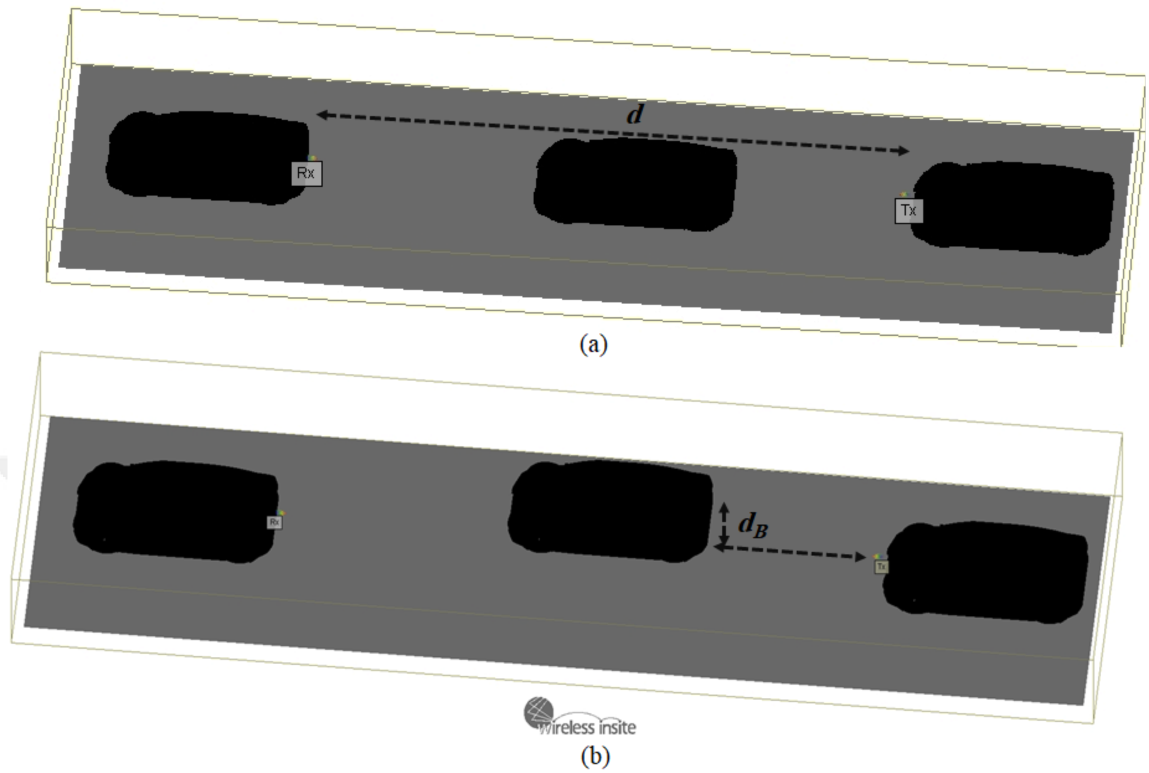

Figure 30: Effect of LOS blockage (a) Full blockage, (b) Partial blockage.

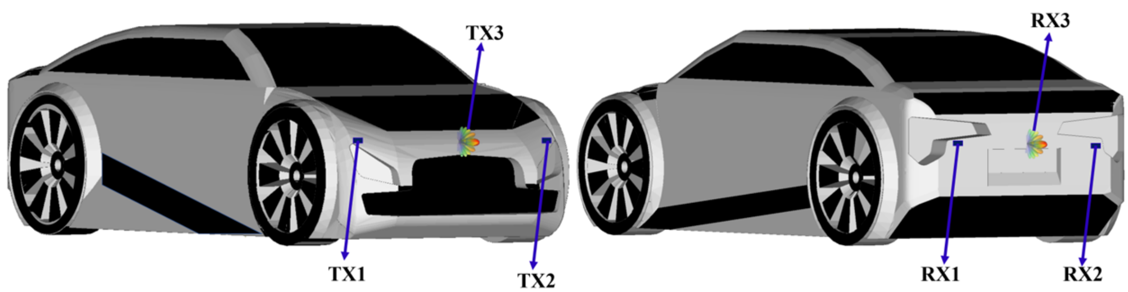

Figure 31: CAD model of vehicles and the locations of transmitters and receivers.

3.3.1 MMW Channel Modelling

In the following, we explain the main steps in the simulation study of MMW vehicular communication using Wireless Insite.

First, we build a three-dimensional model of the vehicular environment in the software where the CAD models of vehicles are imported. Then, we define the transmitter and receiver specifications such including antenna type, radiation pattern, orientation, etc. Additional inputs related to antenna type include maximum gain, polarization, aperture/feed width and height, and feed-aperture length. For example, in our simulations, we use the horn antennas which are preferred in vehicular scenarios due to their attractive merits such as directional performance, high gain, wide bandwidth, and peak power handling capability. When the radio waves encounter objects (i.e., road surface, other vehicles, etc), they produce losses depending on the electrical features of the surface materials. In Wireless Insite®to characterize these interactions, we define the frequency dependence of surface materials in terms of permittivity, conductivity, and thickness [67]. For example, the reflections of the road surface are characterized as a mix of specular and diffuse in our study while the reflections on the vehicles with glossy paint are modeled as specular [87]. To model the scattering in Wireless Insite, the X3D propagation model is used where the reflection type in materials can be determined by the "scatter fraction" parameter. This parameter changes between 0 and 1 such that zero denotes the purely specular reflections and unity indicates the purely diffuse case.

Wireless Insite®uses the SBR method [69] to obtain the channel impulse response. By default, the rays are launched with 0.25^o angular spacing. These are traced back to the receiver. The software accounts for the effects of reflections, and diffraction based on the geometrical optics and uniform theory of diffraction for each multiple components. As outputs, Wireless Insite can generate the received power, the path loss, and CIR automatically by selecting those items as intended results in the output window [35]. It is worth noting that generating CIR, PL, and P_r in Wireless Insite follows the equations in Sections 1.5.

3.4 Results and Discussions

In this section, we present simulation results for VLC and MMW channels of vehicular scenarios under consideration. Table 15 and Fig. 32 provide the simulation and imported CAD parameters. As illustrated in Fig. 33, the MMW system uses a horn antenna (see

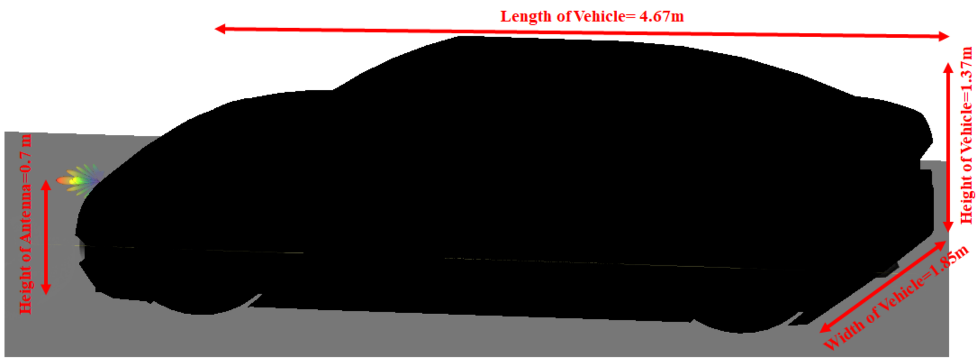

Figure 32: Parameters of Vehicle CADs.

Appendix A for further details on antenna specifications) placed at the same height as headlights.

To have a fair comparison between the two systems, attention should be paid to optical versus electrical power. For the VLC system, the transmit electrical power (P_t) is related to the transmit optical power ($P_{t,\text{opt}}$) by the electrical-to-optical conversion ratio (η), i.e., $P_{t,\text{opt}} = \eta P_t$. This is the power that drives the LED in VLC system. In our analysis, η = 0.5 W/A [88], and $\Re$ = 0.5 A/W [89], are given and the transmit power is further divided by 2 (i.e., two headlights) to have a fair comparison with the MMW system, which utilizes a single transmit antenna.

Consider the CIR in Fig. 34 plotted by using Wireless Insite reconstruction of the vehicular scenario 1. This CIR is very similar to the one proposed in [72] as IEEE 802.11ay channel modeling. The conclusion as a result of these observations is that realistic MMW channel models consist of Deterministic (D-rays) and Random (R-rays) MPCs defined by the scenarios and unpredictable factors, respectively. The first D-ray components are the direct path (LOS) and some ground reflections (1-order reflection) dominating other path components as shown in Fig. 35a. Then higher-order reflections between two cars and car-road (See Fig. 35b and c) are added as R-rays with different powers and delays to construct the CIR. It is worth noting that 2-order reflected components between car and road as Fig. 35c have low delay and power, so they disappear sooner comparing 2-order

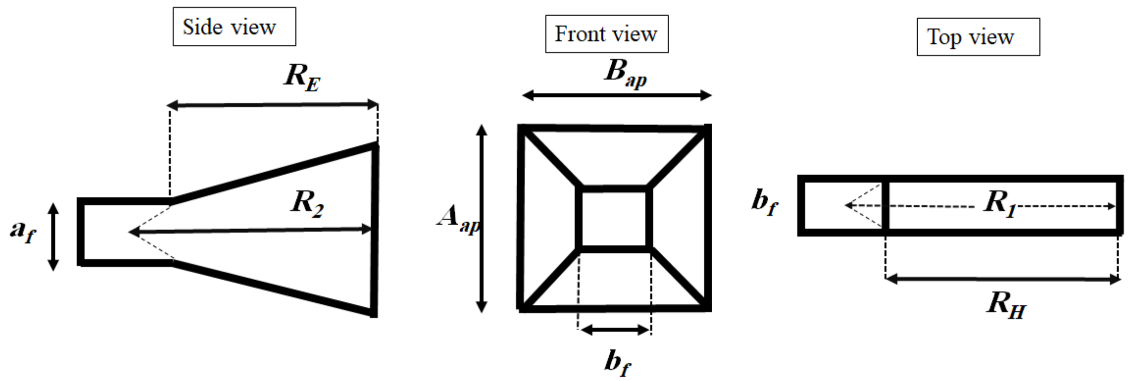

(a)

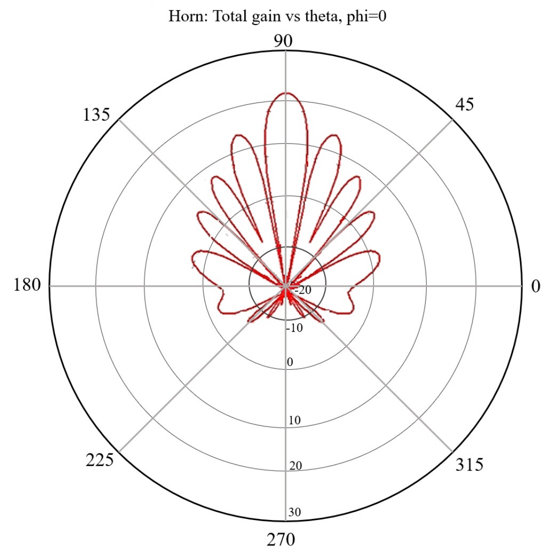

(b)

Figure 33: Horn antenna specifications (a) Physical dimensions (b) Radiation pattern of Horn antenna.

reflections between two cars.

In Fig. 36, we present the received power versus distance for Scenario 1, assuming different values of transmit power (P_t). In particular, we assume P_t = 1 mW, 0.0316 W, 1 W, 5 W, 10 W, 20 W, and 40 W. It is observed that, in comparison to MMW, the VLC channel exhibits a faster-decaying behavior. For example, at a transmit power of P_t = 1 mW, the difference in received powers reaches up to 40 dB. This is a result of the quadratic relationship between the received and transmitted electrical powers in VLC. Therefore, VLC is better suited for relatively short-distance communication while MMW might be

Table 15: Simulation Parameters

Road Size	100 m × 11.25 m
Road surface (Asphalt)	ε_r=5.72 $\sigma_r = 5.10^{-4}$
Scattering	Mixed diffuse and specular
No of Lanes **Width of lane**	3 3.75 m
Height of Vehicle **Length of Vehicle** **Width of Vehicle** **Height of antennas** **Material of Vehicle**	1.37 m 4.67 m 1.85 m 0.7 m Metal
Transmit Power	1mW, 0.0316, 1, 5, 10, 20, 40 W
Area of antenna	1 cm^2
Gain of antenna	23 dBi
Gain of optical concentrator	1
Power spectral density of noise	10^{-21} A^2/Hz
System bandwidth	20 MHz

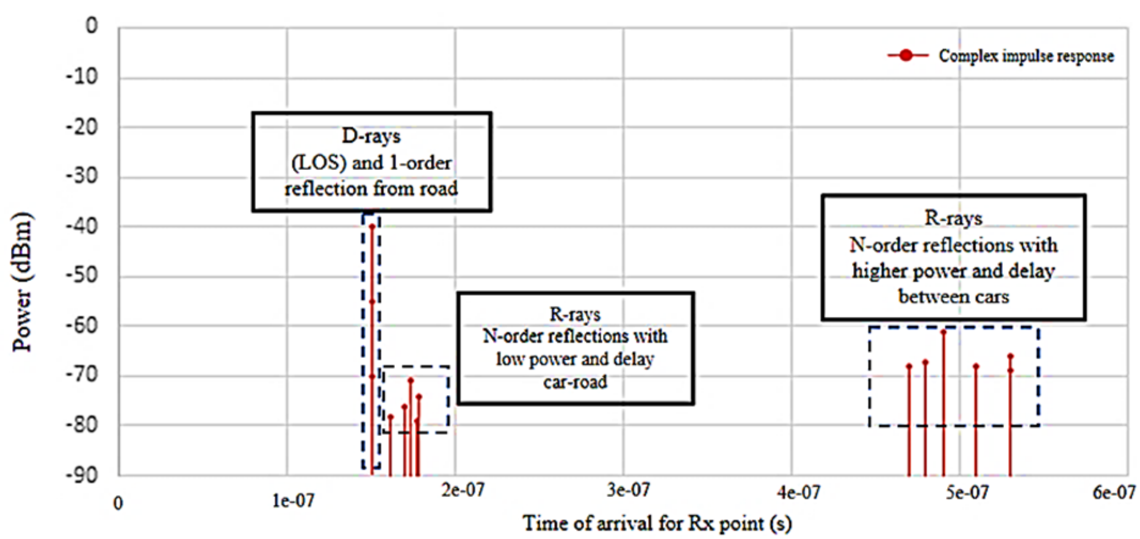

Figure 34: Analysing the CIR of V2V Sceanario

better for larger distances.

In Fig. 37, the CIR of scenario 1 for different TX-RX distances is presented by Wireless Insite including the powers of MPCs in terms of ToA. LOS ray is the first and largest

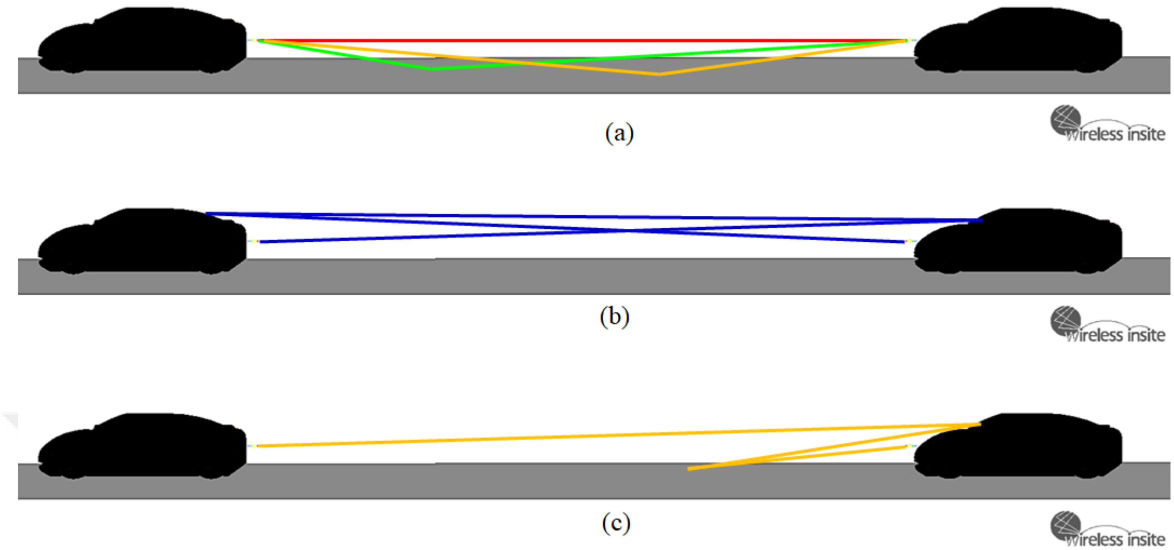

Figure 35: Propagation of MPCs for scenario 1 (a) LOS and 1-order reflections from the road as D-rays, (b) 2-order reflections between cars as R-rays, (c) 2-order reflections between car and road as R-rays.

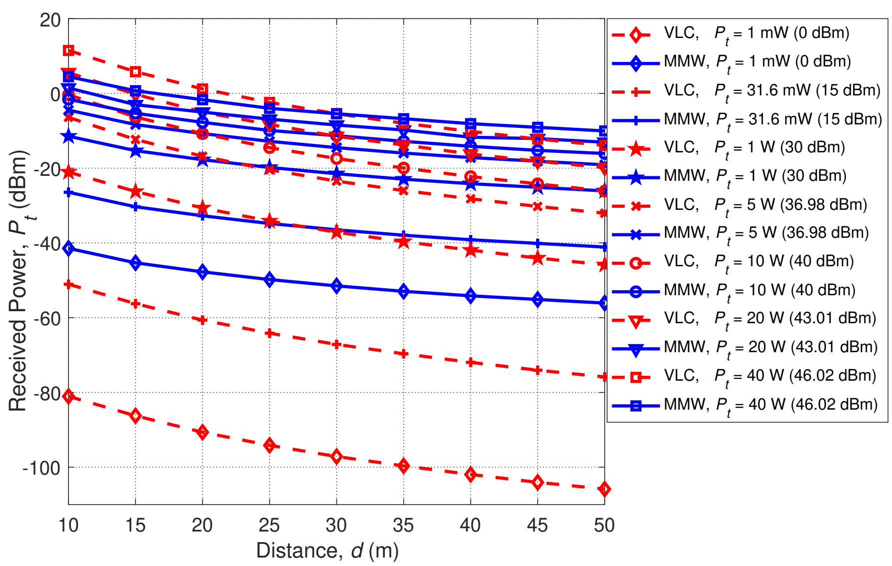

Figure 36: The received power versus distance in Scenario 1.

component, however 1-order NLOS reflections from the road are related to the first components with less power. By increasing the Tx-RX distance not only the LOS ray is transfered

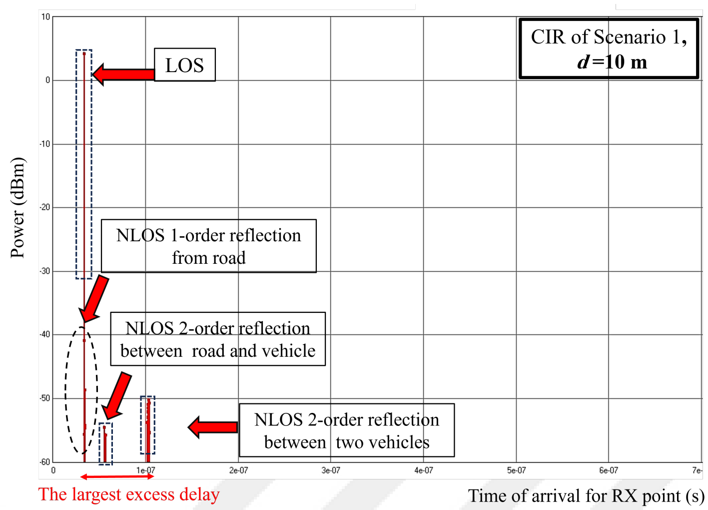

(a)

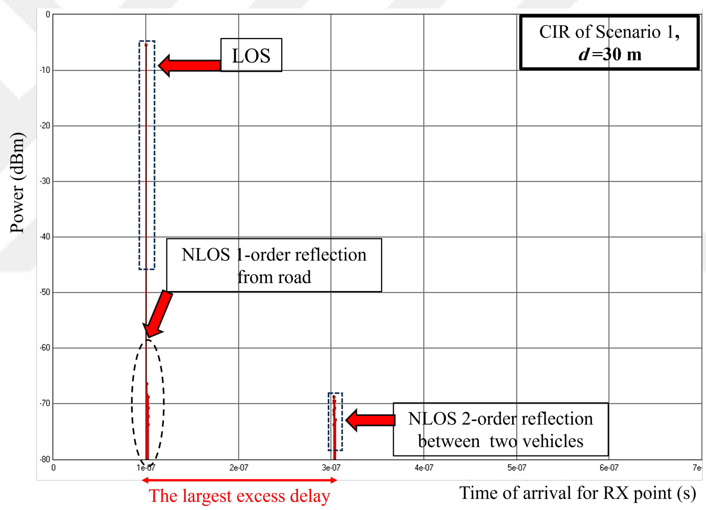

(b)

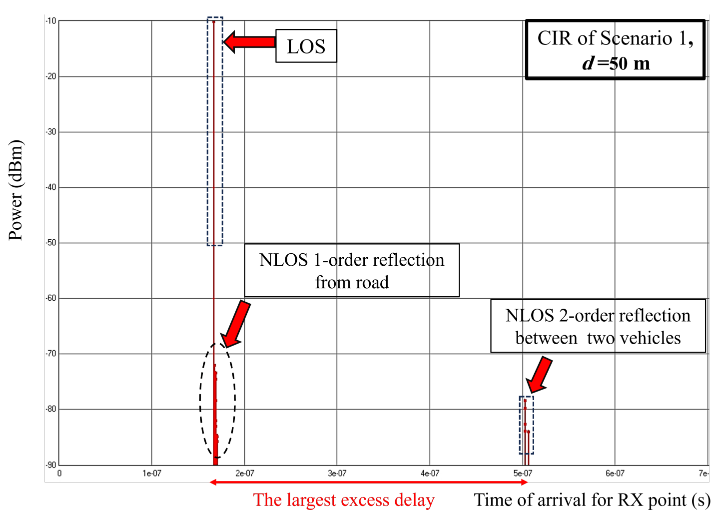

(c)

Figure 37: CIR of Scenario 1: (a) *d*= 10 m, (b) *d*= 30 m, (c) *d*=50 m

to more ToA, but also its power decreases. It is also observed that the NLOS 2-order reflections between the road and vehicle (See Fig. 35c) happen at a short TX-RX distance comparing Fig. 37a to 37c. Although they have less ToA, they are delivered to the receiver with lower powers compared to the reflections between two vehicles. The common reflections between the two vehicles (See Fig. 35b) as NLOS 2-order reflections at all TX-RX distances are the main factors behind increasing the excess delay. As a result of comparing Fig. 36 and Fig. 37, the LOS components are the dominant part of the total received power at every distance.

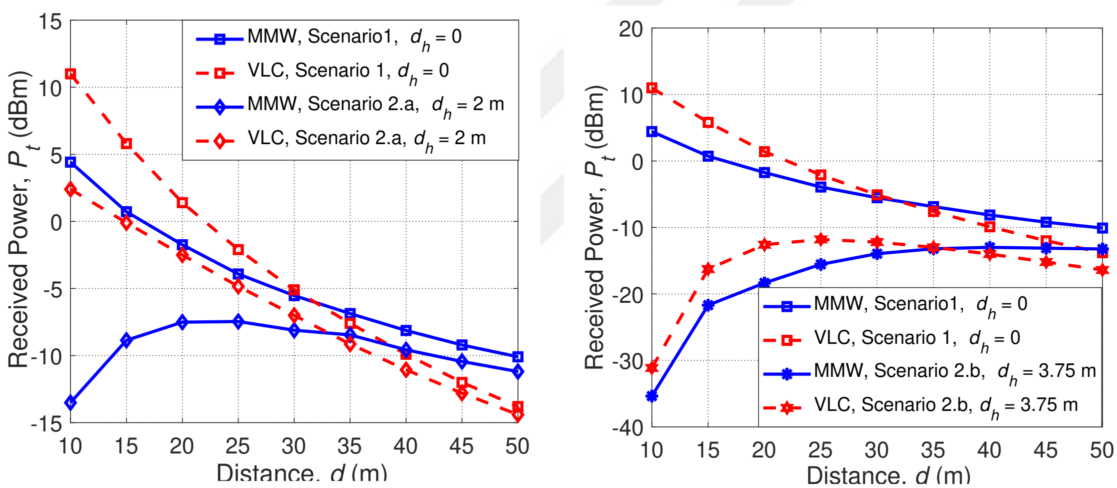

(a) (b)

Figure 38: Effect of the different lateral shifts in Scenario 2: (a) d_h= 2 m, (b) d_h= 3.75 m, $P_t = 40$ W is assumed.

In Fig. 38, we investigate the effect of lateral shift based on Scenario 2. It is observed that the received power first increases then decreases for the cases of lateral shifts (i.e., d_h = 2 m and 3.75m) unlike the case of perfect alignment (i.e., d_h = 0 m). The reason for this behavior is that the arrival angle on the receiver side is larger for short distances in the presence of lateral shifts. This effectively reduces the received power levels. When the transmission distance increases, the received power converges to that of the perfect alignment case, resulting in somewhat parabolic behavior. Comparing Fig. 38a and 37b further shows that the initial reduction of the received power level in the VLC system is less than that of the MMW system. This is mainly due to the geometry of the two headlight transmitters and the two receivers used in the VLC case. Having two receivers on the left and right side of vehicles results in better tackling for lateral shifts at short distances.

Fig. 39a and 38c show the CIR of scenario 2 for different lateral shifts at d=10 m. Let's consider the CIRs plotted in Fig. 37 and 39 together to analyze the effect of lateral shift on the behavior of the MMW channel. At first sight, the power of the LOS component as a dominant part in composing the received power decreases leading to less received power. The more lateral shift, the more power reduction has. This downtrend is the same for NLOS N-order reflections of roads and vehicles. The most interesting point caused by lateral shift is that the NLOS 2-order reflections have less ToA at d_h=2 m in comparison to d_h=3.75 m. Although there are some NLOS 1-order reflections from the road toward RX at d_h=2 m, just one reflection from the road could be delivered to RX as NLOS 1-order reflection at d_h=3.75 m. The main factor behind this fact is the different FoV by both TX and RX (See Fig. 39b and 39d). One also should not overlook the fact that the largest excess delays in both scenarios 1 and 2 are the same even by increasing the lateral shift.

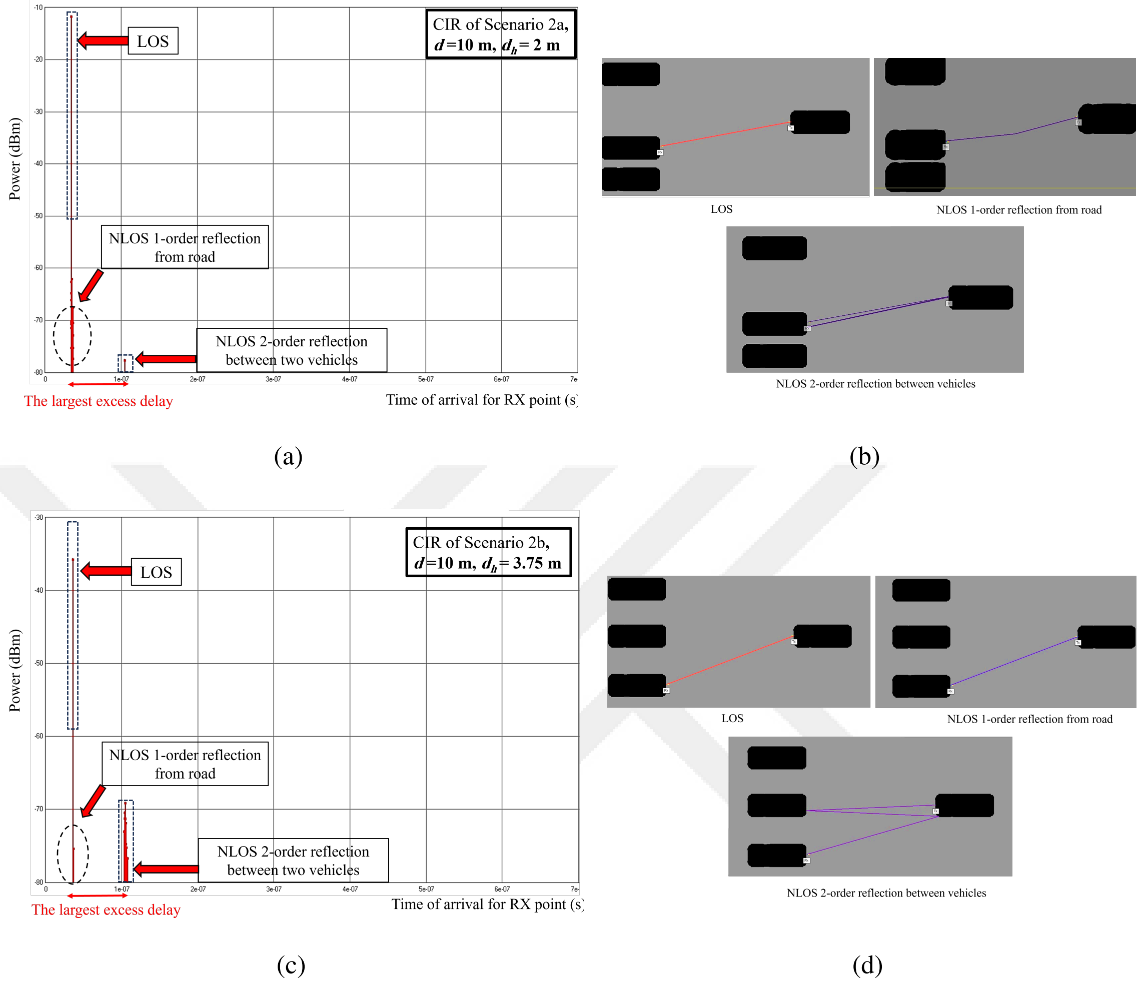

Figure 39: CIR of Scenario 2 for d=10 m: (a) d_h= 2 m, (b) LOS and N-order reflections for d_h=2 m, (c) d_h= 3.75 m, (d) LOS and N-order reflections for d_h=3.75 m,

Table 16: Calculating PVO related to Scenario 3 (Fig. 29 and 41)

Corresponding Scenario	***VOB***	***BOI***	***PVO***
Scenario 3a (Fig.29a and 41)	1	5	$PVO = \frac{1}{5} \times 100 = 20\%$
Scenario 3b (Fig.29b and 41)	3	5	$PVO = \frac{3}{5} \times 100 = 60\%$
Scenario 3c (Fig.29c and 41)	4	5	$PVO = \frac{4}{5} \times 100 = 80\%$

In Fig. 40, we investigate the effect of neighbor vehicles based on Scenario 3 described in Fig. 29. Let L_b denote the length of each block (see Fig. 41) and W_b denote the width of each block. In our case, it should be equal to or smaller than 4.67 m (i.e., the length of

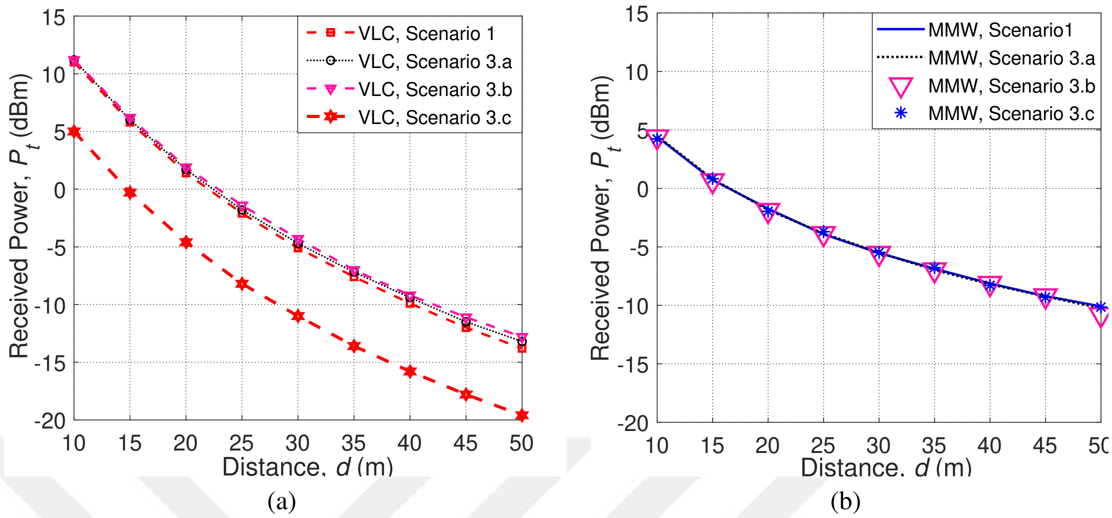

Figure 40: Effect of vehicle density in Scenario 3 (a) VLC, and (b) MMW, $P_t = 40$ W is assumed.

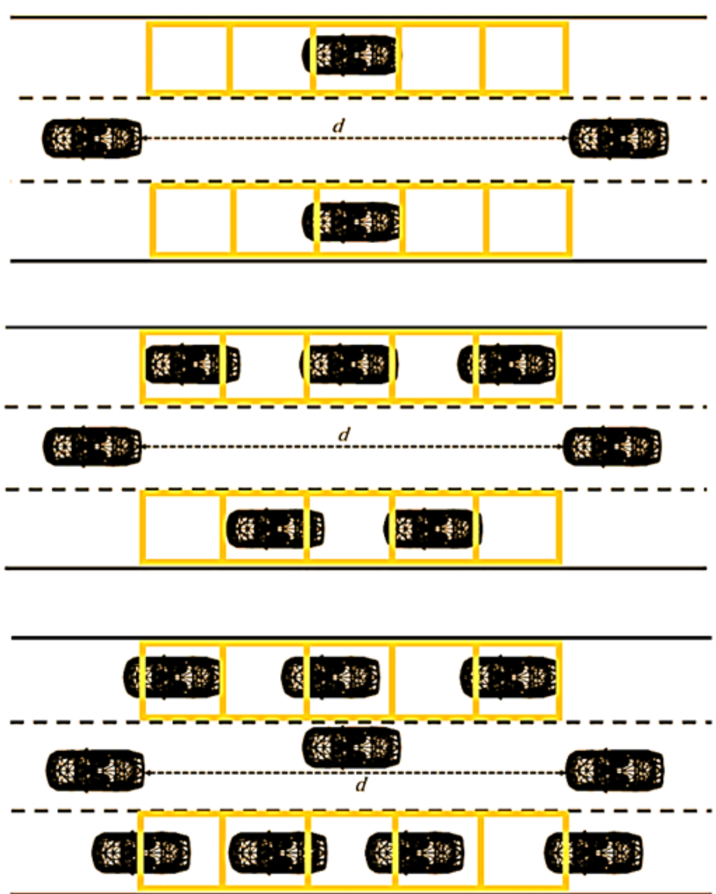

Figure 41: Classification of vehicle density by considering the block-based approach.

vehicles). For simplicity, assume W_b= 3.75m and L_b= 4.67 m. We consider the average distance between two vehicles as d=25 m. We calculate PVO for our corresponding sections of Scenario 3 i.e., Fig. 29a, Fig. 29b, and Fig. 29c. The results of PVO based on Table 16 by using (3.1) are 20%, 60%, and 80% for Scenario 3a, 3b, and 3c, respectively. Therefore, the calculations of PVOs for Scenario 3a, 3b, and 3c on Table 16, can be classified as low, mid, and high density based on Table 14. It is observed that the effect is negligible when the density of neighbor vehicles is small for both MMW and VLC systems. For high density (Scenario 3.c), the VLC system experiences some loss due to the partial blockage resulting from the vehicle in the middle (See Fig. 29c).

Fig. 42 demonstrates the CIRs related to the effect of vehicle density in the MMW channel. At first sight, comparing both Fig. 39 and 42, the LOS components have the same power. Therefore, there are no remarkable differences between the received powers of Scenarios 1 and 3 (See Fig. 40b). This fact is also proved for different densities of vehicles due to having the same power of LOS components. Although there are the less NLOS 1-order reflections from the road plotted with less power compared to LOS as the first components in CIR, just one NLOS 2-order reflection between the road and vehicle is displayed in Scenario 3a related to the low density of vehicles. Moreover, NLOS 2-order reflections between two vehicles lead to increasing the largest excess delay comparing the CIRs in Fig. 39 and 42. It is worth noting that there is no NLOS 2-order reflection between the road and the vehicle by increasing the density of vehicles.

In Fig. 43, we investigate the effect of LOS blockage and neighbor vehicles based on Scenario 4. In particular, we consider the full blockage described in Scenario 4.a. (Fig. 30a) and the partial blockage described in Scenario 4.b. (Fig. 30b). In the case of full blockage, Fig. 43a shows that there is no received power in the VLC system since the optical signal is completely blocked by the middle vehicle between TXs and RXs (See Fig. 30a). The MMW system is more robust and it is observed that the received power grows gradually by the distance until reaching its maximum. From Fig. 43b, it is observed that

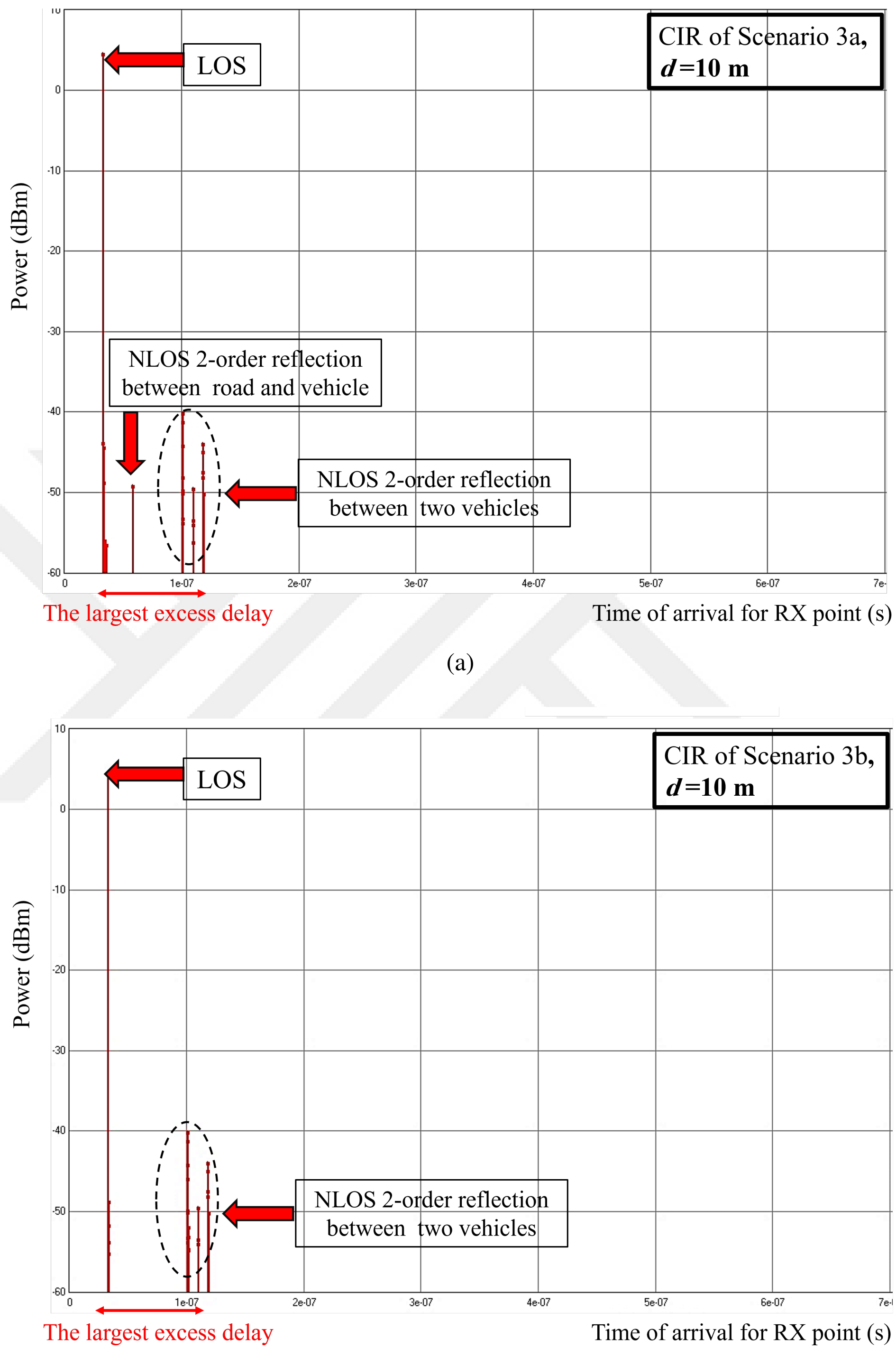

(a)

(b)

Figure 42: CIR of (a) Scenario 3a (Low density of vehicles), (b) Scenario 3b (Medium density of vehicles).

the received power has only a 1 dBm difference compared with Scenario 1 because the PDs are located at the side (RX1/RX2), at a blockage lateral distance (d_B) value of 0.5 m. When

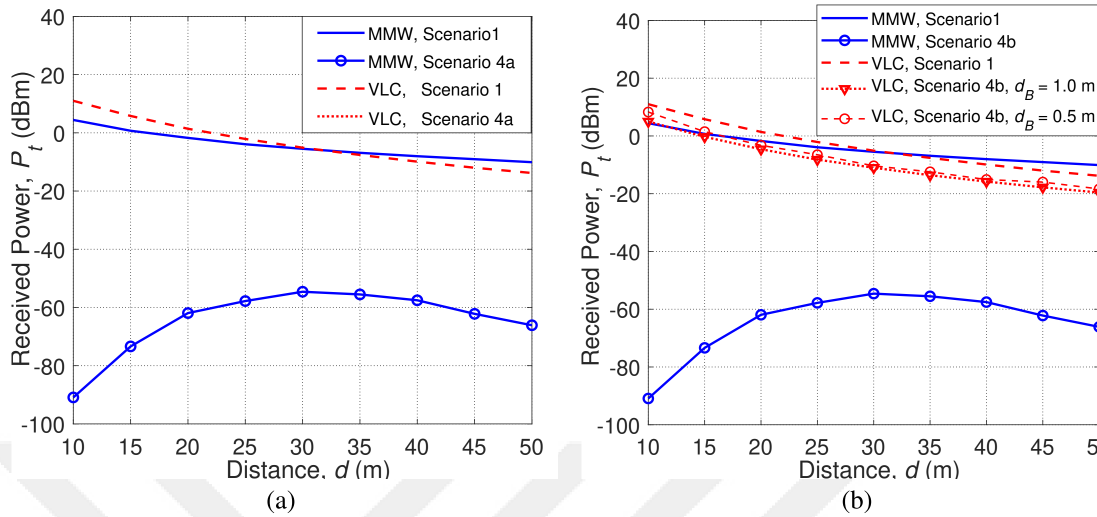

Figure 43: Effect of blockages on MMW and VLC in scenario 4: (a) Full blockage (b) Partial blockage, $P_t = 40$ W is assumed.

d_B between the blocking car and the connected cars increases in the VLC system, the effect of blockage is much reduced. In conclusion, both VLC and MMW have the same behavior for sufficiently small values of d_B (less than 0.5 m).

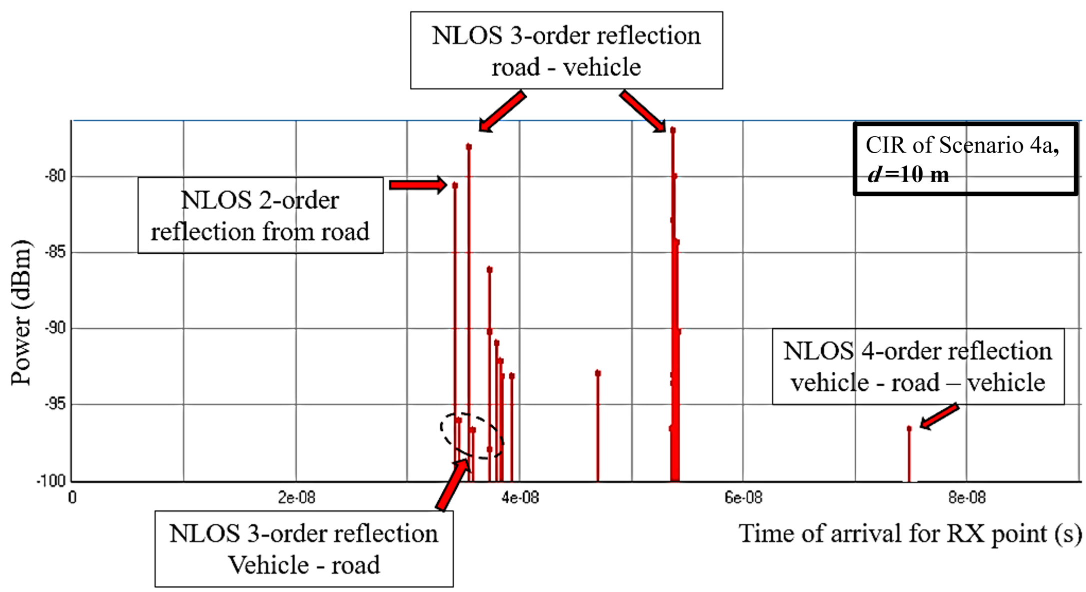

Figure 44: CIR of Scenario 4a for d= 10 m.

Fig. 44 and 45 present the CIR and MPCs of the blocked MMW channel related to Scenario 4a at d=10 m. At first sight in Fig. 44, the LOS component disappeared due to blocking it with the middle vehicle. Therefore, there is no first dominant component and the components with maximum power (approximately 80 dB less power than LOS in Scenario 1) are present at more ToA compared with the CIR of Fig. 37. There is also no NLOS 1-order reflection from the road delivered to the RX antenna. In other words, all rays at least experience two reflections, one of them is related to the road and others can be from the middle vehicle (See Fig. 45). Interestingly, the NLOS 2-order reflections from the road in the role of the first component (i.e., with less ToA in Fig. 44) and as good as the highest components are shown in Fig. 45a. However, Fig. 45b indicates that the last component in CIR come from NLOS 4-order reflections under the middle vehicle with road. More to the point, the NLOS 3-order reflections related to the components with maximum power started with reflection from the road and then re-mirror by vehicles as Fig. 45c and 44d. On the other hand, the components with minimum power are related to the NLOS 3-order rays with the first two reflections between vehicles and the third reflection from the road toward the RX antenna (See Fig. 45e and 44f). Overall, we can denote that the reflection ray from the road has less power than one from the vehicles due to the permittivity and conductivity of the road and vehicles.

So far, we assumed that the neighbor vehicles have inactive transmitters and considered only the effect of reflections and blockage from the neighbors on the received signal power was earlier defined as the optical power (intensity). In the following, we will investigate the effect of interference under the assumption that the neighbours have active transmitters. Let P_t denote the transmitted electrical power. Furthermore, let $\sigma^2 = N_0 B$ denote the noise variance where N_0 is the spectral power density and B is the bandwidth.The Signal-to-Interference-Noise Ratio (SINR) for MMW system is given by

$$\gamma = \frac{|H_{\mathrm{MMW}}|^2 P_t}{\sigma_n^2 + \sum_{j=1}^{N} |H_{\mathrm{MMW},j}|^2 P_t}, \tag{3.2}$$

where $|H_{\mathrm{MMW}}|$ is the magnitude of channel frequency response for the main MMW link and $|H_{\mathrm{MMW},j}|$ is the magnitude of channel frequency response associated with the j^{th} neighbour.

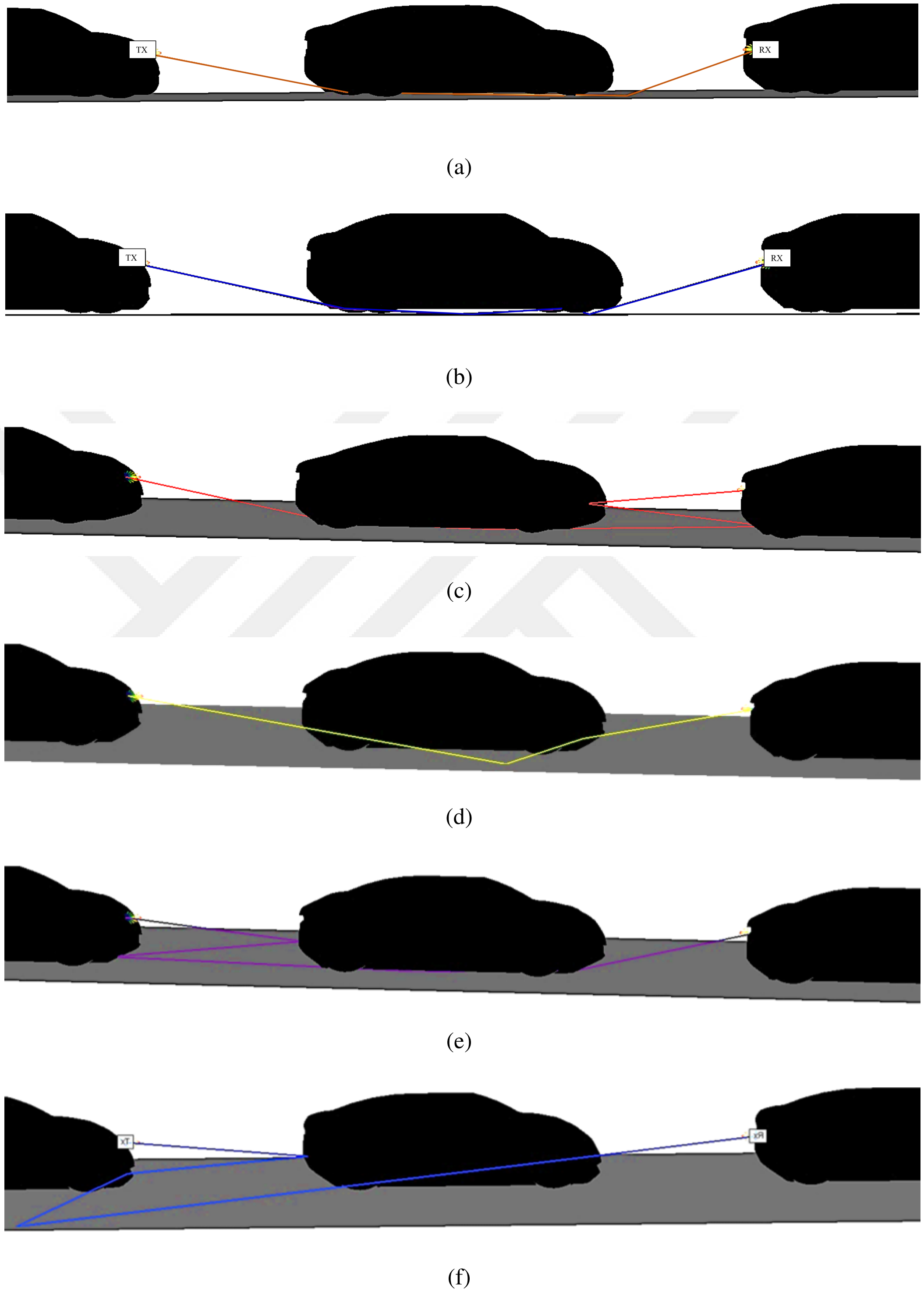

Figure 45: Propagation of MPCs for scenario 4a at d= 10 m related to (a) First component, (b) Last component, (c) First component with Max power, (d) Second component with Max power, (e) First components with Min power, (f) Second component with Min power.

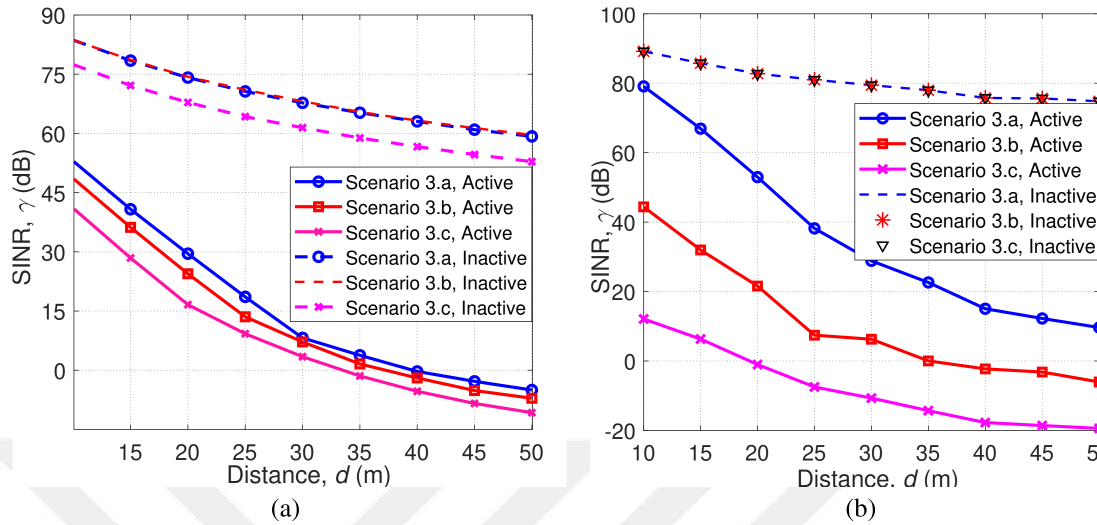

Figure 46: SINR for (a) VLC and (b) MMW systems. Scenario 3 is considered.

In Fig. 46, we present the SINR results and compare them with the case of inactive transmitters (i.e., no interference). We assume $N_0 = 10^{-21}\,\mathrm{A}^2/\mathrm{Hz}$, [90], [91] and B = 20 MHz [91]. In both systems, it is observed that the received SINR value reduces for all vehicle density scenarios as a result of the interference impact. However, it is observed that the VLC system suffers less from interference. That is because some of the interferers are completely blocked due to the high density of vehicles. For example, consider Scenario 3.c (high density) and a distance of d = 30 m. The received SINR reduces for VLC and MMW systems by 58 dB and 90 dB, respectively, in comparison to the case of inactive transmitters. In the MMW system with active transmitters, any additional vehicle strongly impacts the SINR performance, which makes a big difference in the SINR values associated with the three scenarios under consideration. In the VLC system, however, the interferences from the additional vehicles are more likely to be partially or fully blocked. Therefore, less difference in the SINR values is observed for the VLC system.

Besides the pavement material, the weather conditions influence the strength of the reflections as an atmospheric loss. Although the LOS link is impaired by bad weather conditions, in certain cases the reflectivity of the road can be improved as the NLOS links [92]. That's why exploiting the ray tracers as CAD tools increases the accuracy of weather

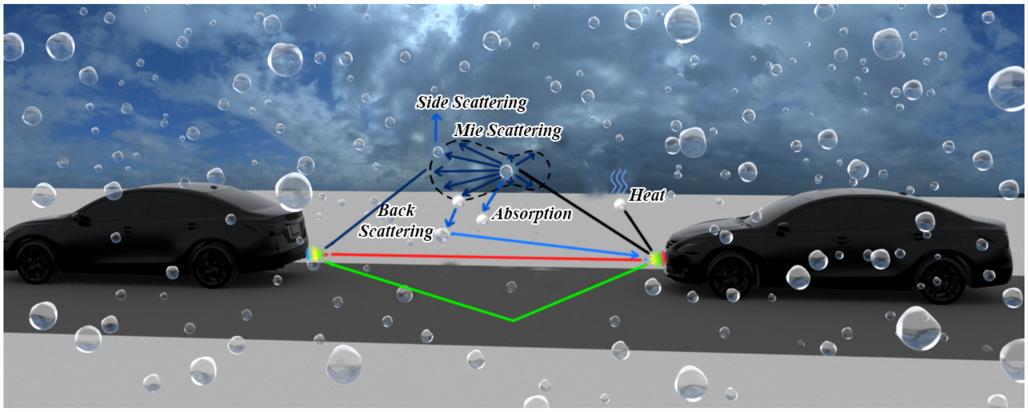

Figure 47: Effect of weather conditions on MMW V2V scenario.

conditions. Different processes occur including absorption, heat, multipath scatter, and backscatter by traveling through the atmosphere (See Fig. 47). Typically, there are two different types of scattering including Rayleigh and Mie scattering. Once the order of radius of the scattering particle is equal to 0.1 µm or greater, the scattering will begin to become an issue considering MMW. This corresponds to Mie scattering for rain, and drizzle while dust, smoke, and cloud droplets act as Rayleigh scatterers. As this paper investigates wavelengths on the order of a millimeter-wave focusing on rain and fog conditions, the Mie scattering is the main issue.

To model the effect of the weather conditions, the three parameters supplied by Wireless Insite are captured including the temperature, the humidity, and the pressure of weather. We take $T = 20°\text{C}$, $H = 60\%$, and $P = 101.3\,\text{kPa}$ to investigate the light rain. It is worth noting that other parameters including the size of rain rate and fog/snowdrops have not been included in Wireless Insite, therefore we can just study the light rain condition. We also take two closed-form attenuation models i.e. ITU and Millimeter wave Propagation Model (MPM) into account to compare our results with closed-form formulas. The equations were written in the Appendix B related to the rain attenuation coefficient. It is observed from Fig. 48 that the results from Wireless Insite match with the MPM analytical model and are close to the ITU model for light rain. It should be also observed that MMW system is much more affected by the rain conditions compared with the VLC system. One can notice

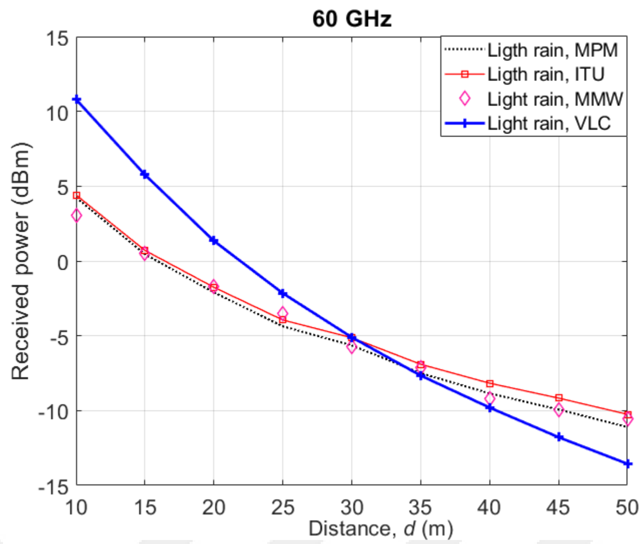

Figure 48: Effect of light rain condition on received power in terms of TX-RX distance.

also that even under the effect of rain conditions, VLC is well suited for short-distance communication while switching to MMW technology is required for higher distances.

CHAPTER IV

CONCLUSIONS AND FUTURE WORK

In this chapter, we review the entire dissertation objectives and results. We emphasize on the contributions that this research made. In the end, we give some prospective points for future work.

4.1 Conclusions

In this dissertation, we proposed a realistic MMW channel modeling approach based on a 3D wireless communication and propagation prediction software called Wireless Insite designed by Remcom company. Taking advantage of the advanced ray tracing features of this software, we were able to obtain realistic CIRs that take into account practical issues such as wavelength dependency of reflection coefficients, different types of reflections (diffuse, specular, and mixed cases of diffuse and specular), different types of antennas. We were also able to design different study areas including indoor and outdoor scenarios to obtain CIRs and other parameters related to channel characterization.

In Chapter II, We have developed a mobile RF channel based on non-sequential ray tracing. For realistic modeling, wavelength dependency was explicitly taken into account while different locations of antennas, different types of antennas, and different frequencies were considered. An empty indoor environment and CAD human models were used in our simulations. Under these realistic assumptions, we have obtained CIRs over the user movement trajectories and presented expressions for path loss and received power. Our results demonstrated that the received power varies significantly based on the user positions.

In detail, we investigated the effect of varying distances between the transmitter and receiver on indoor channel parameters. We presented a comprehensive one-to-one comparison between indoor VLC and RF channels based on advanced ray tracing simulators. We analyzed the CIRs obtained by ray tracing and compared the path loss at different indoor scenarios and frequency bands including 2.4 GHz, 6 GHz, 28 GHz, 60 GHz, 100 GHz, and VLC band. The different antenna types (i.e., omnidirectional, directional, rectangular patch, and indoor luminaire), receiver locations, and user trajectories (i.e., diagonal, vertical, and horizontal paths) have been investigated. It has been observed that the higher the RF bands, the path loss of the channel is higher, while the VLC channels exhibit a lower path loss level than MMW bands and a higher level than 2 GHz bands. Our results further revealed that the propagation channel characteristics are highly dependent on the antenna type same as the geometry of the user and the RX. For example, using the omnidirectional and rectangular patch antennas comes with lower path loss compared to the horn antennas, and such a gap significantly increases when the RX becomes closer to the TX antenna, where the direct LOS link becomes stronger. We then obtained closed-form expressions for the CDFs of indoor channels for all scenarios and receivers under consideration. While our current study is limited to two-dimensional scenarios, three-dimensional scenarios such as vertical movement in an elevator and vertical movement of the user in the case of a spiral staircase are interesting to explore in the future.

We further investigated CIRs for each configuration and presented a channel characterization study where channel parameters like path loss and received power are obtained. From the derived channel impulse responses, it is observed that the common property of the CIRs was composed of dominant multiple LOS links and some N-order NLOS delay taps due to reflection rays between walls, floor, and the human body.

In Chapter III, we presented a realistic vehicular MMW channel modeling approach for the practical ITS usage scenarios by taking advantage of advanced ray tracing. we presented a one-to-one comparison between vehicular VLC and MMW channels. For this purpose, we conducted extensive simulations in Wireless Insite ray tracing software tools and compared the received signal strengths for both systems under the same settings. In particular, we investigated communication scenarios between two vehicles in the same lane as well as in different lanes with a lateral shift. In comparison to the MMW system, the received signal in the VLC system is shown to exhibit a faster-decaying behavior. This indicates that VLC is better suited for relatively short-distance communication while MMW might be better for larger distances. We also studied the impact of the density of neighbor vehicles and blockage. Our results revealed that the MMW and VLC systems exhibit some similarities in some cases, in particular, due to their relatively narrow radiation/illumination patterns. However, in the case of full blockage, the MMW system was found to be superior to VLC system. In the case of partial blockage, VLC stood out as the better choice.

Building on non-sequential ray tracing, we have precisely taken into account the road reflection model. For each configuration, we obtained CIRs and presented a channel characterization study. From the derived channel impulse responses, it is observed that the common property of the CIRs was composed of dominant multiple LOS links and a less number of NLOS delay taps due to rflection between the vehicles and the road.

4.2 Future Work

X3D is a 3D propagation model with no restrictions on geometry shape or transmitter/receiver height. This accurate model includes reflections, transmissions, and diffractions along with atmospheric absorption and diffuse scattering. Supports frequencies up to 100 GHz [48]. In addition to the built-in waveforms, Wireless InSite allows User-Defined waveforms. They can be defined in either the time domain or frequency domain. For this purpose, Remcom specified the set-up file in a certain format that can be imported into the software. Therefore, realistic scenarios including both indoor and outdoor study areas can be extended to the THz band in future works.

Recently, Wireless InSite has facilitated the simulation of radio frequency (RF) interactions with engineered electromagnetic surfaces (EES), enabling the modeling of passive metasurfaces designed to optimize wireless communication coverage by influencing the propagation of signals through a given environment.

The capability to manipulate the electromagnetic (EM) propagation environment is a key focus in 6G research. Applications such as reconfigurable intelligent surfaces (RIS) depend on either metasurface or reflect arrays another technology option to enhance wireless channels. Engineered electromagnetic surfaces (EES) belong to the category of passive metasurfaces that enhance wireless coverage at microwave and millimeter-wave frequencies. This enhancement is achieved through printed conductive patterns on substrates like plastic or glass. When strategically positioned on surfaces such as walls, windows, or other structures, the scattering properties of these printed patterns redirect RF wave propagation, thereby improving wireless connectivity. The EES capability in Wireless InSite allows for the analysis of coverage enhancements, whether from a static EES or a specific configuration of a metasurface-based RIS.

Wireless InSite's EES capability is founded on the Ray Optical EES Scattering model, which was developed by the Communications Research Centre Canada (CRC), a part of Innovation, Science, and Economic Development Canada. The implementation of this model in Wireless InSite's ray tracing and EM path processing calculations enables the prediction of reflections, transmissions, and diffractions interacting with EES positioned within diverse environments, including office buildings and urban areas.

In the future, we aim to exploit the last capabilities of Wireless Insite to model the characteristics of RIS-added THz communication for different study environments. Some scenarios can be defined to investigate the CIR including the different locations of the RIS plane (i.e., enabling RIS close to TX or RX), various deflection angles from RIS toward the RX, and different sizes of RIS. Moreover, we can study both near-field and far-field scenarios considering the operating frequency. These parameters can be considered for RIS-aided scenarios in Indoor, vehicular, and UAV communications.

APPENDIX A

HORN ANTENNA

In this appendix, we present how we calculate the main parameters of the horn antenna used in our simulations. We consider a standard pyramid horn antenna with a peak gain of 23 dBi following [93] and the same aperture area as the VLC receiver for a fair comparison. The design of the horn antenna can be reduced to the solution of a single fourth-order equation given by [70]

$$A_{ap}^4 - a_f A_{ap}^3 + \frac{3b_f G\lambda^2}{8\pi\varepsilon_{ap}} A_{ap} - \frac{3G^2\lambda^4}{32\pi^2\varepsilon_{ap}^2} = 0, \tag{A1}$$

where G is the gain of the antenna, ε_{ap} is the aperture efficiency, and λ is the wavelength. A_{ap}, and B_{ap} are the dimensions of horn aperture, the dimensions of feed (wave guide) denoted by a_f, b_f (See Fig. 33a). R_1, R_2, α_E, and α_H are the intermediate parameters related to designing (E-H) planes of horn antennas [70]. The feed-aperture length of the horn antenna from two different views including the up view (R_H) and the right view (R_E) should have the same quantities in designing the antenna. For a horn antenna to be realizable and to have an effective area equal to 1 cm^2 [70], we need to have R_H = R_E and $A_{ap}B_{ap}$ = 1 cm^2. Following the steps in [70], the above parameters can be calculated as

$$A_{ap}^{(o)} = 0.45\lambda\sqrt{G} \tag{A2}$$

$$B_{ap} = \frac{1}{4\pi}\frac{G\lambda^2}{0.5A_{ap}}. \tag{A3}$$

$$R_1 = \frac{A_{ap}^2}{3\lambda}. \tag{A4}$$

$$R_2 = \frac{B_{ap}^2}{2\lambda}. \tag{A5}$$

$$R_E = R_2(1 - \frac{a_f}{A_{ap}}). \tag{A6}$$

$$R_H = R_1(1 - \frac{b_f}{B_{ap}}). \tag{A7}$$

In our case, we use the waveguide standard known WR-12 and WR-15 for a_f and b_f values (i.e., a_f = 0.12 cm, b_f = 0.06 cm and a_f = 0.36 cm, b_f = 0.18 cm) operating for MMW with normal gains of 20 dBi and 25 dBi, respectively [71, 94]. Based on these, we calculated A_{ap} = 1.032 cm, B_{ap} = 0.97 cm, and R_H = 0.58 cm.

APPENDIX B

RAIN CONDITIONS (MPM)

The Atmospheric Loss (AL) is added as much as the propagation loss in MMW noted by AL which is included by AL_{rain} related to rain attenuation calculated by the following:

$$AL = AL_{rain}[\mathrm{dB/m}]\, d[\mathrm{m}] \tag{B.1}$$

where d is the distance between the transmitter and receiver and AL_{rain} is

$$AL_{Rain} = 0.1820 f N''(f), \tag{B.2}$$

where $N''(f)$ is refractivity spectra related to MPM. Rain refractivity is approximated as follows:

$$N''_R(f) = a_r R^{b_r}, \tag{B.3}$$

$$a_r = X_1 f^{X_2}, \tag{B.4}$$

$$b_r = X_3 f^{X_4}, \tag{B.5}$$

where R is rain rate and frequency-dependent coefficient a and exponent b were calculated using drop size spectra of Laws and Parsons at the temperature of T=0°C. A regression fit to individual $(a_r,\, b_r)$ pairs over the frequency range from 54 to 180 GHz resulted as $X_1 = 0.225$, $X_2 = -0.301$, $X_3 = 2.63$, $X_4 = -0.272$ [92].

REFERENCES

[1] E. Hajlaoui, A. Zaier, A. Khlifi, J. Ghodhbane, M. B. Hamed, and L. Sbita, "4G and 5G technologies: A comparative study," in *Int. Conf. Advanced Technol. Signal and Image Processing (ATSIP)*, pp. 1–6, 2020.

[2] "Technical Feasibility of IMT in Bands Above 6 GHz, document ITU-R M.2376-0, ITU-R, International Telecommunication Union, 2015." `https://www.itu.int/dms_pub/itu-r/opb/rep/R-REP-M.2376-2015-PDF-E.pdf`. [Accessed: January 10, 2024].

[3] S. Kaddouri, M. El Hajj, G. Zaharia, and G. El Zein, "Indoor path loss measurements and modeling in an open-space office at 2.4 GHz and 5.8 GHz in the presence of people," *IEEE 29th Annu. Int. Symp. Pers. Indoor and Mobile Radio Commun.(PIMRC)*, pp. 1–7, Sep. 2018.

[4] B. M. Donlan, D. R. McKinstry, and R. M. Buehrer, "The UWB indoor channel: large and small scale modeling," *IEEE Trans. Wireless Commun.*, vol. 5, no. 10, pp. 2863–2873, Oct. 2006.

[5] I. D. S. Batalha *et al.*, "Indoor corridor and office propagation measurements and channel models at 8, 9, 10 and 11 GHz," *IEEE Access*, vol. 7, pp. 55005–55021, May. 2019.

[6] N. Zhang *et al.*, "Dynamic channel modeling for an indoor scenario at 23.5 GHz," *IEEE Access*, vol. 3, pp. 2950–2958, Dec. 2015.

[7] A. Sreedevi, T. R. Rao, and M. Susila, "Measurements at 2.4, 3.4, 5.2, 28 and 60 GHz for device-to-device wireless communications," *Wireless Pers. Commun.*, vol. 108, no. 3, pp. 1733–1743, May. 2019.

[8] Y. Xing *et al.*, "Millimeter wave and sub-THz indoor radio propagation channel measurements, models, and comparisons in an office environment," *IEEE Commun. Lett.*, vol. 25, no. 10, pp. 3151–3155, Jun. 2021.

[9] X. Wu *et al.*, "Two-stage access point selection for hybrid VLC and RF networks," in *2016 IEEE 27th Annual International Symposium on Personal, Indoor, and Mobile Radio Communications (PIMRC)*, pp. 1–6, 2016.

[10] L. Feng *et al.*, "MmWave and VLC-based indoor channel models in 5G wireless networks," *IEEE Wirel. Commun.*, vol. 25, no. 5, pp. 70–77, 2018.

[11] M. Sobetwa and O. Sokoya, "Measurement analysis of indoor parameters for an indoor wireless propagation," in *Int. Conf. Wireless Technol. Embedded and Intell. Syst. (WITS)*, pp. 1–6, 2019.

[12] J. Choi, V. Va, N. Gonzalez-Prelcic, R. Daniels, C. R. Bhat, and R. W. Heath, "Millimeter-wave vehicular communication to support massive automotive sensing," *IEEE Commun. Mag.*, vol. 54, no. 12, pp. 160–167, 2016.

[13] V. Va, T. Shimizu, G. Bansal, R. W. Heath Jr, *et al.*, "Millimeter wave vehicular communications: A survey," *Foundations and Trends® in Networking*, vol. 10, no. 1, pp. 1–113, 2016.

[14] M. Giordani, Shimizu, *et al.*, "Path loss models for V2V mmwave communication: Performance evaluation and open challenges," in *Proc. 2nd IEEE Connected and Autom. Veh. Symp. (CAVS)*, pp. 1–5, IEEE, 2019.

[15] G. Sanchez *et al.*, "Millimeter wave radio channel characterization for 5G vehicle to vehicle communications," *Measurement, Elsevier*, vol. 95, pp. 223–229, 2017.

[16] E. Kampert, Jennings, *et al.*, "Investigating the V2V millimeter-wave channel near a vehicular headlight in an engine bay," *IEEE Commun. Lett.*, vol. 22, no. 7, pp. 1506–1509, 2018.

[17] E. Ben-Dor, Rappaport, *et al.*, "Millimeter-wave 60 GHz outdoor and vehicle AOA propagation measurements using a broadband channel sounder," in *Proc. IEEE Global Telecommun. Conf. (GLOBECOM)*, pp. 1–6, 2011.

[18] J.-J. Park *et al.*, "Millimeter wave vehicular blockage characteristics based on 28 GHz measurements," in *Proc. IEEE 86th Veh. Tech. Conf.(VTC-Fall)*, pp. 1–5, IEEE, 2017.

[19] M. Boban *et al.*, "Multi-band vehicle-to-vehicle channel characterization in the presence of vehicle blockage," *IEEE Access*, vol. 7, pp. 9724–9735, 2019.

[20] Y.-J. Chen, T. Hsu, and L.-C. Wang, "Improving handover performance in 5G mm-wave hetnets," in *GLOBECOM 2017-2017 IEEE Global Commun. Conf.*, pp. 1–6, IEEE, 2017.

[21] Y. Niu, Y. Li, D. Jin, L. Su, and A. V. Vasilakos, "A survey of millimeter wave communications (mmwave) for 5G: opportunities and challenges," *Wireless Netw.*, vol. 21, pp. 2657–2676, 2015.

[22] J. Stańczak, "Mobility enhancements to reduce service interruption time for LTE and 5G," in *IEEE Conf. Standards for Commun. and Netw. (CSCN)*, pp. 1–5, 2016.

[23] R. Schneider, D. Didascalou, and W. Wiesbeck, "Impact of road surfaces on millimeter-wave propagation," *IEEE Trans. Veh. Technol.*, vol. 49, no. 4, pp. 1314–1320, 2000.

[24] T. Wada, M. Maeda, M. Okada, K. Tsukamoto, and S. Komaki, "Theoretical analysis of propagation characteristics in millimeter-wave intervehicle communication system," *Electronics and Communications in Japan (Part II: Electronics)*, vol. 83, no. 11, pp. 33–43, 2000.

[25] A. Maltsev, A. Pudeyev, I. Karls, I. Bolotin, G. Morozov, R. Weiler, M. Peter, and W. Keusgen, "Quasi-deterministic approach to mmwave channel modeling in a non-stationary environment," in *2014 IEEE Globecom Workshops (GC Wkshps)*, pp. 966–971, IEEE, 2014.

[26] J. W. McKown and R. L. Hamilton, "Ray tracing as a design tool for radio networks," *IEEE Netw. Mag.*, vol. 5, no. 6, pp. 27–30, Nov. 1991.

[27] W. Honcharenko, H. Bertoni, J. Dailing, J. Qian, and H. Yee, "Mechanisms governing UHF propagation on single floors in modern office buildings," *IEEE Trans. Veh. Technol. (TVT)*, vol. 41, no. 4, pp. 496–504, Nov. 1992.

[28] P. F. Driessen and T. Gimersky, M.and Rhodes, *Ray Model of Indoor Propagation*. Wireless Pers. Commun., 1993.

[29] T. Holt, K. Pahlavan, and J. Lee, "A graphical indoor radio channel simulator using 2D ray tracing," in *Proc. IEEE Int. Symp. Personal, Indoor, and Mobile Radio Communications*, pp. 411–416, Oct. 1992.

[30] F. Ikegami, T. Takeuchi, and S. Yoshida, "Theoretical prediction of mean field strength for urban mobile radio," *IEEE Trans. Antennas Propag.*, vol. 39, pp. 299–302, Mar. 1991.

[31] T. S. Rappaport, S. Y. Seidel, and K. R. Schaubach, *Site-Specific Propagation Prediction for PCS System Design*. Wireless Pers. Commun., 1993.

[32] M. Lawton and J. McGeehan, "The application of GTD and ray launching techniques to channel modeling for cordless radio systems," in *Proc. 42nd IEEE Veh. Technol. Conf*, pp. 125–130, May. 1992.

[33] N. Amitay, "Modeling and computer simulation of wave propagation in lineal line-of-sight microcells," *IEEE Trans. Veh. Technol.*, vol. 41, no. 4, pp. 337–342, Nov. 1992.

[34] S. Priebe, M. Jacob, C. Jastrow, T. Kleine-Ostmann, T. Schrader, and T. Kürner, "A comparison of indoor channel measurements and ray tracing simulations at 300 GHz," in *35th Int. Conf. Infrared, Millimeter, and Terahertz Waves*, pp. 1–2, 2010.

[35] "Wireless Insite." `http://www.remcom.com/wireless-insite/`, 2019. [Accessed: January 10, 2024].

[36] R. Luebbers, "Finite conductivity uniform GTD versus knife edge diffraction in prediction of propagation path loss," *IEEE Trans. Antennas Propag.*, vol. 32, no. 1, pp. 70–76, Jan. 1984.

[37] W. Burnside and K. Burgener, "High frequency scattering by a thin lossless dielectric slab," *IEEE Trans. Antennas Propag.*, vol. 31, no. 1, pp. 104–110, Jan. 1983.

[38] "Effects of building materials and structures on radio wave propagation above about 100 MHz," *Recommendation ITU-R*, pp. 2040–1, Jul. 2015.

[39] "Electrical characteristics of the surface of the earth," *Recommendation ITU-R*, pp. 527–3, 1992.

[40] C. A. Balanis, *Advanced Engineering Electromagnetics*. New York: Wiley, 1989.

[41] M. C. Jeruchim, P. Balaban, and K. S. Shanmugan, *Simulation of Communication Systems*. New York: Plenum Press, 1992.

[42] R. Marks, C. Eklund, S. Ponnuswamy, K. L. Stanwood, and N. J. van Waes, "Wirelessman: Inside the IEEE 802.16 standard for wireless metropolitan area networks," *IEEE Standards Information Network/IEEE Press, first ed.*, May. 2006.

[43] R. G. Kouyoumjian and P. H. Pathak, "A uniform geometrical theory of diffraction for an edge in a perfectly conducting surface," *Proceedings of the IEEE*, vol. 62, no. 11, pp. 1448–1461, 1974.

[44] M. Hata, "Empirical formula for propagation loss in land mobile radio services," *IEEE Trans. Veh. Technol.*, vol. 29, no. 3, pp. 317–325, Aug. 1980.

[45] "Receive diversity, course notes, dept. of electrical and computer engineering, u. toronto." `http://www.comm.utoronto.ca/~rsadve/Notes/DiversityReceive.pdf`. [Accessed: January 10, 2024].

[46] J. R., *Radiowave Propagation and Smart Antennas for Wireless Communications.* Kluwer Academic Publishers, 2000.

[47] E. Telatar, "Capacity of multi-antenna gaussian channels," *European Trans. Telecomm. (ETT)*, vol. 10, no. 6, pp. 585–595, 1999.

[48] F. Aghaei, H. B. Eldeeb, L. Bariah, S. Muhaidat, and M. Uysal, "Comparative characterization of indoor VLC and MMW communications via ray tracing simulations," *IEEE Access*, vol. 11, pp. 90345–90357, Aug. 2023.

[49] F. Aghaei, H. B. Eldeeb, and M. Uysal, "A comparative evaluation of propagation characteristics of vehicular VLC and MMW channels," *IEEE Trans. Veh. Technol.*, pp. 1–10, Jul. 2023.

[50] T. E. Bogale and L. B. Le, "Massive MIMO and mmWave for 5G wireless hetnet: Potential benefits and challenges," *IEEE Veh. Technol. Mag.*, vol. 11, no. 1, pp. 64–75, 2016.

[51] M. Uysal, "Visible light communications: from theory to industrial standardization," in *IEEE Opt. Fiber Commun. Conf. and Exh. (OFC)*, pp. 1–3, Mar. 2019.

[52] A. Jovicic, J. Li, and T. Richardson, "Visible light communication: opportunities, challenges and the path to market," *IEEE Commun. Mag.*, vol. 51, no. 12, pp. 26–32, Dec. 2013.

[53] Y. Chen, W. Guan, J. Li, and H. Song, "Indoor real-time 3-D visible light positioning system using fingerprinting and extreme learning machine," *IEEE Access*, vol. 8, pp. 13875–13886, 2020.

[54] P. Du, S. Zhang, C. Chen, H. Yang, W.-D. Zhong, R. Zhang, A. Alphones, and Y. Yang, "Experimental demonstration of 3D visible light positioning using received signal strength with low-complexity trilateration assisted by deep learning technique," *IEEE Access*, vol. 7, pp. 93986–93997, 2019.

[55] F. Wang, F. Yang, J. Song, and Z. Han, "Access frameworks and application scenarios for hybrid VLC and RF systems: State of the art, challenges, and trends," *IEEE Commun. Mag.*, vol. 60, no. 3, pp. 55–61, 2022.

[56] S. M. Sheikholeslami *et al.*, "Communication-efficient federated learning for hybrid VLC/RF indoor systems," *IEEE Access*, vol. 10, pp. 126479–126493, 2022.

[57] Abuella, Hisham, *et al.*, "Hybrid RF/VLC systems: A comprehensive survey on network topologies, performance analyses, applications, and future directions," *IEEE Access*, vol. 9, pp. 160402–160436, 2021.

[58] Adnan-Qidan, Ahmad, Morales-Céspedes, Máximo, Armada, and A. García, "Load balancing in hybrid VLC and RF networks based on blind interference alignment," *IEEE Access*, vol. 8, pp. 72512–72527, 2020.

[59] M. G. Sanchez, *Millimeter-wave (mmwave) communications*. MDPI-Multidisciplinary Digital Publishing Institute, 2020.

[60] S. Althunibat, R. Mesleh, and K. Qaraqe, "Secure index-modulation based hybrid free-space optical and millimeter wave links," *IEEE Trans. Veh. Techno.*

[61] L. Feng *et al.*, "MmWave and VLC-based indoor channel models in 5G wireless networks," *IEEE Wireless Commun.*, vol. 25, no. 5, pp. 70–77, Aug. 2018.

[62] I. Stefan, H. Burchardt, and H. Haas, "Area spectral efficiency performance comparison between vlc and rf femtocell networks," in *IEEE Int. Conf. Commun. (ICC)*, pp. 3825–3829, Nov. 2013.

[63] T. K. Geok, F. Hossain, and A. T. W. Chiat, "A novel 3D ray launching technique for radio propagation prediction in indoor environments," *PloS one*, vol. 13, no. 8, p. e0201905, 2018.

[64] J. Zhang, J. Lin, P. Tang, W. Fan, Z. Yuan, X. Liu, H. Xu, Y. Lyu, L. Tian, and P. Zhang, "Deterministic ray tracing: A promising approach to THz channel modeling in 6G deployment scenarios," *IEEE Commun. Mag.*, 2023.

[65] T. Geok, F. Hossain, S. Rahim, O. Elijah, A. A. Eteng, C. T. Loh, L. Li, C. Tso, T. A. Rahman, and M. Hindia, "3D RT adaptive path sensing method: RSSI modelling validation at 4.5 GHz, 28 GHz, and 38 GHz," *Alexandria Eng. J.*, vol. 61, no. 12, pp. 11041–11061, 2022.

[66] H. B. Eldeeb *et al.*, "Channel modelling for light communications: Validation of ray tracing by measurements," in *IEEE 12th Int. Symp. Commun. Syst. Netw. Digit. Signal Process. (CSNDSP)*, pp. 1–6, Nov. 2020.

[67] A. Uyrus and B. Turan, "Recommendation ITU-R P.2040-1: Effects of building materials and structures on radio wave propagation above about 100 MHz," *Recomm. ITU-R P.2040*, vol. 1, Jul. 2015.

[68] M. Uysal, F. Miramirkhani, T. Baykas, and K. Qaraqe, "IEEE 802.11 bb reference channel models for indoor environments," tech. rep., Sep. 2018.

[69] H. Ling, R.-C. Chou, and S.-W. Lee, "Shooting and bouncing rays: Calculating the RCS of an arbitrarily shaped cavity," *IEEE Trans. Antennas Propag.*, vol. 37, no. 2, pp. 194–205, Feb. 1989.

[70] G. Abhignya, B. Yogita, C. Abhinay, and B. Balaji, "Design, fabrication, and testing of pyramidal horn antenna," *Int. J. Engin. Appl. Sci. (IJEAS)*, vol. 2, no. 24, pp. 2394–3661, Apr. 2015.

[71] "Wr-15 waveguide standard gain horn antenna operating from 50 GHz to 75 GHz with a nominal 25 dBi gain with UG-385 / U-Mod round cover flange." `https://www.pasternack.com/wr-15-waveguide-gain-horn-antenna-25dbi-ug-385-mod-round-flange-/pewan1012-p.aspx`. [Accessed: Dec. 30, 2022].

[72] A. Maltsev, A. Pudeyev, A. Lomayev, and I. Bolotin, "Channel modeling in the next generation mmWave Wi-Fi: IEEE 802.11ay standard," in *European Wireless 2016; 22th European Wireless Conference*, pp. 1–8, 2016.

[73] K. Jurczenia and J. Rak, "A survey of vehicular network systems for road traffic management," *IEEE Access*, vol. 10, pp. 42365–42385, 2022.

[74] J. B. Kenney, "Dedicated short-range communications (DSRC) standards in the united states," *Proc. IEEE*, vol. 99, no. 7, pp. 1162–1182, 2011.

[75] "Toyota its web exhibition 2021 - V2X." `https://www.toyota.co.jp/its/en/2021/v2xtechnology/`. [Accessed: January 10, 2024].

[76] G. Naik *et al.*, "IEEE 802.11bd 5G NR V2X: Evolution of radio access technologies for V2X communications," *IEEE Access*, vol. 7, pp. 70169–70184, 2019.

[77] "China autonomous and 5G industry integration development report 2022 application of 5G V2X will promote the realization of high-level autonomous driving research and markets.com." `https://www.businesswire.com/news/home/20220523005608/en/`. [Accessed: January 10, 2024].

[78] "Ford says all of its vehicles will 'Talk and Listen'by 2022 via 5G C-V2X." `https://www.dbusiness.com/daily-news/ford-says-all-of-its-vehicles-will-talk-and-listen-by-2022-via/5g-c-v2x/`. [Accessed: January 10, 2024].

[79] M. Noor-A-Rahim *et al.*, "6G for vehicle-to-everything (V2X) communications: Enabling technologies, challenges, and opportunities," *Proc. IEEE*, vol. 110, no. 6, pp. 712–734, 2022.

[80] G. Singh, Srivastava, *et al.*, "Heterogeneous visible light and radio communication for improving safety message dissemination at road intersection," *IEEE Trans. Intell. Transp. Syst.*, pp. 1–13, 2022.

[81] A. Tassi, M. Egan, R. J. Piechocki, and A. Nix, "Modeling and design of millimeter-wave networks for highway vehicular communication," *IEEE Trans. Veh. Technol.*, vol. 66, no. 12, pp. 10676–10691, 2017.

[82] B. Turan, S. C. Ergen, O. Narmanlioglu, M. Uysal, and F. Hu, "IEEE 802.15. 13-compliant visible light communications in vehicular networks," in *Vehicle-to-vehicle and vehicle-to-infrastructure communications*, pp. 125–140, 2018.

[83] M. Uysal, Z. Ghassemlooy, A. Bekkali, A. Kadri, and H. Menouar, "Visible light communication for vehicular networking: Performance study of a V2V system using a measured headlamp beam pattern model," *IEEE Vehicular Technology Magazine*, vol. 10, no. 4, pp. 45–53, 2015.

[84] L. Feng *et al.*, "MmWave and VLC-based indoor channel models in 5G wireless networks," *IEEE Wirel. Commun.*, vol. 25, no. 5, pp. 70–77, 2018.

[85] A. Uyrus *et al.*, "Visible light and mmWave propagation channel comparison for vehicular communications," in *Proc. 10th IEEE Veh. Netw. Conf. (VNC)*, pp. 1–7, IEEE, 2019.

[86] K. Garg *et al.*, "Real-time road traffic density estimation using block variance," in *2016 IEEE Winter Conf. Appl. of Comput. Vision (WACV)*, pp. 1–9, 2016.

[87] H. B. Eldeeb *et al.*, "A path loss model for vehicle-to-vehicle visible light communications," in *Proc. 15th Int. Conf. on Telecommun. (ConTEL)*, pp. 1–5, IEEE, 2019.

[88] V. Degli-Esposti, "A diffuse scattering model for urban propagation prediction," *IEEE Trans. Antennas Propag.*, vol. 49, no. 7, pp. 1111–1113, Jul. 2001.

[89] J. Senic, C. Gentile, P. B. Papazian, K. A. Remley, and J.-K. Choi, "Analysis of E-band path loss and propagation mechanisms in the indoor environment," *IEEE Trans. Antennas Propag.*, vol. 65, no. 12, pp. 6562–6573, Dec. 2017.

[90] M. Vaezi *et al.*, *Multiple access techniques for 5G wireless networks and beyond*, vol. 159. Springer, 2019.

[91] X. Wu *et al.*, "Two-stage access point selection for hybrid vlc and rf networks," in *2016 IEEE 27th Annual International Symposium on Personal, Indoor, and Mobile Radio Communications (PIMRC)*, pp. 1–6, 2016.

[92] H. J. Liebe, *An atmospheric millimeter wave propagation model*. US Department of Commerce, National Telecommunications and Information . . . , 1984.

[93] A. Yamamoto *et al.*, "Path-loss prediction models for intervehicle communication at 60 GHz," *IEEE Trans. veh. Technol*, vol. 57, no. 1, pp. 65–78, 2008.

[94] "Wr-12 waveguide standard gain horn antenna operating from 60 GHz to 90 GHz with a nominal 20 dBi gain with UG-387 / U-Mod round cover flange." `https://www.pasternack.com/wr-12-waveguide-gain-horn-antenna-10dbi-ug-387-mod-round-flange-/pewan1013-p.aspx`. [Accessed: January 10, 2024].

VITA

Fahimeh Aghaei is an Iranian researcher. She was born in 1985 in IRAN. She received her B.Sc. and M.Sc. degrees (Hons.) in electrical engineering from the Isfahan University of IRAN in 2010 and 2016, respectively. She joined the Communication Theory and Technologies (CT&T) Research Group as a Research Assistant in 2020 working toward his doctorate under the supervision of Prof. Murat Uysal at Özyeğin University, Istanbul, Turkey. Her current research interests include millimeter communications, Channel modeling, vehicular communication, and Reconfigurable Intelligent Surface (RIS).